Pontifícia Universidade Católica
do Rio de Janeiro

Luis Ernesto Ynoquio Herrera

MOBILE ROBOT SIMULTANEOUS LOCALIZATION AND MAPPING USING DP-SLAM WITH A SINGLE LASER RANGE FINDER

M.Sc. Thesis

Thesis presented to obtain the M.Sc. title at the Mechanical Engineering Department at PUC-Rio.

Advisor: Marco Antonio Meggiolaro

Rio de Janeiro

Abril 2011

Luis Ernesto Ynoquio Herrera

MAPEAMENTO E LOCALIZAÇÃO SIMULTÂNEA DE ROBÔS MÓVEIS USANDO DP-SLAM E UM ÚNICO MEDIDOR LASER POR VARREDURA

Dissertação apresentada como requisito parcial para obtenção do grau de Mestre pelo Programa de Pós-Graduação em Engenharia Mecânica do Departamento de Engenharia Mecânica do Centro Técnico Científico da PUC-Rio. Aprovada pela Comissão Examinadora abaixo assinada.

Rio de Janeiro, 7 de abril de 2011

Abstract

Luis Ernesto, Ynoquio Herrera; Meggiolaro, Marco Antonio (Orientador). **Mobile Robot Simultaneous Localization and Mapping Using DP-SLAM with a Single Laser Range Finder** Rio de Janeiro 2011, 168p. M.Sc. Dissertation – Mechanical Engineering Department, Pontifícia Universidade Católica do Rio de Janeiro.

Simultaneous Localization and Mapping (SLAM) is one of the most widely researched areas of Robotics. It addresses the mobile robot problem of generating a map without prior knowledge of the environment, while keeping track of its position. Although technology offers increasingly accurate position sensors, even small measurement errors can accumulate and compromise the localization accuracy. This becomes evident when programming a robot to return to its original position after traveling a long distance, based only on its sensor readings. Thus, to improve SLAM´s performance it is necessary to represent its formulation using probability theory. The Extended Kalman Filter SLAM (EKF-SLAM) is a basic solution and, despite its shortcomings, it is by far the most popular technique. Fast SLAM, on the other hand, solves some limitations of the EKF-SLAM using an instance of the Rao-Blackwellized particle filter. Another successful solution is to use the DP-SLAM approach, which uses a grid representation and a hierarchical algorithm to build accurate 2D maps. All SLAM solutions require two types of sensor information: odometry and range measurement. Laser Range Finders (LRF) are popular range measurement sensors and, because of their accuracy, are well suited for odometry error correction. Furthermore, the odometer may even be eliminated from the system if multiple consecutive LRF scans are matched. This works presents a detailed implementation of these three SLAM solutions, focused on structured indoor environments. The implementation is able to map 2D environments, as well as 3D environments with planar terrain, such as in a typical indoor application. The 2D application is able to automatically generate a stochastic grid map. On the other hand, the 3D problem uses a point cloud representation of the map, instead of a 3D grid, to reduce the SLAM computational effort. The considered mobile robot only uses a single LRF, without any odometry information. A Genetic Algorithm is presented to optimize the matching of LRF scans taken at different instants. Such matching is able not only to map the environment but also localize the robot, without the need for odometers or other sensors. A simulation program is implemented in Matlab® to generate virtual LRF readings of a mobile robot in a 3D environment. Both simulated readings and experimental data from the literature are independently used to validate the proposed methodology, automatically generating 3D maps using just a single LRF.

Key Words

Mobile Robots, Bayesian Filter, Scan Matching, Simultaneous Localization and Mapping, Laser Range Finder.

Resumo

Luis Ernesto, Ynoquio Herrera; Meggiolaro, Marco Antonio (Orientador). **Mapeamento e Localização Simultânea de Robôs Móveis usando DP-SLAM e um Único Medidor Laser por Varredura** Rio de Janeiro 2011, 168p. Dissertação de Mestrado – Departamento de Engenharia Mecânica, Pontifícia Universidade Católica do Rio de Janeiro.

SLAM (Mapeamento e Localização Simultânea) é uma das áreas mais pesquisadas na Robótica móvel. Trata-se do problema, num robô móvel, de construir um mapa sem conhecimento prévio do ambiente e ao mesmo tempo manter a sua localização nele. Embora a tecnologia ofereça sensores cada vez mais precisos, pequenos erros na medição são acumulados comprometendo a precisão na localização, sendo estes evidentes quando o robô retorna a uma posição inicial depois de percorrer um longo caminho. Assim, para melhoria do desempenho do SLAM é necessário representar a sua formulação usando teoria das probabilidades. O SLAM com Filtro Extendido de Kalman (EKF-SLAM) é uma solução básica, e apesar de suas limitações é a técnica mais popular. O Fast SLAM, por outro lado, resolve algumas limitações do EKF-SLAM usando uma instância do filtro de partículas conhecida como *Rao-Blackwellized*. Outra solução bem sucedida é o DP-SLAM, o qual usa uma representação do mapa em forma de grade de ocupação, com um algoritmo hierárquico que constrói mapas 2D bastante precisos. Todos estes algoritmos usam informação de dois tipos de sensores: odômetros e sensores de distância. O *Laser Range Finder* (LRF) é um medidor laser de distância por varredura, e pela sua precisão é bastante usado na correção do erro em odômetros. Este trabalho apresenta uma detalhada implementação destas três soluções para o SLAM, focalizado em ambientes fechados e estruturados. Apresenta-se a construção de mapas 2D e 3D em terrenos planos tais como em aplicações típicas de ambientes fechados. A representação dos mapas 2D é feita na forma de grade de ocupação. Por outro lado, a representação dos mapas 3D é feita na forma de nuvem de pontos ao invés de grade, para reduzir o custo computacional. É considerado um robô móvel equipado com apenas um LRF, sem nenhuma informação de odometria. O alinhamento entre varreduras laser é otimizado fazendo o uso de Algoritmos Genéticos. Assim, podem-se construir mapas e ao mesmo tempo localizar o robô sem necessidade de odômetros ou outros sensores. Um simulador em Matlab® é implementado para a geração de varreduras virtuais de um LRF em um ambiente 3D (virtual). A metodologia proposta é validada com os dados simulados, assim como com dados experimentais obtidos da literatura, demonstrando a possibilidade de construção de mapas 3D com apenas um sensor LRF.

Palavras-Chave

Robótica Móvel, Filtros Bayesianos, Alinhamento de Varreduras Laser, Mapeamento e Localização Simultânea, Medidor Laser de Varredura

Summary

List of figures

List of tables

List of Variables

A_t : State transition matrix

B_t : Matrix that translates control input into a predicted change in state

d : Measured data

f : function that represents the motion model in EKF-SLAM

h : function that represents the perception model in EKF-SLAM

h_j^i : function that represents the perception model for the particle i

H_j^i : The Jacobian of h_j^i at L_j

H_t : The Jacobian of h at $\overline{\lambda}_t$

Jf_{u_t} : The Jacobian of f at u_t

K_t : Kalman gain

L: Set of landmarks with known exact location

$L_{n,t}^i$: Position of landmark n, related with particle i, at time t

L_{t1} L_{t2} ... L_{tn} : n-th landmark estimated at time t

L_q : New observed landmark

η : Normalizer

$\boldsymbol{p}$: Vector of the parameters to estimate (in DE)

p_c : Probability of crossover

p_m : Probability of mutation

P_t : Covariance of the process noise

P_r : Reference robot position

P_n : New robot position

Q : Covariance matrix for the sensor noise in EKF-SLAM

$R_0, R_1, \ldots R_t$: Robot position at time t

$Rx, Ry, R\theta$: Robot position in two-dimensional planar coordinates

$R^{i,t}$: Robot path, related with particle i, until time t

S_{new} : New scan

S_{ref} : Reference scan

t_x : Translation in x

t_y : Translation in y

U : Uncertainty of the control u_t in EKF-SLAM

u_t : Control at time t

w_t^i : Weight of particle i at time t

x_t^i : Particle i at time t

Z_0, Z_1, Z_t : Map estimated at time t

x_i : Distance that the laser ray travels through the square i

x_t : State variable at time t

z_t : Sensor measurement at time t

$z_{j,t}$: The j^{th} landmark sensor observation in z_t

$\Delta x, \Delta y, \Delta\theta$: displacements that are referenced to the current robot position

λ_t : Gaussian mean at time t

$\lambda_{n,t}^i$: Mean related with the landmark position $L_{n,t}^i$

ρ_i : Opacity of the square i

Σ_t : Gaussian covariance at time t

$\overline{\Sigma}_t$, $\overline{\lambda}_t$: Predicted covariance and mean at time t

$\Sigma_{n,t}^i$: Covariance related with the landmark position $L_{n,t}^i$

φ : Rotation in z

Φ_t : Set of particles at time t

List of Abbreviations

SLAM : Simultaneous Localization and Mapping

LRF : Laser Range Finder

GPS: Global Positioning System

KF : Kalman Filter

PF : Particle Filter

EKF-SLAM : Extended Kalma Filter SLAM

FastSLAM : Fast SLAM

DP-SLAM : Distributed Particle SLAM

ICP : Iterative Closest Point

IDC : Iterative Dual Correspondence

ICL : Iterative Closest Line

HAYAI : The Highspeed and Yet Accurate Indoor/outdoor-tracking

NDT : Normal Distributed Transform

GA : Genetic Algorithm

GP : Genetic Programming

DE : Differential Evolution

LSLAM : Low SLAM

HSLAM: High SLAM

Stdv : Standard Deviation

1
Introduction and Problem Definition

1.1.
Introduction

1.1.1.
Robotics

"Robotics is the science of perceiving and manipulation the physical world through computer-controlled mechanical devices" [1].

The word *robo*t was first introduced in 1921 by the Czech novelist Karel Čapek in his satirical drama entitled: *Rossum´s Universal Robots*. It is derived from the Czech word *robota*, which literally means "forced laborer" or "slave laborer" [2]. From there this word was popularized by science fiction, assigning it to machines with anthropomorphic characteristics, fitted with action and decision capabilities, similar or higher than humans [3]. Examples of successful robotics system include mobile platforms for planetary exploration, robotics arms in assembly lines, cars traveling autonomously on highways, actuated arms that assist surgeons and so on.

Mobile robot systems operate in increasingly unstructured environments, inherently unpredictable. "As a result, robotics is moving into areas where sensor input becomes increasingly important, and where robot software has to be robust enough to cope with a range of situations – often too many to anticipate them all" [1]. Robotics is becoming a software science, where the target is to develop sturdy software that enables robots to overcome the numerous challenges in unstructured and dynamic environments.

1.1.2. Uncertainty in Robotics

Uncertainty in robotics arises from five different factors [1]:

1. **Environment**. Environments such as private homes and highways are highly dynamic and unpredictable

2. **Sensors**. Limitation in sensors arises from their range and resolution. In addition, sensors are subject to noise.

3. **Robots**. "Robot actuation involves motors that are, at least to some extent, unpredictable, due to effects such as control noise and wear-and-tear" [1].

4. **Models**. Models are idealization of the real world. They only partially model the physical processes of the robot and its environment.

5. **Computation**. "Robots are real-time systems, which limits the amount of computation that can be carried out" [1]. Many algorithms are approximate, reaching timely response through slaughtering accuracy.

"Traditionally such uncertainty has mostly been ignored in Robotics" [1]. However, as robots are moving away into increasingly unstructured environments, the ability to deal with uncertainty is crucial for building successful systems.

1.2. Problem Definition

The scope of this work is related to the SLAM problem. SLAM (Simultaneous Localization and Mapping) is one of the most widely researched subfields of robotics, in special in mobile robotic systems.

Let's consider a mobile robot which is using wheels connected to a motor, actuators and a camera. Consider that the robot is manipulated by an operator mapping inaccessible places. The actuators allow the robot to move around, and the camera provides visual information for the operator to know where objects are and how the robot is oriented in reference to them. What the human operator is doing is an example of SLAM.

“Thus, the SLAM subfield of Robotics attempts to provide a way for robots to perform SLAM autonomously. A solution to the SLAM problem would allow a robot to make maps without any human assistance whatsoever” [4].

In the following, the SLAM idea is graphically presented (example taken from [4]).

1.2.1. Localization overview

Let’s consider a mobile robot in an environment which contains beacons or landmarks (points in the environment with a known exact location) from which the robot can calculate its distance and direction. Assume that the robot starts in some true known location R_0 (e.g. the red filled circle in Figure 1.1), and it has knowledge of a set L containing several landmark locations. When the robot moves a given distance in a certain direction (the movement vector u_1) to location R_1, it actually moves along some other vector to some location R'_1 which is nearby R_1, due to uncertainties in the actuators. Landmarks need to be relocated to determine the new robot position. Because the actuators are imprecise, the landmarks could not be reacquired by assuming they have moved inversely to u_1. Thus, the robot must search for the landmarks, starting near the expected location of the landmark and expanding outwards. Figure 1.1 presents this situation.

Note that R'_1 and vector u'_1 correspond to estimates rather than the actual values. Once the landmarks are reacquired, a new robot location estimate, R_1, can be made as shown in Figure 1.2.

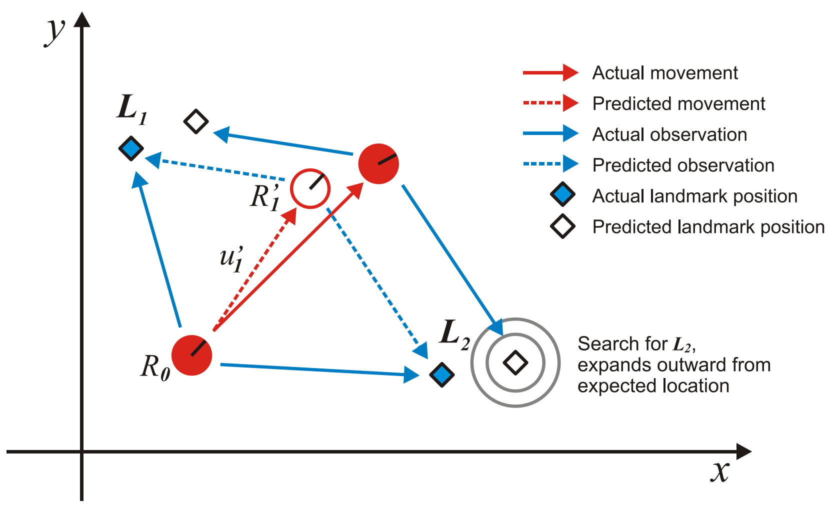

Figure 1.1: Localization Overview (search for landmarks)

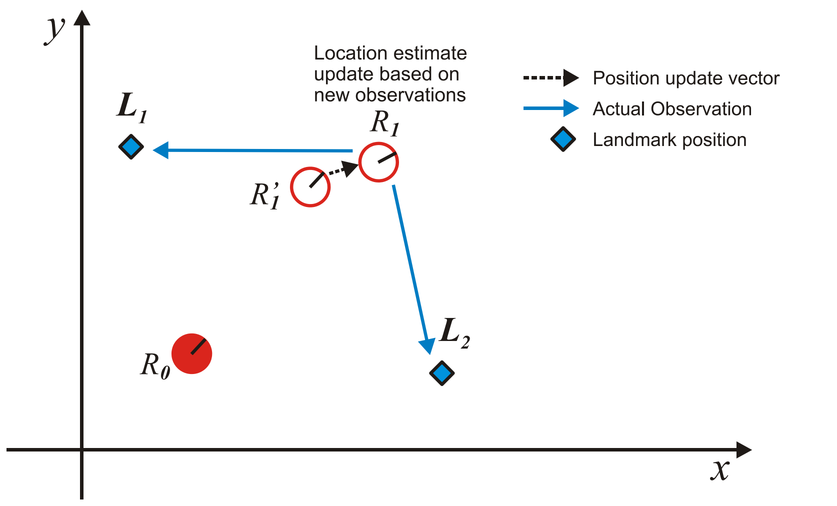

Figure 1.2: Localization Overview (location updated)

It is important to stress that R_1 is the location updated based on new observations, and therefore it is an estimated (white filled circle) robot position rather than the true position (red filled circle), which is impossible to perfectly measure.

1.2.2. Mapping overview

Mapping is, in a way, the opposite of localization. In mapping, it is assumed that the robot exactly knows where it is at all times. What the robot does not know, in the mapping context, is the locations of landmarks. Thus, the robot must locate landmarks to build a map $Z_t=\{L_{t1}\ L_{t2}\ \ldots\ L_{tn}\}$, where L_{tn} is the n^{th} landmark estimate at time step t. Of course Z_t only contains approximations of the actual landmark locations. As the robot moves, the map is usually more accurate.

Let's follow the same example from the previous section, beginning at $\boldsymbol{R_0}$ and moving along $\boldsymbol{u_1}$ to $\boldsymbol{R_1}$. The robot will acquire the set of landmarks, but in this situation the perceived landmarks locations will have shifted from their expected location due to sensor inaccuracies instead of odometry inaccuracies. The landmarks can be relocated by searching nearby where the robot expects to find them. Thus, the robot will have built a new map Z_1, consisting of new locations of the landmarks in Z_0. Figure 1.3 demonstrates the process. For simplicity, in this example preservation of landmarks is assumed; in reality some landmarks are lost and new landmarks are acquired.

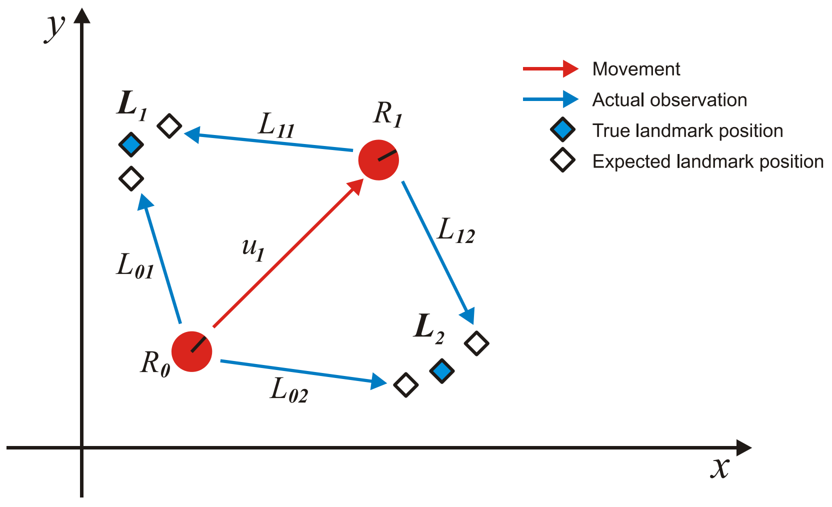

Figure 1.3: Mapping Overview

To generate a new map, Z_2, combining information of Z_0 and Z_1 but containing only one instance of each landmark, the robot can choose one of many options. For example, it can choose any point on the line connecting L_{0n} and L_{1n} (note that L_{0n} and L_{1n} are two conflicting perceived locations of landmark n).

Whichever the method selected for incorporating new sensor readings, it seems safe to assume that Z_t will improve as time t increases.

1.2.3. Simultaneous Localization and Mapping

The Localization Overview and the Mapping Overview presented before require something as an input that is unavailable in practice. Localization requires accurate landmark locations as input and conversely Mapping requires exact robot localization. This suggests that the two processes are related and could be combined into a single solution.

Suppose a robot starts moving from some known origin. It uses the Mapping process to construct a preliminary map. It then moves to a new location and updates its expected location as in Localization step. Finally, the new calculated pose is used to once again generate a new map, which is combined with the original map as described in Section 1.2.2. By repeating this process, one can provide a map for input into the Localization, and a location for input into the Mapping. Figure 1.4 demonstrates the basic Simultaneous Localization and Mapping idea.

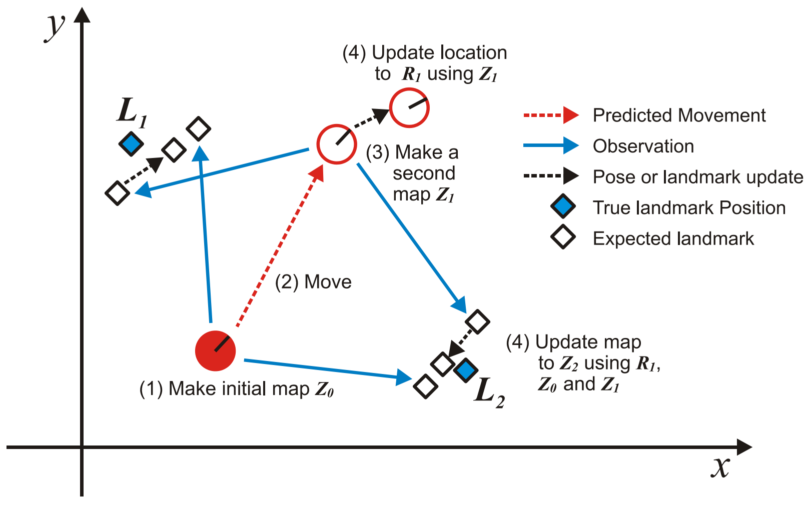
y
x
L_1
L_2
(4) Update location to R_1 using Z_1
(3) Make a second map Z_1
(2) Move
(1) Make initial map Z_0
(4) Update map to Z_2 using R_1, Z_0 and Z_1
Predicted Movement
Observation
Pose or landmark update
True landmark Position
Expected landmark

Figure 1.4: Simultaneous Localization and Mapping

One thing to notice with this combined localization and mapping algorithm is that one does not provide completely accurate input to either the mapping or the localization components.

1.3. Motivation

Petrobras operates in oil and gas exploitation at Amazon, in the province of Urucu (AM), at the Solimões River, about 650 km from Manaus City. To drain this production, it has been built two gas pipelines: Coari-Manaus and Urucu Porto Velho, with 420 Km of extension from Manaus as well.

In order to monitor these almost one thousand kilometers of pipeline in a hard access region and to avoid environment disasters, it was built a robotic amphibian vehicle, named Hybrid Environmental Robot (HER).

HER is able to move in many different grounds of Amazon: water, ground and aquatic microfiber, and it is also able to monitor different scenarios using many sensors, as shown in Figure 1.5. Moving into such an extended and remote areas and collecting data samples has become an important issue; thus, a precise position perception is needed, allowing the possibility for navigation and demarcation in areas of interest.

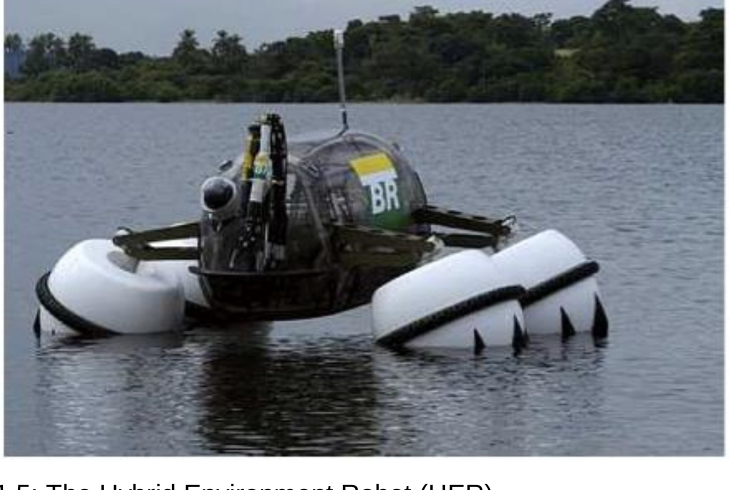

Figure 1.5: The Hybrid Environment Robot (HER)

HER acquires its position using a GPS system. However, it is prone to failure because of obstructions in satellite signal, caused by local vegetation. In this case, HER needs to acquire its position in a different way, in order to continue its mission or to search places with better satellite reception. The use of odometers is not a good choice due to frequent slipping on the ground; beyond, it does not have any utility over water. Localization by cameras also does not presents good results due to high similarity between vegetation images, making hard a reliable keypoints establishment. Inertial platforms would help in the localization of the robot, but would not have any utility to detect obstacles.

So, the use of a Laser Range Finder (LFR) represents great advantages, cause it is able, not only to locate the robot or mapping the environment, but also to detect obstacles on the robot´s path.

1.4. Objective

The objective of this work is to perform SLAM with limited sensor capabilities. More specifically, it is shown that localization and mapping can be performed without odometry measurements, just by using a single Laser Range Finder (LRF).

To accomplish that, first a detailed explanation of SLAM algorithms implementations is given, focusing on the: EKF-SLAM, FastSLAM, and DP-SLAM methods. Then, a Genetic Algorithm is implemented for Normal Distribution Transform (NDT) optimization, in order to obtain robot displacement without odometry information. An implementation for 3D mapping is shown, using DP-SLAM, which does not use predetermined landmarks (not dealing either with data association problems). Finally a virtual 3D environment is simulated including virtual Laser Range Finder (LRF) readings, to validate the presented methodology. Experimental data from actual LRF readings are also used to evaluate the performance of the algorithms.

1.5. Organization of the Thesis

This thesis is divided into six chapters, described as follows:

Chapter 2 comprises the theory necessary for Probabilistic Robotic. The basic concepts of representing uncertainties in a planar robot environment are shown. Also the main algorithms for scan matching are given, emphasizing on the Normal Distribution Transform(NDT). Concluding with Genetic Algorithms and Differential Evolution (DE).

Chapter 3 describes the principal algorithms for the SLAM solutions, including EKF-SLAM, FastSLAM and DP-SLAM. Besides, is presented a review for 3D SLAM solutions and 3D mapping.

Chapter 4 gives a detailed implementation of the principal SLAM solutions: EKF-SLAM, FastSLAM and DP-SLAM. Is explained also, the simulated Laser Range Finder (RLF) in a structured environment, developed for testing the proposed methods. In addition, is explained the NDT optimization using Differential Evolution, in order to get robot displacements without odometry information.

Chapter 5 presents the results obtained in simulated and real data acquired from the literature.

Chapter 6 presents comments and conclusions to the performed work.

2.
Theoretical Basis

2.1.
Probabilistic Robotics

“The key idea of Probabilistic Robotics is to represent uncertainty explicitly, using the calculus of probability theory” [1]. In other words, instead of relying on a single “best guess” probabilistic algorithms represent information by probabilistic distributions. By doing so, probabilistic robotics can mathematically represent ambiguity and degree of belief, enabling them to accommodate all sources of uncertainty.

The advantage of probabilistically programming robots, compared to other approaches that do not explicitly represent uncertainty, is simply because:

> *“A robot that carries a notion of its own uncertainty and that acts accordingly is superior to one that does not.”* [1].

Probabilistic approaches are typically more robust under sensor limitation, sensor noise, environment dynamics, and so on. They are well suited to complex and unstructured environments, where the ability to deal with uncertainty is quite important. “Probabilistic algorithms are broadly applicable to virtually every problem involving perception and action in the real world” [1].

All these advantages, however, come at a price. The two most cited limitations of probabilistic algorithms are: a need to approximate and computational inefficiency. Because probabilistic algorithms consider entire probability densities, they are less efficient than non-probabilistic ones. Computing exact posterior distributions is typically infeasible, since distributions over the continuum possess infinitely many dimensions (most robot worlds are continuous). Sometimes, uncertainty can be approximated with a compact parametric model (e.g. discrete distributions or Gaussians); in other cases, a more complicated representations most be employed.

“At the core of probabilistic robotics is the idea of estimating state from sensor data” [1]. This sensor data are not directly observable, but that can be inferred. A robot has to rely on its sensors to gather information, while this information is only partial, and corrupted by noise. Thus, state estimation seeks to recover state variables from data.

2.1.1. Bayes Filter and SLAM

In Probabilistic Robotics, all quantities related in estimation such as sensor measurements, controls, state of the robot and its environment might be modeled as random variables. Random variables can take on multiple values, and they behave according to probabilistic laws. Probabilistic inference is the process of calculating these laws.

“Bayes rule is the archetype of probabilistic inference” [5]. It plays a predominant role in probabilistic robotics. Therefore, it is the basic principle underlying virtually every single successful SLAM algorithm. The Bayes rule is stated as [1]:

$$p(x \mid d) = \eta\, p(d \mid x) p(x) \tag{2.1}$$

If the quantity to learn is x (e.g. a map), using measurement data d (e.g. odometry, range scans), then Bayes rule tells that the estimation problem can be solved by multiplying two terms: $p(x|d)$ and $p(x)$. The term $p(x|d)$ is a generative model, it describes the process of generating sensor measurements under different worlds x. The term $p(x)$ is called the prior. It specifies the willingness before the arrival of any data. Finally, η is a normalizer that is necessary to ensure that the left- hand side of Bayes rule is indeed a valid probability distribution [5].

In robotic mapping there are two different types of data: sensor measurements and controls. Let´s denote sensor measurement (e.g. camera images, LRF scans) by the variable *z*, and the control (e.g. motion command, odometry) by *u*. Let us assume that the data is collected in alternation:

$$z_1, u_1, z_2, u_2, ... \tag{2.2}$$

where subscripts are used as time index.

"In the field of robot mapping, the single dominating scheme for integrating such temporal data is known as Bayes Filter" [5].

The Bayes Filter is the extension of Bayes rule to temporal estimation problems[5]. It is a recursive estimator to compute posterior probability distributions over quantities that cannot be observed directly – such as a map or robot position. Let's call this unknown quantity the state x_t, where *t* is the time index. The generic Bayes filter calculates a posterior probability over the state x_t using the recursive equation [1]:

$$p(x_t \mid z^t, u^t) = \eta \, p(z_t \mid x_t) \int p(x_t \mid u_t, x_{t-1}) p(x_{t-1} \mid z^{t-1}, u^{t-1}) dx_{t-1} \tag{2.3}$$

where the superscript ^{t} refers to all data leading up to time *t*, that is:

$$z_t = \{z_1, z_2, \ldots, z_t\} \tag{2.4}$$

$$u_t = \{u_1, u_2, \ldots, u_t\} \tag{2.5}$$

Note that Bayes filter is recursive, that is, the posterior probability $p(x_t|z^t,u^t)$ is calculated from the same probability one time step earlier. The initial probability at time $t = 0$ is $p(x_0|z^0,u^0)=p(x_0)$.

In the context of robotic mapping the state x_t contains all unknown quantities that are typically two: the map and the robot's pose in the environment. When using probabilistic techniques, the mapping problem is one where both the map and the robot pose have to be estimated in the same time altogether. Using *m* to denote the map and *R* for the robot's pose, the following Bayes Filter is obtained [1]:

$$p(R_t, m_t \mid z^t, u^t)$$
$$= \eta\, p(z_t \mid R_t, m_t) \iint p(R_t, m_t \mid u_t, R_{t-1}, m_{t-1})\, p(R_{t-1}, m_{t-1} \mid z^{t-1}, u^{t-1})\, dR_{t-1} dm_{t-1} \qquad (2.6)$$

If assumed a static world, the time index can be omitted when referring to the map *m*. Also, most approaches assume that the robot motion is independent of the map. And finally, using the Markov assumption, which postulates that past and future data are independent if one knows the current state x_t, the state x_t can be estimated using only the state x_{t-1} one step earlier. This results in a convenient form of the Bayes Filter for the robot mapping problem [5]:

$$p(R_t, m \mid z^t, u^t)$$
$$= \eta\, p(z_t \mid R_t, m) \int p(R_t \mid u_t, R_{t-1})\, p(R_{t-1}, m \mid z^{t-1}, u^{t-1})\, dR_{t-1} \qquad (2.7)$$

This estimator does not require integration over maps *m*, as it was the case for the previous one from eq. (2.6). The static world assumption is quite important, because such integration is difficult due to the high dimensionality of the space of all maps.

In eq. (2.7) two distributions probabilities have to be specified: $p(R_t|u_t, R_{t-1})$ and $p(z_t|R_t,m)$. Both are generative models of the robot and its environment.

The probability distribution $p(R_t|u_t, R_{t-1})$, often called to as *motion model*, specifies the effect of the control *u* on the state. It describes the probability that the control *u*, if executed at the world state R_{t-1}, leads to the state R_t.

The probability $p(z_t|R_t,m)$, often called to as *perception model*, describes in probabilistic terms how sensor measurements *z* are generated for different poses R_t and maps *m*.

However, eq. (2.7) cannot be implemented on a digital computer in its general stated form. This is because the posterior over the space of all maps and robot poses is a probability distribution over a continuous space, hence possesses infinitely many dimensions. Therefore, any working mapping algorithm has to take additional assumptions. These assumptions and their implications on the resulting algorithms and maps constitute the main differences between the different solutions to the SLAM.

Figure 2.1 shows a generative probabilistic model (dynamic Bayes network) that underlies the essential of SLAM.

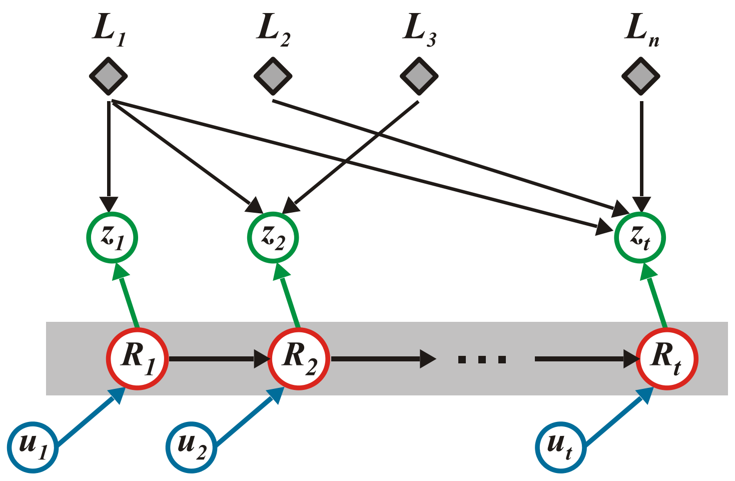

Figure 2.1: SLAM like a Dynamic Bayes Network

In particular, the robot poses, denoted by R_1, R_2, …, R_t, evolve over time as a function of the controls, denoted by u_1, u_2, …, u_t. The map is composed (as it will be seen later) by landmarks and each measurement of them, denoted by z_1, z_2, …, z_t, which are a function of its position L_1, L_2, …, L_n and of the robot pose at the time the measurement was taken.

Note that in this SLAM equation analysis the odometery u_t is assumed to be known, and this assumption will be kept till the Section 4.5.1 where odometry is replaced by Scan Matching.

2.1.2. Motion Model

“Robot motion models play an important role in modern robotics algorithms” [6]. The main purpose of a motion model is to model the relationship between a control input to the robot and a change in the robot´s configuration, pose and map. Good models will capture not only systematic errors, but it will also capture the stochastic nature of the motion. The same control input will almost never produce the same result. "Thus, the effects of a robot's action are, therefore, best described as distributions" [6].

This thesis focuses entirely on kinematics for mobile robots operating in planar environments. Kinematics describes the effect of control actions on the configuration of a robot. A rigid mobile robot is commonly described by six variables, its three-dimensional Cartesian coordinates and its three Euler angles (roll, pitch, yaw) referred to an external coordinate frame. But in a planar environment, the position of a mobile robot is summarized by three variables: its two-dimensional planar coordinates referred to an external coordinate frame, along with its angular orientation.

$$R = \begin{pmatrix} Rx \\ Ry \\ R\theta \end{pmatrix} \tag{2.8}$$

Figure 2.2 illustrates a robot pose in a plane.

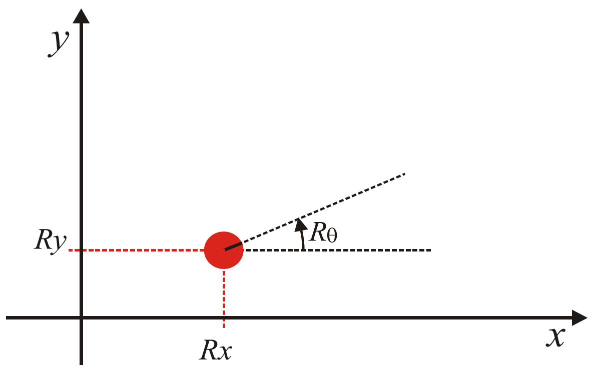

Figure 2.2: Robot pose

The orientation of a robot is often called *bearing*, or *heading direction.*

The probabilistic kinematic model, or *motion model*, plays the role of the state transition model in Mobile Robotics. As described in the previous section, this model is the probability distribution:

$$p(R_t \mid u_t, R_{t-1}) \tag{2.9}$$

Figure 2.3 shows two examples that illustrate the motion model for a rigid mobile robot in a planar environment. The robot's initial pose, in both cases, is R_{t-1}. The distribution $p(R_t|u_t, R_{t-1})$ is visualized in the form of a gray shaded area: darker areas mean more probability in robot position. In both figures, the robot moves forward some distance, during which it may accumulate translational and rotational errors. The right figure shows a larger spread of uncertainty due to a more complicated motion.

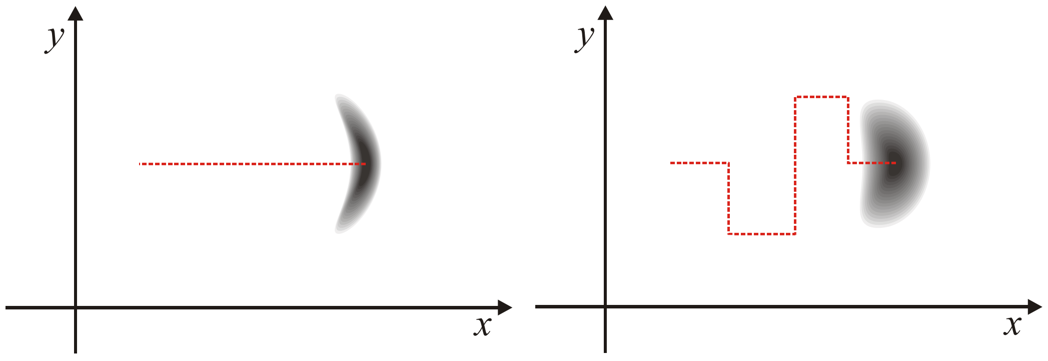

Figure 2.3: The motion model, showing posterior distributions of the robot's pose after executing the motion command u_t (red striped line). The darker a location, the more likely it is.

There are two motion models usually used. "The first model assumes that the motion data u_t specifies the velocity commands given to the robot's motors" [1]. Many commercial mobile robots (e.g. differential drive, synchro drive) are actuated by independent translational and rotational velocities. The second model, which is used in this work, assumes that u_t contains odometry information (distance traveled, angle turned).

However, odometry is only available as the robot moves. Hence it cannot be used for motion planning, such as collision avoidance [1]. “Technically, odometry are sensor measurements, not controls” [1]. But it is common to simply consider odometry as if it was a control input signal.

2.1.3. Perception Model

“The perception model comprises the second domain-specific model in probabilistic robotics, next to the motion model” [1]. In probabilistic terms, the Perception Model describes how sensor measurements *z* are generated for different poses *R* and maps *m*. As described before, this is modeled by:

$$p(z_t \mid R_t, m) \tag{2.10}$$

The Perception Model account for the uncertainty in the robot’s sensors. Thus, it explicitly models noise in sensor measurement. It could say that better results are acquired by a more accurate Perception Model. However, it is almost impossible to accurately model a sensor; reference [1] gives two primarily reasons[1]: “First, developing an accurate perception model can be extremely time-consuming; and second, an accurate model may require state variables that are not known, such as the surface material” [1]. In this way Probabilistic Robotics, instead of modeling the Perception Model by a deterministic function $z=f(x)$, accommodates the inaccuracies of Perception Model by a conditional probability density, $p(z|x)$. “Herein lies a key advantage of probabilistic techniques over classical robotics” [1].

Figure 2.4 shows a robot in an environment getting measurements from its Laser Range Finder (LRF). Given a position and the map of the environment, it is possible to use ray-tracing to get expected measurements for each rangefinder angle.

The result of modeling the sensor is shown in Figure 2.5. For a particular expected distance, the sensor will give a value near that distance with some probability. So, given an actual measurement and an expected distance, it is possible to find the probability of getting that measurement using the graph from Figure 2.5.

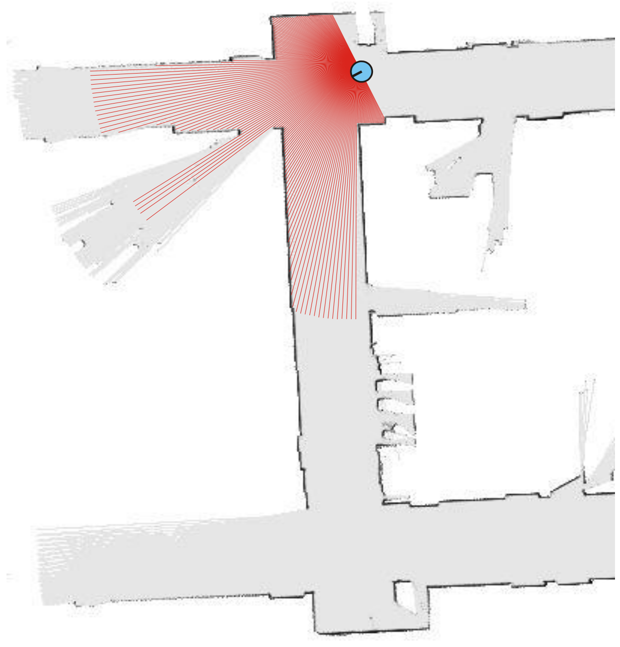

Figure 2.4: Robot in a map getting measurements from its LRF.

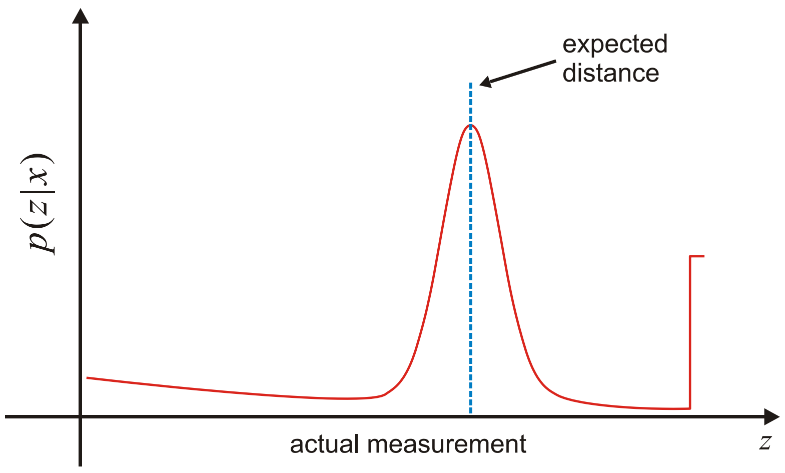

Figure 2.5: Given an actual measurement and an expected distance, the probability of getting that measurement is given by the red line in the graph.

Today’s robots use a variety of sensor types, such as tactile sensors, range finder sensors, sonar sensors or cameras. The model specifications depend on the sensor type.

2.2. Map Representation

There are many reasons to have a representation of the robot’s environment. Some of the purposes of having a map are listed in the following:

- **Localization.** The robot localization is possible making a correspondence between a given map and the observation of the robot’s environment.
- **Motion planning.** Once the robot is located and given a target position, all necessary movements in the map can be compute to successfully move to the target.
- **Collision avoidance.** Using a map and robot’s localization the navigation is possible without collisions.
- **Human use.** The map constructed by the robot can be used for exploration tasks in potentially hazardous environments.

In general, the map representation can be grouped into three main types: Geometric, Topological and Hybrid. However the general tendency in SLAM is to use geometric representation. Thus, this representation has also a subdivision: Landmark (or feature maps) and Grid maps.

2.2.1. Landmark Maps

The landmark-based maps consist of a set of distinctive point localizations that are referred to a global reference system. In structured domains such as indoor environments, landmarks are usually modeled as geometric primitives such as points, lines or surfaces.

The main advantage of landmark-base maps is their representation compactness. By contrast, this kind of map requires the existence of structures or objects that are distinguishable enough from each other. Thus, an extra algorithm for recognizable and repeatedly detectable landmark extraction is needed.

In practice, good landmarks may have similar traits, which often make them difficult to distinguish from each other. When this happens the problem of data association, also known as the *correspondence problem*, has to be addressed. “The correspondence problem is the problem of determining if sensor measurements taken at different points in time correspond to the same physical object in the world” [5]. It is a difficult problem, because the number of possible hypotheses can grow exponentially.

Figure 2.6 shows a simulated landmark-based map, where the blue asterisks represent the landmarks and the small triangle the robot position.

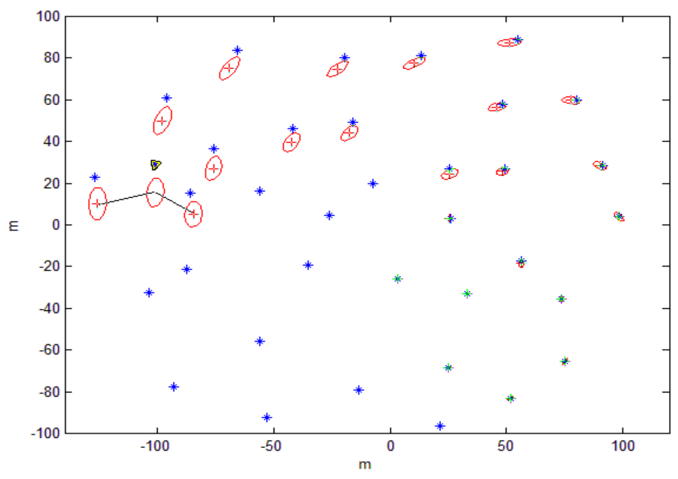

Figure 2.6: Simulated Landmark Map

2.2.2. Grid Maps

A grid map, or occupancy grid, is a popular and intuitive method to describe an environment. Occupancy grids were originally developed at Carnegie Mellon University in 1983 for sonar navigation within a lab [7].

Occupancy grids divide the environment up into a regular grid square, all of equal size. “Each of these grid squares correspond to a physical area in the environment and, as such, each square contains a different set of objects or portions of an object” [6]. An occupancy grid is an ideal representation of the environment, containing information on whether a square in the real environment is occupied or not.

The occupancy grid representation can be generalized into two types: deterministic and stochastic [6], described as follows.

- Deterministic map grids are the simplest representation, having two values for each grid square. Typically squares are considered as either Empty or Occupied, also sometimes is include a value for Unknown (or Unobserved). However, this representation is an exaggerated simplification for the sensors, since almost never a sensor will see a square of the environment which is both completely occupied and accurately observed.

- Stochastic maps, besides of Occupied and Empty, have a gradual scale of various degrees of occupancy. What percentage of the square is believed to be occupied, or how transparent the object is to the sensor are some factors that affect the occupancy value. The stochastic representation and the corresponding observation model need to be properly tuned for the sensor used.

Figure 2.7 shows a stochastic grid map, where the occupancy of each square is given in gray scale color, and darkest squares mean high probability of occupancy.

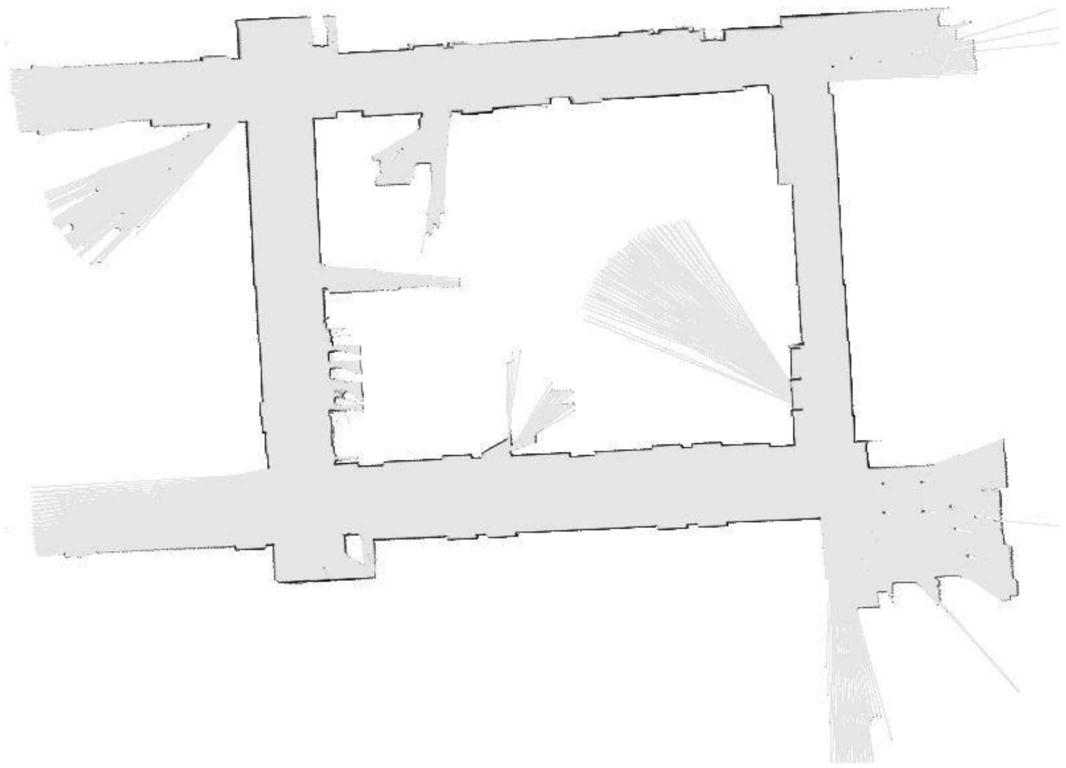

Figure 2.7: Grid Map: White regions mean unknown areas, light gray represents unoccupied areas, and darker gray to black represent increasingly occupied areas.

This work uses occupancy grid maps for environment representation, specifically stochastic occupancy grid maps.

2.3. Scan Matching

“Many SLAM algorithms are based on the ability to match two range scans or to match a range scan to a map” [8]. Laser Range Fiders (LRF) are popular sensors to get the input for scan matching, since their high reliability and their low noise in many situations.

The goal of scan matching is to find the relative displacement between the two positions at which the scans were taken. If a robot starts at position P_r (which is a reference pose), takes a scan S_r (reference scan), after that it moves through a static environment to a new pose P_n and takes another scan S_n (new scan), then scan matching seeks the difference of position P_n from posistion P_r (the relative translation and rotation) by aligning the two scans.

“The basis of most successful algorithms is the establishment of correspondences between primitives of the two scans” [8], i.e. point-to-point or feature-to-feature.

Different routines are developed to use point-to-point matching approaches such as the Iterative Closest Point (ICP) and the Iterative Dual Correspondence (IDC), both proposed by Lu and Milios [9]; and another, The Iterative Closest Line (ICL) proposed by Alshawa [10].

In [11] it is proposed a method that searches for features like corners and jump-edges from raw range scans. Another method based on feature extraction is HAYAI proposed in [12]. This method solves the self-localization problem for high speed robots.

One method that does not use correspondences between scans is the Normal Distribution Transform proposed in [8]. This method transforms the discrete set of 2D points reconstructed from a single scan into a piecewise continuous differentiable probability density defined on the 2D plane.

This work uses the NDT for scan matching but without using odometry information. But before getting to it; let’s briefly review some of methods used for scan matching including NTD.

2.3.1. Point to Point Correspondence Methods.

- **The Iterative Closest Point (ICP)**

  The most general matching point to point approach was introduced by Lu and Milios in [9]. This is essentially a variant of the ICP (Iterative Closest Point) algorithm applied to laser scan matching.

  A scan is a sequence of points which represent a 2D plane contour of the local environment. “Due to the existence of random sensing noise and self-occlusion, it may be impossible to align two scans perfectly” [9]. Thus this method assumes two types of discrepancies between scans:

- in the first type, there are small deviations of scan points from the true contour due to random sensing noise, and
- the other type of discrepancy is the gross difference between the scans caused by occlusion. These discrepancy types are called outliers.

Adopting these criterions, ICP finds the best alignment of the overlapping part in the sense of minimum least-square errors, while ignoring the outlier parts. That is way ICP also need of correspondence search and outlier detection algorithms.

Lu and Milios [9] present two scan matching methods based on ICP. The first considers the two components (rotational and translational) separately; alternately fixing one, then optimizing the other. Given the rotation, least-square optimization is used to acquire translation.

Their second method called Iterative Dual Correspondence (IDC) combines two ICP-like algorithms with different point-matching heuristics.

- **The Iterative Closest Line (ICL)**

“ICL is similar to ICP, except that instead of matching query points to reference points, the query points are matched to lines extracted from the reference points” [13].

2.3.2. Feature to Feature Correspondence Methods.

- **Feature Based Laser Scan Matching for Accurate and high speed Mobile Robot Localization.**

Proposed by Aghamohammadi *et al.* [11]. This method divides the features into two types: features corresponding to the jump-edges and those corresponding to the corners detected in the scan**.**

In order to detect jump-edges, this method uses the natural consecutive order of points in the scan. Thus it defines a d_{th} which is the maximum distance between two consecutive scan points. Beyond d_{th} these two consecutive points can be considered as jump-edges.

To obtain the second class of features, the corners, this method uses a line fitting algorithm. Thus the split-and-merge algorithm is used but only for line fitting. In this way, using two points taken of two consecutive lines, it searches for the farthest point to the straight line joining these two points.

Finally, after extracting features for two consecutive scans, a matching algorithm, based on a dissimilarity function is calculated.

This method is fast and it can be used for high speed mobile robot, but it suffers when the environment does not have corners or when it has circular walls, because no corners could be extracted and false jump-edges could be acquired.

- **The Highspeed and Yet Accurate Indoor/outdoor-tracking (HAYAI)**

HAYAI was proposed by Lingemann *et al.* [12]. This uses the inherent order of the scan data, allowing the application of linear filters for fast reliable feature detection.

Thus, this method chooses *extrema* in the polar representation of a scan as natural features. These *extrema* correlate to corners and jump-edges in Cartesian space. The usage of polar coordinates implicates a reduction by one dimension, since all operations deployed for feature extraction are fast linear filters.

For feature detection, HAYAI filters the scan signal using three one dimensional filters $\boldsymbol{\psi} = [\psi_{-1}, \psi_0, \psi_{+1}]$.The first one sharpens the data in order to emphasize the significant parts of the scan. The second one computes the derivation signal using a gradient filter. And, the last one smoothes the gradient signal to simplify the detection of zero crossing using a softening filter.

After generating the sets of features from both scans, the matching between both sets is calculated. But instead of solving the hard optimization problem of searching for an optimal match, HAYAI uses a heuristic approach, utilizing inherent knowledge about the problem of matching features, e.g., “the fact that the features topology cannot change fundamentally from one scan to the following” [12].

“Although this method is a fast and feature based method for scan matching, it suffers from the lack of satisfying robustness property of feature extraction. It is well-suited for high range sensors” [11].

2.3.3. The Normal Distribution Transform

The assumed correspondences between two scans captured from two different poses of the robot are generally not true. That is why Biber [8] proposed a new method that does not need correspondences. Thus NDT makes an occupancy grid and subdivide the 2D plane into cells. To each cell, it assigns a normal distribution, which models the probability of measuring a point. “The result of the transform is a piecewise continuous and differentiable probability density, that can be used to match another scan using Newton’s algorithm” [8].

This work uses the NDT for scan matching, which will be explained in detail next.

The NDT representation of one scan is built as follows: first, it subdivides regularly into cells of constant size the 2D space around the robot. Then, for each cell that contains at least three points:

1. collects all 2D-Points $x_{i=1\ldots n}$ contained in this cell.
2. calculates the mean:

$$\boldsymbol{q} = \frac{1}{n}\sum_i x_i \tag{2.11}$$

3. calculates the covariance matrix

$$\Sigma = \frac{1}{n}\sum_i (x_i - \boldsymbol{q})(x_i - \boldsymbol{q})^T \tag{2.12}$$

The probability of a 2D-point x contained in this cell is now modeled by the normal distribution $N(\boldsymbol{q},\Sigma)$:

$$p(x) \sim \exp\left(-\frac{(x-\boldsymbol{q})^T \Sigma^{-1} (x-\boldsymbol{q})}{2}\right) \tag{2.13}$$

Unlike to occupancy grid that represents the probability of a cell being occupied, the NDT represents the probability of measuring a point for each position within the cell. NDT proposes a cell size of 1000 mm by 1000 mm and this value will be adopted in this work.

To minimize discretization effects, NDT uses four overlapping grids as follows: one grid with side length $\boldsymbol{l}$ of a single cell is place first, then a second one, shifted by half cell horizontally, a third one, shifted by half vertically and finally a fourth one, shifted by half horizontally and vertically. In this way, each 2D point falls into four cells. Thus, if the probability density of a point is calculated the densities of all four cells are evaluated and the result is summed up.

Figure 2.8 shows an example laser scan and a visualization of the resulting NDT. This visualization is created by evaluating a fine mesh of points; bright areas indicate high probability of being occupied.

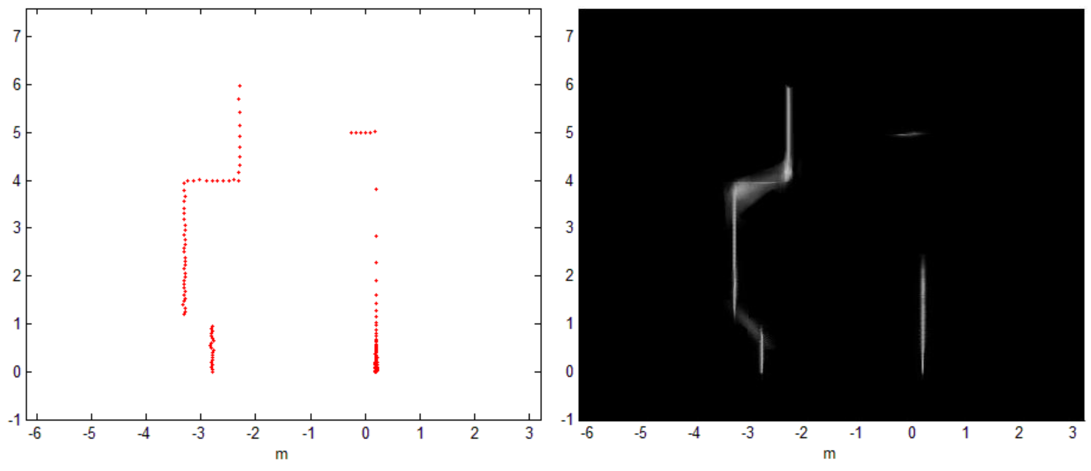

Figure 2.8: An example of NTD: the original laser scan (left) and the resulting probability density (right).

The spatial transformation *T* between two robot positions is given by:

$$T: \begin{pmatrix} x' \\ y' \end{pmatrix} = \begin{pmatrix} \cos\phi & -\sin\phi \\ \sin\phi & \cos\phi \end{pmatrix} \begin{pmatrix} x \\ y \end{pmatrix} + \begin{pmatrix} t_x \\ t_y \end{pmatrix} \tag{2.14}$$

where t_x and t_y describes the translation and φ the rotation between the two positions. As described in Section 2.3 the goal of the scan matching is to recover these values using the laser scans taken at two positions. The outline of NTD, given two scans, is as follows:

1. first, the NDT of the first is built;
2. a estimate for the variables (t_x ,t_y ,φ), is initialized (by zero or by using odometry data);
3. for each point of the second scan: a reconstructed 2D point into the coordinate frame of the first scan is mapped, according to the value of variables;
4. the corresponding normal distribution for each mapped point is determined;
5. the score for the variables is determined by evaluating the distribution for each mapped point and summing the result;
6. a new estimate for variables are calculated by trying to optimize the score, this is done by performing one step of Newton's Algorithm, and
7. go to step 3 until a convergence criterion is met.

The steps one to four are straightforward. The remaining is described using the following notation:

- $\boldsymbol{p} = (t_x, t_y, \varphi)^T$: the vector of the variables to estimate.
- x_i : the reconstructed 2D point of laser scan point *i* of the second scan in the coordinate frame of the second scan.

- x'_i : the point x_i mapped into the coordinate frame of the first scan according to the vector ***p***, that is $x'_i = T\,(x_i\,, \boldsymbol{p})$
- Σ_i , $\boldsymbol{q_i}$: the covariance matrix and the mean of the corresponding normal distribution to point x'_i looked up in the NDT of the first scan.

"The mapping according to ***p*** could be considered optimal, if the sum evaluating the normal distribution of all points x'_i with parameters Σ_i and $\boldsymbol{q_i}$ is a maximum" [8]. NDT calls this sum the score of ***p***, defined as:

$$score(\boldsymbol{p}) = \sum_i \exp\left(-\frac{(x'_i - q_i)^{\mathrm{T}} \Sigma_{\mathrm{i}}^{-1} (x'_i - q_i)}{2} \right) \tag{2.15}$$

NDT normalization problems are described as minimization problems, thus NDT adopts its notation to this convention. Therefore the function to minimize is the negative of *score*.

NDT uses Newton's algorithm iteratively to find the vector ***p*** = $(t_x\,, t_y\,, \varphi)^T$ that minimizes the function ***f*** = –*score*. Each iteration solves the equation:

$$\mathbf{H}\Delta\boldsymbol{p} = -\boldsymbol{g} \tag{2.16}$$

where ***g*** is the transposed gradient of ***f*** with entries

$$g_i = \frac{\partial f}{\partial p_i} \tag{2.17}$$

and **H** is the Hessian of ***f*** with entries

$$H_{i\,j} = \frac{\partial f}{\partial p_i\, \partial p_j} \tag{2.18}$$

The solution of this linear system is an increment $\Delta\boldsymbol{p}$ which is added to the current estimate:

$$\boldsymbol{p} \leftarrow \boldsymbol{p} + \Delta\boldsymbol{p} \tag{2.19}$$

2.4. Genetic Algorithms

The Genetic Algorithm (GA) is a search heuristic that imitates the process of natural evolution; this heuristic is routinely used to generate useful solutions to optimization and search problems. Problem solving using genetic algorithms isn´t new, the pioneering work of J. H. Holland in the 1970’s [14] showed significant contribution for engineering applications.

GA´s are inspired by a biological process in which best individuals are likely to be the winners in a competing environment. The potential solution of a problem is an individual which can be represented by a set of variables. These variables are considered as the genes of a chromosome and they are usually structured by a sequence of bits. A positive value (known as *fitness value*), obtained by a *Fitness Function*, reflects the degree of “quality” of the chromosome in order to solve the problem, and this value is narrowly related to its *objective value*.

In the process of a genetic evolution, a chromosome with high quality has the tendency to produce good-quality offsprings, which means better solutions to the problem. “In a practical application of GA, a population pool of chromosomes has to be installed, which can be randomly set initially” [15]. In each cycle of genetic process, a subsequent generation is created from the best chromosomes in the current population. This group of chromosomes, generally called “parents”, are selected via a specific selection routine. The roulette wheel selection [16] is one of the most commonly used techniques to provide selection mechanism; this selection is based on the fitness value of chromosomes.

The parents are mixed and recombined to produce offsprings for the next generation. From this process of evolution, it is expected that the best chromosomes will create more offsprings, and thus having a higher probability of surviving in the subsequent generation. This emulates the survival-of-the-fittest mechanism in nature. The evolution cycle is repeated until a desired termination criterion is reached. The criterion used could be the number of evolution cycles, the amount of variation of individuals between different generations, or a predefined fitness value. In order to achieve a GA evolution cycle, two fundamental operators, crossover and mutation, are required.

The procedure described above can be applied in many different ways to solve a wide range of problems.

However, in the design of a GA to solve a specific problem, there are always two major decisions: specifying the mapping between the chromosome structure and candidate solutions (representation problem) and defining a concrete fitness function.

2.4.1. Chromosome Representation

“Bit-string encoding is the most classical approach used by GA researchers because of its simplicity and traceability” [15]. A slight modification is the use of Gray code in the binary coding; “in practice, Gray-coded representation if often more successful for multi-variable function optimization applications” [17].

Real-valued chromosomes were introduced to deal with real variable problems. “Many works indicate that the floating point representation would be faster in computation” [15].

2.4.2. The Fitness Function

“The Fitness Function is at the heart of an evolutionary computing application” [18]. It determines which solutions within a population are better at solving the particular problem[18], being an important link between GA and the system. The Fitness Function takes a chromosome as an input and outputs a number which represents the measure of the chromosome performance.

An ideal fitness function correlates closely with the algorithm goal, and besides may be computed quickly. Speed of execution is very important, thus, a typical GA must be iterated many, many times, in order to produce a usable result for a non-trivial problem.

Definition of the *Fitness Function* is not straightforward in many cases, and it is often performed iteratively if the solutions produced by GA are not what it is desired.

2.4.3. Fundamental Operators

The crossover operator is shown in Figure 2.9. The portion of the two chromosomes beyond the crossover point to the right is exchanged to form the offspring. An operation rate (p_c) with a typical value between 0.6 - 1.0 is normally used as the probability of crossover.

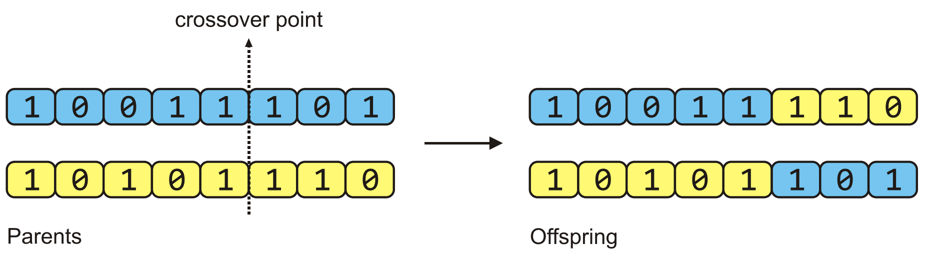

Figure 2.9: The crossover operator

Although one-point crossover was inspired by biological processes, it has one major drawback in the certain combination of *schema* (encoded form of the chromosome): sets of strings that have one or more features in common cannot be combined in some situations. “A multipoint crossover can be introduced to overcome this problem” [15]. As a result, the generating offspring performance is much improved.

The mutation operator, on the other hand, is applied to each offspring individually after the crossover exercise. Figure 2.10 shows the mutation process. It commutes each bit randomly with a probability p_m with a typical value of less than 0.1 [15].

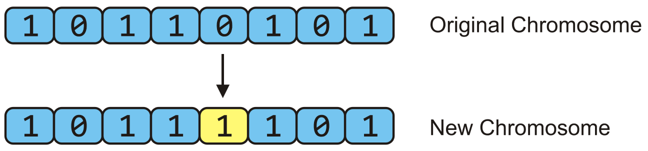

Figure 2.10: The mutation operator

The choice value of p_m and p_c can be a complex, nonlinear operation problem; furthermore, their settings are critically dependent upon the nature of the fitness function [15].

2.4.4. Genetic Algorithms to Solve Problems

Arguably the most obvious application of GA is the multi-variable function optimization. By searching for some optimal value, many problems can be formulated; where the value is a complicated function of its input parameters. In some cases, the interest is on variable settings that lead to the greatest value of the function. In other cases, the exact optimum is not required, just a near optimum, or inclusive a value that represents an improvement over the previously best known value [17].

2.4.5. Differential Evolution

Differential Evolution (DE), like GA, owned to the family of Evolutionary Computation. It is an optimization technique that uses an exceptionally simple evolution strategy, being significantly faster and robust at numerical optimization. It is more likely to find a function’s true global optimum.

“DE uses real coding of floating point numbers” [19], and the population is represented by *NP* individuals, where an individual is formed by a vector of *D* real variables, where D is the number of problem’s variables.

DE uses both, crossover and mutation operators. However, both operations are redefined in its context. DE creates a vector x_c', a mutated form of any individual x_c (an individual randomly picked from the initial population *NP*), using the vector difference between two other randomly picked individuals x_a and x_b such that: $x_c' = x_c + F(x_a - x_b)$, where *F* is an user-supplied scaling factor. The optimal value of *F* for most functions lies in the range of 0.4 to 1.0 [20]. This operation is known as *mutating with vector differentials*.

After that, the crossover is applied between any individual member of the population x_i and the mutated vector x_c', by swapping the vector elements in the corresponding locations. Like GA, this is also done probabilistically, and the decision of performing (or not performing) crossover is determined by a crossover constant *CR* in the range 0 to 1.

The new vector x_t produced is known as the *trial vector*. "Thus, the trial vector is the child of two parents, a noisy random vector x_c' and the target vector $\mathrm{x_i}$, against which it must compete" [19]. *CR* represents the probability that the child vector inherits the parameter values from the noisy random vector x_c'. When $CR = 1$, for example, every trial vector parameter comes from x_c'. If $CR = 0$, all but one trial vector parameter comes from the target vector x_t. To ensure that x_t differs from x_i by at least one parameter, the final trial vector parameter always comes from the noisy random vector, even when $CR = 0$, so that it does not become an exact replica of the original parent vector. Thus, the trial vector is allowed to pass on the next generation if and only if, its fitness is higher than that of its parent vector x_i, otherwise the parent vector yields to the next generation. Figure 2.11 shows the process of DE.

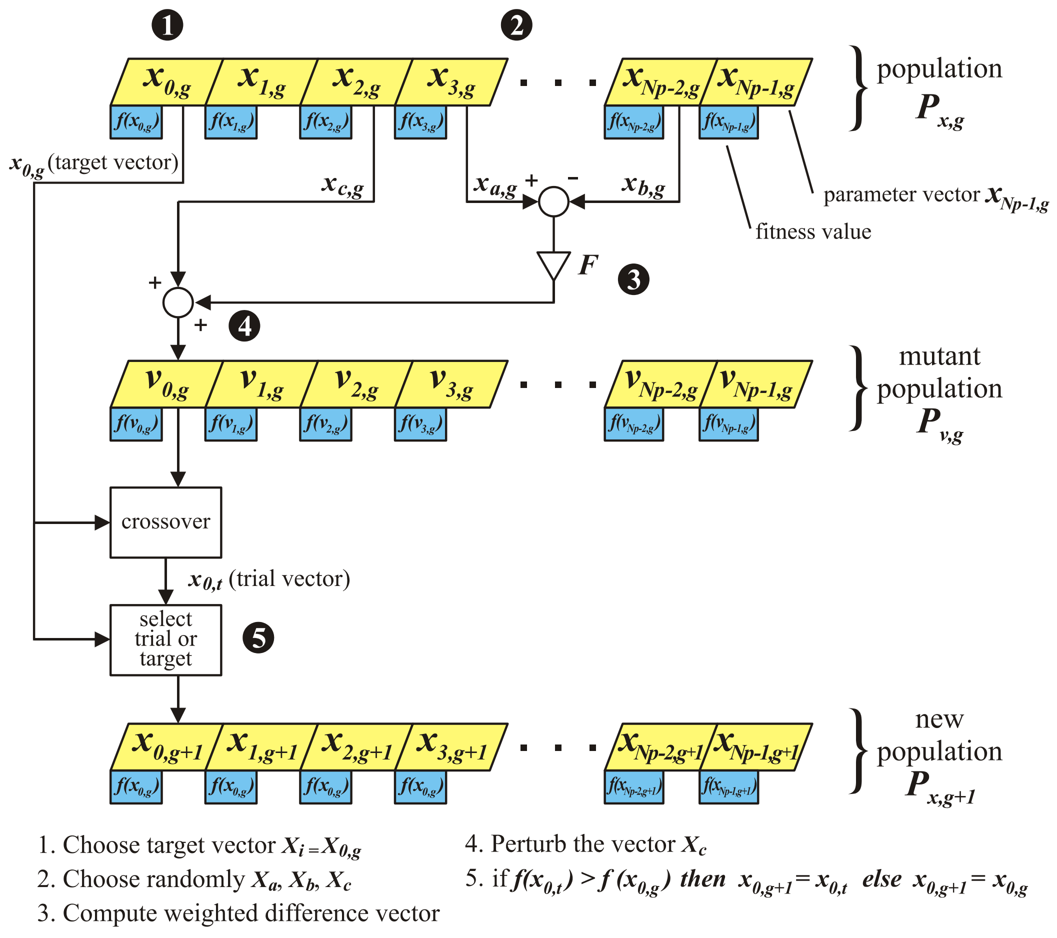
1
2
x0,g x1,g x2,g x3,g . . . xNp-2,g xNp-1,g
population Px,g
parameter vector xNp-1,g
fitness value
x0,g (target vector)
xc,g
xa,g
xb,g
F
3
4
v0,g v1,g v2,g v3,g . . . vNp-2,g vNp-1,g
mutant population Pv,g
crossover
x0,t (trial vector)
select trial or target
5
x0,g+1 x1,g+1 x2,g+1 x3,g+1 . . . xNp-2,g+1 xNp-1,g+1
new population Px,g+1
1. Choose target vector Xi = X0,g
2. Choose randomly Xa, Xb, Xc
3. Compute weighted difference vector
4. Perturb the vector Xc
5. if f(x0,t) > f (x0,g) then x0,g+1 = x0,t else x0,g+1 = x0,g

Figure 2.11: Differential Evolution Process [21]

Among all, just three factors control evolution under DE: the population size *NP*, the weight *F* applied to the random differential, and the crossover constant *CR*.

2.4.6.
Different Strategies of DE

Depending on the type of problem, different strategies can be adopted in the DE algorithm. "The strategies can vary based on the vector to be perturbed, number of difference vectors considered for perturbation, and finally the type of crossover used" [19]. The following are the 10 different working strategies proposed by Price and Storn [21].

1. DE/best/1/exp

2. DE/rand/1/exp
3. DE/rand-to-best/1/exp
4. DE/best/2/exp
5. DE/rand/2/exp
6. DE/best/1/bin
7. DE/rand/1/bin
8. DE/rand-to-best/1/bin
9. DE/best/2/bin
10. DE/rand/2/bin

The convention used above is DE*/x/y/z*. DE means Differential Evolution, *x* denotes a string representing the vector to be perturbed, *y* is the number of difference vectors used for perturbation of *x*, and *z* denotes the type of crossover being used (exp: exponential, bin: binomial).

For perturbation with a single vector difference, out of the three distinct randomly chosen vectors, the weighted vector differential of any two vectors is added to the third one. In the same way for perturbation with two vector differences, five distinct vectors, other than the target vector, are chosen randomly from the current population. Out of these, the weighted vector difference of each pair of any four vectors is added to the fifth one for perturbation.

In exponential crossover, the crossover is performed on the *D* variables in one loop until it is within the *CR* bound. In binomial crossover, the crossover is performed on each of the *D* variables whenever a randomly picked number between 0 and 1 is within the *CR* value. So, for high values of *CR*, the exponential and binomial crossovers yield similar results. In the binomial case, the last variable always comes from a random noisy vector to ensure that is different from the target vector, and hence the above procedure is applied up to $D - 1$ variables.

“The strategy to be adopted for each problem is to be determined separately by trial and error” [19]. The best strategy for a given problem may not work well when applied to a different problem.

In the next chapter, the presented analytical background is applied to the SLAM problem.

3.
SLAM Solutions

3.1.
Gaussian Filter SLAM Solutions

“Historically, Gaussian Filters constitute the earliest tractable implementations of the Bayes Filter for continuous spaces”. It could say that they are also by far the most popular family of techniques to date – despite a number of limitations [1].

Gaussian assumes the idea that beliefs are represented by multivariate normal distributions:

$$p(x) = \det(2\pi\Sigma)^{-\frac{1}{2}} \exp\{-\tfrac{1}{2}(x-\lambda)^T \Sigma^{-1}(x-\lambda)\} \tag{3.1}$$

The distribution over the variable *x* is characterized by two sets of parameters: the mean *λ* and the covariance Σ. The mean has the same dimensionality of the state *x*. The covariance is a symmetric quadratic matrix, positive semi-definite, and its dimension is the dimensionality of the state *x* squared. Hence, the dimension of the covariance matrix depends quadratically on the dimension of the state vector *x*.

3.1.1.
Kalman Filter SLAM

“Probably the best studied technique for implementing Bayes filter is the Kalman Filter” [1]. “The Kalman Filter (KF) was developed by R.E. Kalman, whose prominent paper on the subject was published in 1960” [4].

The KF is an algorithm which processes data and estimates variable values. In SLAM context, the variable values to be estimated consist of the robot position and landmark locations. The data to be processed may be actuator inputs, range sensor readings, motion sensors and digital cameras of the mobile robot. Thus, the KF utilizes all available data to simultaneously estimate robot position and generate a landmark map. In [22] it is explained that KF is a set of mathematical equations that provides an efficient computational (recursive) mean to estimate the estate of a process, in a way that minimizes the mean of the squared error.

"Under certain conditions, the estimates made by a KF are very good; in fact, they are in a sense "optimal" " [4].

The Kalman Filter represents probability distributions at time t by the mean λ_t and the covariance Σ_t. Thus, posterior distributions are Gaussian if the following three properties are fulfilled, in addition to the Markov assumptions of the Bayes filter[1].

1. the next state probability (or motion model), $p(x_t|u_t,x_{t-1})$ in eq. (2.3), must be a linear function in its arguments with added Gaussian noise [1]. This is expressed by the following equation:

$$x_t = A_t x_{t-1} + B_t u_t + \varepsilon_t \tag{3.2}$$

where x_t and x_{t-1} are *state* vectors, and u_t is the control vector at time t, given by

$$x_t = \begin{pmatrix} x_{1,t} \\ x_{2,t} \\ \vdots \\ x_{m,t} \end{pmatrix} \quad \text{and} \quad u_t = \begin{pmatrix} u_{1,t} \\ u_{2,t} \\ \vdots \\ u_{q,t} \end{pmatrix} \tag{3.3}$$

A_t is a square matrix of size m x m, where m is the dimension of the state vector x_t. B_t is of size m x q, where q is the dimension of the control vector u_t. The random variable, ε_t in eq.(3.2), is a Gaussian random vector of size m, that models the uncertainty in the state transition. Its mean is zero and its covariance is denoted by P_t. A state transition of the form in eq.(3.2) is called a linear Gaussian, "to reflect the fact that it is linear in its arguments with additive Gaussian noise" [1].

The probability $p(x_t|u_t,x_{t-1})$ is obtained by plugging eq.(3.2) into the multivariate normal distribution, eq. (3.1). The mean of the posterior state is given by $A_t x_{t-1} + B_t u_t$ and the covariance by P_t, thus

$$p(x_t \mid u_t, x_{t-1}) = \det(2\pi P_t)^{-\frac{1}{2}} \exp\{-\tfrac{1}{2}(x_t - A_t x_{t-1} - B_t u_t)^T P_t^{-1}(x_t - A_t x_{t-1} - B_t u_t)\} \tag{3.4}$$

2. the measurement probability (or perception model), $p(z_t|x_t)$ in eq. (2.3), must also be linear in its arguments, with added Gaussian noise [1]:

$$z_t = H_t x_t + \delta_t \tag{3.5}$$

H_t is a matrix of size k x m, where k is the dimension of the measurement vector z_t. The vector δ_t describes the measurement noise with a multivariate Gaussian with zero mean and covariance Q_t. In this way the measurement probability is given by the following multivariate normal distribution [1]:

$$p(z_t \mid x_t) = \det(2\pi Q_t)^{-\frac{1}{2}} \exp\{-\tfrac{1}{2}(z_t - H_t x_t)^T Q_t^{-1}(z_t - H_t x_t)\} \tag{3.6}$$

3. finally, the initial probability $p(x_0)$ must be normally distributed and, denoted by the mean λ_0 and the covariance Σ_0 [1]:

$$p(x_0) = \det(2\pi\Sigma_0)^{-\frac{1}{2}} \exp\{-\tfrac{1}{2}(x_0 - \lambda_0)^T \Sigma_0^{-1}(x_0 - \lambda_0)\} \tag{3.7}$$

These three assumptions are sufficient to ensure that the posterior $p(x_t)$ is always a Gaussian, for any point in time [1].

As described above, the Kalman Filter represents probability distributions at time t by the mean λ_t and the covariance Σ_t. The equations of the Kalman Filter algorithm are depicted in Table 3.1. The inputs of the Kalman Filter is the distribution at time t–1, represented by λ_{t-1} and Σ_{t-1}, the control u_t, and the measurement z_t. The output is the distribution at time t, represented by λ_t and Σ_t.

Table 3.1: The Kalman Filter Algorithm [1].

```
Kalman_filter_algorithm ( $\lambda_{t-1}, \Sigma_{t-1}, u_t, z_t$ )
1:    $\bar{\lambda}_t = A_t \lambda_{t-1} + B_t u_t$                                        (3.8)
2:    $\bar{\Sigma}_t = A_t \Sigma_{t-1} A_t^T + P_t$                                      (3.9)
3:    $K_t = \bar{\Sigma}_t H_t^T \left( H_t \bar{\Sigma}_t H_t^T + Q_t \right)^{-1}$      (3.10)
4:    $\lambda_t = \bar{\lambda}_t + K_t \left[ z_t - H_t \bar{\lambda}_t \right]$        (3.11)
5:    $\Sigma_t = \bar{\Sigma}_t - K_t H_t \bar{\Sigma}_t$                                 (3.12)
6:    return $\lambda_t, \Sigma_t$
```

Let’s describe some of the parameters in above equations.

- $\bar{\Sigma}_t$, $\bar{\lambda}_t$ are the predicted covariance and median, representing $\int p(x_t \mid u_t, x_{t-1}) p(x_{t-1} \mid z^{t-1}, u^{t-1}) dx_{t-1}$ in eq. (2.3), obtained by incorporating the control u_t one step later, but before incorporating the measurement z_t.

- A_t is called the state transition matrix; it describes how one thinks the state will change due to factors not associated with control input. One very nice convention in SLAM is that landmarks will remain stationary. Except for the first row which correspond to changes in robot position, A_t will therefore appear as a diagonal matrix with each diagonal entry containing identity matrices (otherwise A_t would change location of landmarks, which are known to be stationary) [4]. If the robot can have a non-zero velocity at time step t, then the state may change even with no actuator input, and the first column of A_t can account for this. To simplify the analysis, let’s assume that the robot comes to a halt after each time step. In this case, the actuator input fully specifies the most likely new location of the robot. This means that A_t is just the identity matrix, which could be disregarded.

- B_t is a matrix that translates control input into a predicted change in state. Its values will depend on the representation of the control input. It will vary depending on the physical construction of the robot. Because the landmarks will remain stationary the only interesting entries of B_t will be in the first row. Thus, the idea of eq. (3.8) is that the best guess for the new state will be described exactly by the old robot position and how one believes the actuators will change this position.

- P_t is the covariance of the process noise. It accounts for how moving will change the confidence on each individual pair of landmarks as well as robot-landmarks pairs. The entries of P_t will depend on the distance landmarks are away from the robot and other known particularities of the environment and/or state [4].

- Q_t is the covariance matrix for the range sensor noise, it is used to keep track of one's confidence in the range sensor readings.

- H_t transforms one's previous state estimate into a representation used by the sensors. In other words, if the sensors had perceived the world state exactly as predicted by $\overline{\lambda}_t$, they would have returned this information in the form $H_t\overline{\lambda}_t$. Note that the purpose of H_t is very similar to that of B_t.

- Finally, K_t is called the Kalman *gain*. It specifies the degree to which the measurement is incorporated into the new state estimate. The magnitudes of the values in K_t depend on the predicted covariance $\overline{\Sigma}_t$, relative to the combined values of the predicted covariance and sensor uncertainty Q_t.

The Kalman filter is a technique for filtering and prediction in linear systems. However, in most real world SLAM situations there will be some non-linear aspect one might wish to account for. "For example, a robot that moves with constant translational and rotational velocity typically moves on a circular trajectory, which cannot be described by linear next estate transitions" [1]. Thus the plain Kalman Filters, as discussed above is inapplicable to all but the most trivial robotics problems.

3.1.2. Extended Kalman Filter SLAM

The *Extended Kalman Filter* (EKF) overcomes the linearity assumption [1]. Here, in EKF, the assumption is that the next state probability $p(x_t|u_t,x_{t-1})$, and the measurement probability $p(z_t|x_t)$, are ruled by nonlinear functions *f* and *h*, respectively.

$$x_t = f(u_t, x_{t-1}) + \varepsilon \tag{3.13}$$

$$z_t = h(x_t) + \delta \tag{3.14}$$

This model is a generalization of the linear Gaussian model underlying Kalman filters, as stated in eq. (3.2) and eq. (3.5). The function *f* replaces the matrices A_t and B_t in eq.(3.2) and *h* replaces H_t in eq. (3.5) [1]. However, the distribution is not longer a Gaussian when it is used nonlinear functions, *f* and *h*. In this way, the distribution update does not possess a closed-form solution. Therefore, the EKF calculates an approximation of the true distribution. “Thus, the EKF inherits from the Kalman filter the basic belief representation, but it differs in that this belief is only approximate, not exact as it was the case in linear Kalman Filters” [1].

To manage this approximation EKF utilizes a (first order) *Taylor expansion*. The Taylor expansion constructs a linear approximation to a function *f* from its value and slope. The slope is given by the following partial derivative [1]:

$$f'(u_t, x_{t-1}) := \frac{\partial f(u_t, x_{t-1})}{\partial x_{t-1}} \tag{3.15}$$

Both the value of *f* and its slope depend on the argument of *f*.. Thus *f* is approximated by its value at λ_{t-1} (and at u_t), and the linear extrapolation is achieved by a term proportional to the gradient of *f* at λ_{t-1} and u_t [1]:

$$f(u_t, x_{t-1}) \approx f(u_t, \lambda_{t-1}) + \underbrace{f'(u_t, \lambda_{t-1})}_{=:\,F_t}(x_{t-1} - \lambda_{t-1})$$

$$f(u_t, x_{t-1}) = f(u_t, \lambda_{t-1}) + F_t(x_{t-1} - \lambda_{t-1}) \tag{3.16}$$

Written in form of Gaussians, the next state probability is approximated by:

$$\begin{aligned} &p(x_t \mid u_t, x_{t-1}) \\ &\approx \det(2\pi P_t)^{-\frac{1}{2}} \exp\{-\tfrac{1}{2}[x_t - f(u_t, \lambda_{t-1}) - F_t(x_{t-1} - \lambda_{t-1})]^T \\ &\quad P_t^{-1}[x_t - f(u_t, \lambda_{t-1}) - F_t(x_{t-1} - \lambda_{t-1})]\} \end{aligned} \tag{3.17}$$

The matrix F_t is often called the *Jacobian*. The value of the Jacobian depends on u_t and λ_{t-1}, thus it differs for different time points.

The same linearization is used for the measurement function *h*. Where, the Taylor expansion is developed around $\overline{\lambda}_t$, the state regarded most likely by the robot at the time when it linearizes *h* [1]:

$$h(x_t) \approx h(\overline{\lambda}_t) + \underbrace{h'(\overline{\lambda}_t)}_{=:\,H_t}(x_t - \overline{\lambda}_t)$$

$$h(x_t) = h(\overline{\lambda}_t) + H_t(x_t - \overline{\lambda}_t) \tag{3.18}$$

where $h'(x_t) = \frac{\partial h(x_t)}{\partial x_t}$. Written in form of Gaussian, one gets:

$$p(z_t \mid x_t)$$

$$\approx \det(2\pi Q_t)^{-\frac{1}{2}} \exp\{-\tfrac{1}{2}[z_t - h(\bar{\lambda}_t) - H_t(x_t - \bar{\lambda}_t)]^T$$

$$Q_t^{-1}[z_t - h(\bar{\lambda}_t) - H_t(x_t - \bar{\lambda}_t)]\} \qquad (3.19)$$

Table 3.2 depicts the Extended Kalman Filter algorithm.

Table 3.2: The EKF Algorithm [1]

EKF_algorithm ($\lambda_{t-1}, \Sigma_{t-1}, u_t, z_t$)		
1:	$\bar{\lambda}_t = f(u_t, \lambda_{t-1})$	(3.20)
2:	$\bar{\Sigma}_t = F_t \Sigma_{t-1} F_t^T + P_t$	(3.21)
3:	$K_t = \bar{\Sigma}_t H_t^T \left(H_t \bar{\Sigma}_t H_t^T + Q_t\right)^{-1}$	(3.22)
4:	$\lambda_t = \bar{\lambda}_t + K_t\left[z_t - h(\bar{\lambda}_t)\right]$	(3.23)
5:	$\Sigma_t = \bar{\Sigma}_t - K_t H_t \bar{\Sigma}_t$	(3.24)
6:	return λ_t, Σ_t	

In some ways, the EKF is similar to the (linear) Kalman Filter. The difference is that the linear equations in Kalman Filters are replaced by their non-linear generalization in EKFs.

A detailed implementation of the EKF algorithm is shown in Section 4.1.

3.2. Particle Filter SLAM Solutions

3.2.1. Particle Filter Overview

Particle Filters (PF) are alternatives to Gaussian techniques. They do not rely on a fixed functional form of the posterior distribution, such as Gaussians.

Instead, they approximate these posterior distributions by a finite number of values, each harshly corresponding to a region in state space.

"The key idea of the PF is that any posterior distribution p(x_t) can be represented by a set of random state samples drawn from this posterior" [1]. Figure 3.1 shows this idea for a Gaussian; instead of representing the distribution by a parametric form (the mean and covariance that defines the exponential of a normal distribution), PF represents it by a set of samples drawn from this Gaussian. As the number of samples goes to infinity, PF tends to converge uniformly to the correct posterior distribution. Thus this method can represent any arbitrary shape of distribution, making it good for non-Gaussian, multimodal distributions.

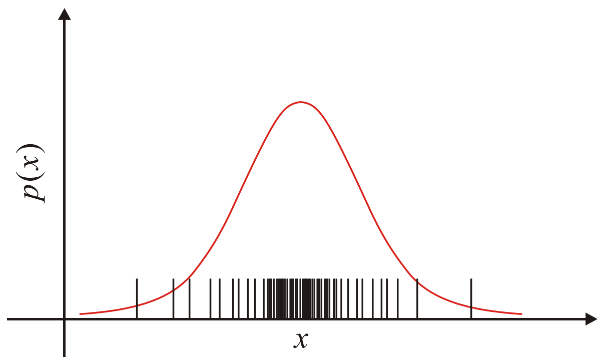

Figure 3.1: Representation of a Gaussian by a set of particles

In PF, the samples are called *particles*, thus the posterior $p(x_t)$ is represented by N weighted particles:

$$\Phi_t := \{\left\langle x_t^i, w_t^i \right\rangle / i = 1 \ldots N\} \tag{3.25}$$

The correspondence between the Bayes Filters and the approximation made by particles is given by

$$p(x_t) \approx \Phi_t \tag{3.26}$$

In this way, to compute $p(x_t)$ it is necessary to find Φ_t at each time, that is to find all values of x_t^i and w_t^i. As a Bayes Filter algorithm, the PF algorithm constructs the distribution $p(x_t)$ recursively from the distribution $p(x_{t-1})$ one time step earlier. Thus, PF constructs the particle set Φ_t recursively from the set Φ_{t-1}.

In Probabilistic Robotics, the process to generate samples x_t^i is achieved using the prior Φ_{t-1} and the most recent control u_t. The desired weight w_t^i of each particle is given using the most recent measurement z_t. Table 3.3 shows the most basic variant of the PF algorithm[1].

Table 3.3: Particle Filter Algorithm [1]

```
        Particle Filter_algorithm ($\Phi_{t-1}, u_t, z_t$)
1:      $\overline{\Phi}_t = \Phi_t = 0$
2:      for $i = 1$ to $N$ do
3:          sample $x_t^i \sim p(x_t \mid u_t, x_{t-1}^i)$
4:          $w_t^i = p(z_t \mid x_t^i)$
5:          $\overline{\Phi}_t = \overline{\Phi}_t + \langle x_t^i, w_t^i \rangle$
6:      end for
7:      for $i = 1$ to $N$ do
8:          draw $i$ with probability $\propto w_t^i$
9:          add $x_t^i$ to $\Phi_t$
10:     end for
11:     return $\Phi_t$
```

The algorithm first samples by processing each particle x_{t-1}^i in the input particle set Φ_{t-1} as follows:

1. Line 3 of table Table 3.3 generates a estimate x_t^i for time t based on the particle x_{t-1}^i and the control u_t. This step involves sampling for the next state transition $p(x|u_t, x_{t-1})$. Thus the set of particles resulting from iterating line 3 N times represents the distribution $\int p(x_t \mid u_t, x_{t-1}) p(x_{t-1} \mid z^{t-1}, u^{t-1}) dx_{t-1}$ in eq. (2.3).

2. Line 4 computes for each particle x_t^i the corresponding weight (*importance factor*) w_t^i using the measurement z_t. Thus, each w_t^i is the probability of the measurement z_t under the particle x_t^i, in the way of $w_t^i = p(z_t \mid x_t^i)$.

3. Finally lines 7 to 11 implement as the so-called *resampling* or *importance resampling*. This lines draw with replacement N particles from the temporary set $\overline{\Phi}_t$. The probability of drawing each particle is given by its importance factor (weight). The resulting set, Φ_t, is a set of N particles distributed according to the desired $p(x_t)$.

Figure 3.2 shows the Particle Filter algorithm idea. The desired $p(x_t)$ is shown as a red line and the samples x_t^i as blue lines.

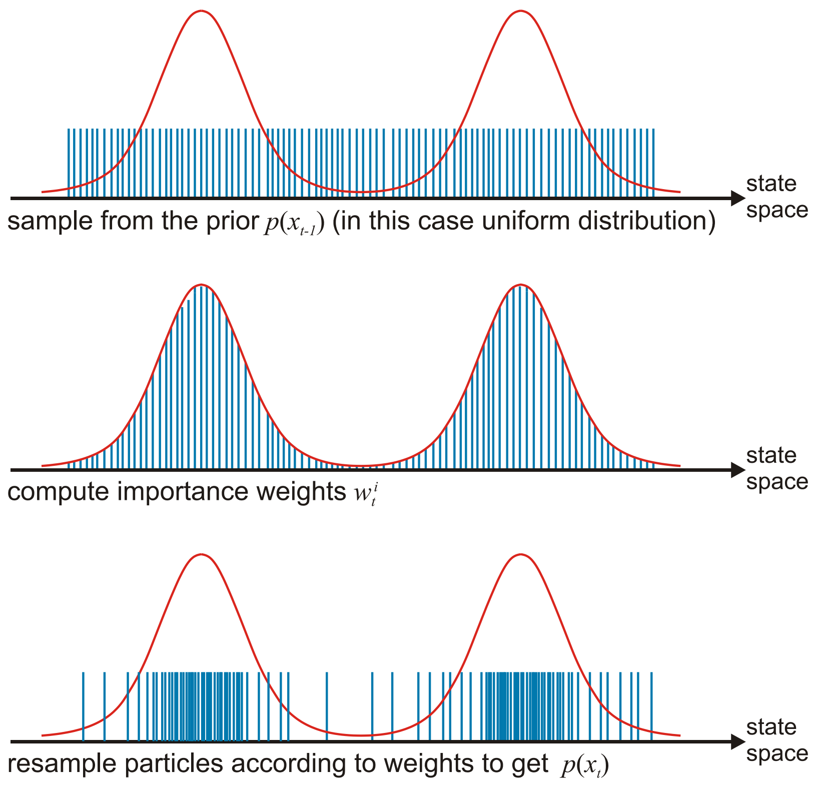
state space
sample from the prior $p(x_{t-1})$ (in this case uniform distribution)
state space
compute importance weights w_t^i
state space
resample particles according to weights to get $p(x_t)$

Figure 3.2: Particle Filter idea.

The PF computes the Bayes filter stated in eq. (2.3) from right to left, as shown in the following equation:

$$\underbrace{\overbrace{p(x_t \mid z^t, u^t)}^{\text{desired distribution } (\Phi_t)}}_{\text{resampling to obtain the desired distribution } p(x_t)} = \underbrace{\eta\, \overbrace{p(z_t \mid x_t)}^{\text{perception model}}}_{\text{computing the weights } w_t^i \text{ using the perception model}} \underbrace{\int \overbrace{p(x_t \mid u_t, x_{t-1})}^{\text{motion model}} \overbrace{p(x_{t-1} \mid z^{t-1}, u^{t-1})}^{\text{prior distribution from the last step } (\Phi_{t-1})} dx_{t-1}}_{\text{generating samples } x_t^i \text{ from the prior distribution } p(x_{t-1}) \text{ using the motion model}} \tag{3.27}$$

3.2.2. Fast SLAM

The Fast SLAM was developed by Montemerlo, Thrun, Koller and Wegbreit [23]. Fast SLAM exploits the condition independence properties of the SLAM model to break up the problem of localizing and mapping into many separate problems.

As it was seen in Section 3.1, the dimension of the covariance matrix Σ_t is the dimensionality of the state x squared. Thus, the number of elements in the covariance matrix depends quadratically on the number of elements in the state vector x. This is because the robot's position uncertainty correlates landmark locations, as Figure 3.3 shows. Supposing an observation (L_1, L_2) made by the robot, then, through another observation for L_1, one ends up to another position for L_2. Now, if the assumption on L_1 is again different, the conclusion on L_2 also is. This is the consequence of not knowing the robot's position precisely. As a result, this lack of knowledge on the robot's position correlates the location of the landmarks.

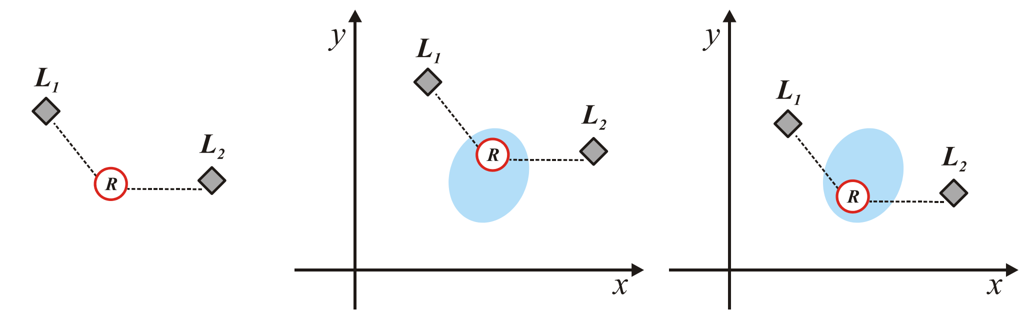

L_1
L_2
R
y
x
Assumed measurement
A different assumption on the position of landmark L_1 leads to a different place of landmark L_2, since the robot´s pose is unknown.

Figure 3.3: Landmark correlation

In this way, if one could know exactly the robot position, there should be no predictable relationship between the landmark observations. An important point in SLAM is that the exact robot pose is not known, but insight of conditional independence of landmarks, given the pose, is enough to motivate FastSLAM, which manages each landmark separately [4] - decoupling into *n* (number of landmarks) independent estimation problems, one for each landmark. Thus, Fast SLAM decomposes the SLAM problem into a robot position problem, and a set of landmark location estimation problems that are conditioned on the robot position estimated.

Mathematically, decorrelation of the landmark locations leads to a factored representation as following:

$$p(R^t, m \mid z^t, u^t) = p(R^t, L_1, \ldots, L_n \mid z^t, u^t)$$
$$p(R^t, L_1, \ldots, L_n \mid z^t, u^t) = p(R^t \mid z^t, u^t) \prod_n p(L_n \mid R^t, z^t, u^t) \tag{3.28}$$

This factorization is exact and always applicable to the SLAM problem [23]. It decomposes the posterior over robot paths and maps into *n*+1 recursive estimators: one estimator over robot pats $p(R^t | z^t, u^t)$ and *n* separated landmark pose estimators $p(L_n | z^t, u^t, R^t)$ conditioned on each hypothetical path.

FastSLAM keeps track of many possible paths simultaneously (superscript *t* of the robot pose R^t), as opposed to the traditional Kalman Filter, “which does not even keep track of a single path, but rather updates a single robot pose” [4]. Thus, Fast SLAM records paths and when the algorithm terminates there will be a record of where the robot has been.

Fast SLAM uses a modified PF for implementing the path estimator, $p(R^t|z^t,u^t)$, and the landmark pose estimators $p(L_n\,|\,z^t,u^t,R^t)$ are realized by Kalman Filters, using separate filters for different landmarks. Because landmark estimation is conditioned on path estimation, each particle in PF has its own local landmark estimations. At time *t*, the *i*-th particle contains

$$s_t^i := \{\underset{\substack{\downarrow\\ \text{weight}}}{w_t^i},\ \underset{\substack{\downarrow\\ \text{robot's}\\ \text{path}}}{R^{i,t}},\underbrace{\lambda_{1,t}^i,\Sigma_{1,t}^i}_{\substack{\text{landmark}\\ 1}},\ \underbrace{\lambda_{2,t}^i,\Sigma_{2,t}^i}_{\substack{\text{landmark}\\ 2}},\ ...,\ \underbrace{\lambda_{n,t}^i,\Sigma_{n,t}^i}_{\substack{\text{landmark}\\ n}}\} \tag{3.29}$$

where $\lambda_{n,t}^i$ and $\Sigma_{n,t}^i$, are the Gaussian parameters (mean and covariance respectively) related with the landmark position $L_{n,t}^i$. To update the landmark-map for a given path $R^{i,t}$ each observed landmark is processed individually as an EKF measurement update from a known robot pose (unobserved landmarks are unchanged).

Bearing the distribution at time *t*–1 as a set of particles, one gets:

$$\Phi_{t-1} := \{\left\langle s_{t-1}^i \right\rangle / \, i = 1...N\} \tag{3.30}$$

The first version of Fast SLAM algorithm [1] follows the following steps:

1. for each particle extend its path, $R^{i,t-1}$, to generate a new pose using the control u_t and the motion model $p(R_t|u_t,R_{t-1})$. Mathematically this means that the distribution at time *t*–1, $p(R^{t-1}|z^{t-1},u^{t-1})$ becomes $p(R^t|z^{t-1},u^t)$. A set of temporal particles is obtained.

2. update the estimation of landmarks, through the EKF

$$p(L_n\,|\,R^t,z^t,u^t) = \eta\, p(z_t\,|\,L_n,R_t)\,p(L_n\,|\,R^{t-1},z^{t-1},u^{t-1}) \tag{3.31}$$

and, using the new poses generated in the step 1 and the measurement z_t, compute the new set of $\lambda_{n,t}^{i}$ and $\Sigma_{n,t}^{i}$. This set of means and covariances are added to the temporal particles set.

3. assign the weight for each particle. This is computed using the result of step 1, $p(R^t | z^{t-1}, u^t)$, where the measurement z_t was not included, and using the distribution $p(R^t | z^t, u^t)$, where z_t is included

$$w_t^i = \frac{p(R^{t,i} \mid z^t, u^t)}{p(R^{t,i} \mid z^{t-1}, u^t)} \tag{3.32}$$

after some considerations and probabilistic transformations, the above equation is given by:

$$w_t^i \approx \eta \det(2\pi U_t^i)^{-\frac{1}{2}} \exp\{-\tfrac{1}{2}(z_t - \hat{z}_t^i)^T U_t^{i\,-1}(z_t - \hat{z}_t^i)\} \tag{3.33}$$

$$U_t^i = H_t^{i\,T} \Sigma_{t-1,n}^i H_t^i + Q \tag{3.34}$$

where z_t is the sensor observation. Note that $\hat{z}_t^i$ is the predicted observation computed using the landmark position estimated in step 2 and the robot poses generated in step 1. H_t^i is the *Jacobian* of the perception model. This set of importance factors (weights) are added to the temporal particles set.

4. finally, resample. Each particle, in the temporal particle set, is drawn (with replacement) with a probability proportional to its importance factor.

A detailed implementation of the Fast Slam 1.0 algorithm is shown in Section 4.2.

3.2.3. DP-SLAM

The Fast SLAM is a good solution to the SLAM problem when there are thousands of landmarks that can be tracked accurately. However tracking landmarks is actually very difficult, particularly in environments with monochromatic areas or repeating patterns.

If the robot is using a LRF, the map generated by the laser has no landmarks; is rather an occupancy grid, as described in Section 2.2.2. "The robot cannot use the range finder to relocate individual points in the grid. However with enough data, the robot might not need to worry about reacquiring landmarks in the first place" [4]. For example, if there was a contoured object in the environment, the robot might align entire occupancy maps by matching up the contour of that object. Distributed Particle SLAM (DP-SLAM) [6] attacks SLAM from this occupancy grid approach, while simultaneously utilizing the conditional independence insight discussed in Fast SLAM.

"One of the steps in the Fast SLAM algorithm was to generate a new pose prediction and a corresponding map prediction" [4]. Thus, the new map prediction was based on the previous pose and the control input u_t. It cannot predict how landmarks will move with respect to the robot anymore because landmarks are not dealt with. However it is possible to make a prediction as to how the occupancy grid will change. Figure 3.4 shows an example of occupancy grid prediction based on a movement of one cell to the right.

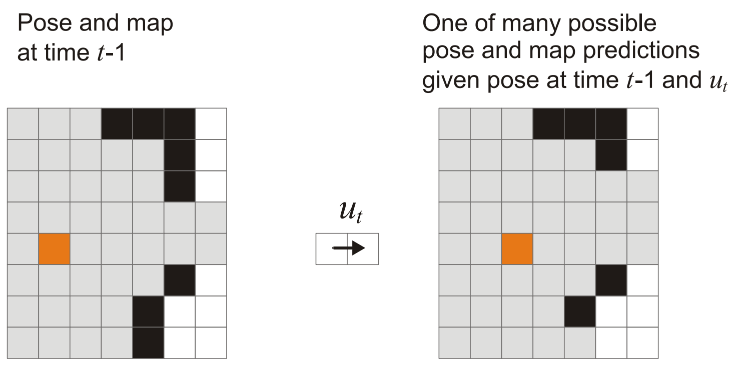
Pose and map at time t-1
One of many possible pose and map predictions given pose at time t-1 and u_t
u_t

Figure 3.4: Occupancy grid prediction based on a movement of one cell to the right.

Similarly to Fast SLAM, DP-SLAM uses PF, generating new particles (poses) by applying probabilistically generated movement vectors to old poses. Thus DP-SLAM uses the same method to generate samples based on the motion model and the control vector u_t.

However, because the map representation is an occupancy grid, the perception model is quite different consequently, the way to assign weights, and the map update are quite different too.

3.2.3.1. DP-SLAM Map Representation

DP-SLAM uses an occupancy grid mapping representation, specifically stochastic maps, where each square has a sliding scale of various degrees of occupancy, as it was seen in Section 2.2.2.

“The idea of using probabilistic map representation is possibly as old as the topic of robotic mapping itself” [6]. Most of the earliest SLAM methods used probabilistic occupancy grids and were especially useful for sonar sensors susceptible to noisy and/or spurious measurements [6].

However, DP-SLAM concentrates on a model for Laser Range Finder. It has a method for representing uncertainty in the map, which takes into account the distance the laser travels through each grid square.

Earlier approaches, to estimating the total probability of the scan, would trace the scan through the map, giving a weight to the measurement error associated with each potential obstacle by the probability that the scan has actually reached the obstacle [6]. “In an occupancy grid with partial occupancy, each cell is a potential obstacle” [6].

Thus each grid square has the probability of stopping a laser ray, represented by [6]

$$P_c(x_i, \rho_i) = 1 - e^{\frac{-x_i}{\rho_i}} \tag{3.35}$$

where x_i is the distance that the laser ray travels through the square i and ρ_i is called the *opacity* of the square, as shown in Figure 3.5.

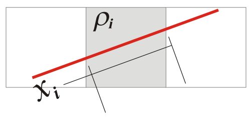

Figure 3.5: Square representation

The probability that an entire laser ray will have been stopped at some point along its trajectory is therefore the cumulative probability that the laser ray is interrupted by squares up to and including the last square, n, it reaches:

$$P(stopped = true) = P_c(\boldsymbol{x}, \boldsymbol{\rho}) = \sum_{i=1}^{n} P_c(x_i, \rho_i) \prod_{j=1}^{i-1} (1 - P_c(x_j, \rho_j)) \tag{3.36}$$

where x_i is the traveled distance (the laser ray travels through the square) and ρ_i the opacity of the square i, as shown in Figure 3.6.

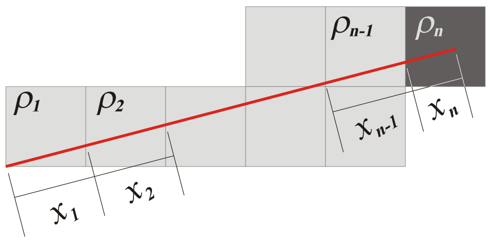

Figure 3.6: Interaction between the laser ray and the square representation

Inside the summation in eq. (3.36), the first term is the probability that the laser ray would be obstructed in the square n. The second term represents the probability that each previous square did not obstruct the laser.

Thus the probability that the laser ray will be interrupted a grid square j is $P(stop{=}j)$, which is computed as the probability that the laser has reached square $j{-}1$ and then stopped at j :

$$P(stop = j \mid \boldsymbol{x},\boldsymbol{\rho}) = P_c(x_j,\rho_j)(1 - P_c(\boldsymbol{x}_{1:j-1},\boldsymbol{\rho}_{1:j-1})) \tag{3.37}$$

where $\boldsymbol{x}_{1:j-1}$ and $\boldsymbol{\rho}_{1:j-1}$ have interpretations as fragments of the $\boldsymbol{x}$ and $\boldsymbol{\rho}$ vectors. Figure 3.7 illustrates this, where j=3, the vector $\boldsymbol{x} = \{x_1, x_2, \ldots x_n\}$, and $\boldsymbol{\rho} = \{\rho_1, \rho_2, \ldots \rho_n\}$.

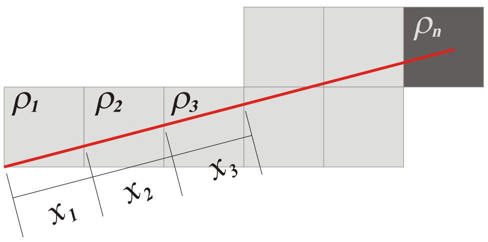

$$P(stop = 3 \mid \boldsymbol{x},\boldsymbol{\rho}) = P_c(x_3,\rho_3)(1 - P_c(\boldsymbol{x}_{1:2},\boldsymbol{\rho}_{1:2})) = (1 - e^{-\frac{x_3}{\rho_3}})[1 - P_c(x_1,\rho_1)][1 - P_c(x_2,\rho_2)]$$

Figure 3.7: Example of application of eq. (3.37) for a given square j=3.

DP-SLAM also defines a vector $\boldsymbol{\delta}$ as a vector of differences, such that δ_i is the distance between the laser distance measurement (the stopping point) and grid square i along the trace of the laser ray. Thus, the conditional probability of the measurement, given that the laser ray that was interrupted in square i, is $P_L(\delta_i|stop=i)$, for which is made the assumption of normally distributed measurement noise. Notice that δ_i terms are only defined if the laser measurement observes a specific stopping point, as shown in Figure 3.8; eq. (3.38) is used to compute this probability.

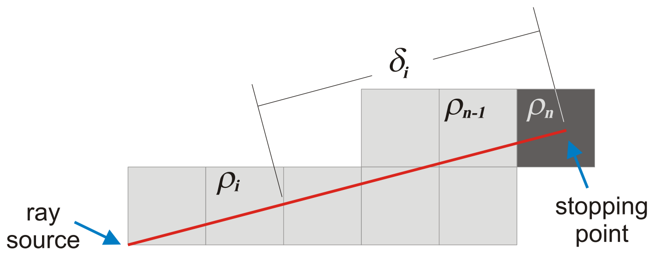

Figure 3.8: Distance between the square i and the stopping point of the laser ray

$$P_L(\delta_i \mid stop = i) = \frac{1}{\sigma\sqrt{2\pi}} e^{\frac{-\delta_i^2}{2\sigma^2}} \tag{3.38}$$

where σ is the standard deviation of the laser measurement.

Clearly in eq. (**3.38**), the lower distance δ_i (which means that square i is closer to the stopping point) the higher the probability. Basically, the idea of this vector of differences $\boldsymbol{\delta}$, is to create a probability distribution as shown in Figure 2.5.

Finally the probability of the laser measurement L, with an observed stopping point, is then the sum, over all grid squares in the range of the laser ray, of the product of the conditional probability of the measurement given that the ray has stopped at that point, and the probability that the ray stopped in each square:

$$P(L, stopped = true) = \sum_{i=1}^{n} P_L(\delta_i \mid stop = i) P(stop = i \mid \boldsymbol{x}, \boldsymbol{\rho}) \tag{3.39}$$

To sum it all in a nutshell, DP-SLAM creates two Gaussians. The first Gaussian computes the probability distribution of stopping the laser ray by all squares along its trajectory (note that measurement z_t must be extended by an arbitrary extra distance). The second Gaussian computes the probability distribution of the measurement z_t (as shown in Figure 2.5) according to the distance between the stopping point and all squares along its trajectory. Finally the weight of this laser ray is obtained by multiplying both distributions. Thus, the weight of an entire scan is the sum of all individual laser ray weight.

To show how this perception model works, let's discuss an example. Suppose that at time t–1 two equals particles p_1 and p_2 (supposing that they were selected by resampling and hence they are copies of one particle at time t–2), having same map m_1 and m_2 and having the same estimated robot pose R_1 and R_2 as shown in the Figure 3.9 (a).

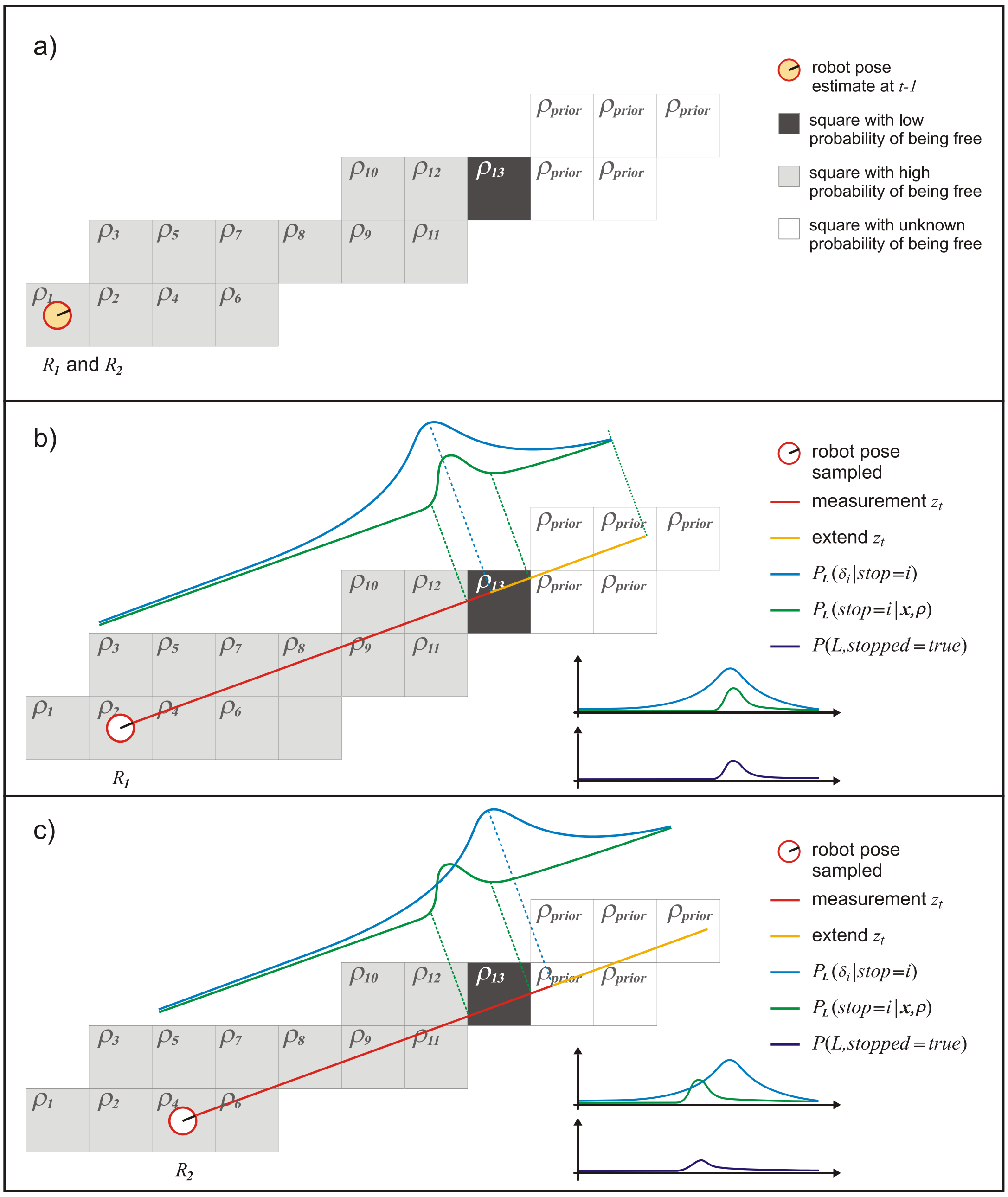
a)
robot pose estimate at t-1
square with low probability of being free
square with high probability of being free
square with unknown probability of being free
ρ_{prior}
ρ_1 ρ_2 ρ_3 ρ_4 ρ_5 ρ_6 ρ_7 ρ_8 ρ_9 ρ_{10} ρ_{11} ρ_{12} ρ_{13}
R_1 and R_2
b)
robot pose sampled
measurement z_t
extend z_t
$P_L(\delta_i|stop=i)$
$P_L(stop=i|\mathbf{x},\rho)$
$P(L,stopped=true)$
R_1
c)
R_2

Figure 3.9: Example of computing the probability of a laser ray given two sampled robot poses.

Now suppose that the robot performs a movement u_t and then does a ray measurement z_t. Using the motion model each estimated robot pose R_1 and R_2 has a new different location (predicted), as shown in Figure 3.9 (b) and (c). Weights are acquired by putting the measurement z_t (extending the measurement by an arbitrary extra distance – yellow line in the Figure 3.9 (b) and (c)) into the predicted robot positions R_1 and R_2 and then evaluating using eq. (3.39).

As illustrated in Figure 3.9 (b) and (c); the sampled robot pose R_1 has a higher probability (or weight) than the sampled robot R_2, as shown in the result (dark blue line) of multiplying $P_L(\delta_i \mid stop = i)$ (light blue line) and $P_L(stop = i \mid \boldsymbol{x}, \boldsymbol{\rho})$ (green line). More details about the opacity parameter, ρ, and how the unknown squares (unobserved previously) are treated, can be found in [6].

"DP-SLAM implements a PF over maps and robot poses, using an occupancy grid to represent the map to track the placement of objects in the environment" [6]. Thus, for a PF to properly track this joint distribution, each particle needs to maintain a separated, complete map. During the resampling in this PF, each particle could be resampled, and consequently copied, multiple times. However, because operations must be performed merely copying maps, a direct approach to this method, where a complete map is assigned to each particle, is impractical. "For a number of particles sufficient to achieve precise localization in a reasonably sized environment, this naïve approach would require gigabytes worth of data movement per update" [6].

3.2.3.2. Ancestry Tree

The greater contribution of DP-SLAM is an efficient representation of the map, making map copying more efficient, reducing the memory required to represent large numbers of occupancy grids. DP-SLAM achieves this through a method called: *Distributed Particle Mapping* (DP-Mapping), "which exploits the significant redundancies between the different maps" [6].

A particle from the distribution at time $t-1$ is called a "parent" and its successor (sampled particle) at time t is called "child", while two children with the same parent are "siblings". If a LRF sweeps out an area of size A << M (where M is the area of the total map) and if there are two siblings s_1 and s_2 (each one with a different pose), each sibling will make updates in at most an area of size A to the map it inherits form its parent. Thus the maps for s_1 and s_2 can differ of their parent in at most an area of size A, the remainder area of the map is identical.

Then DP-SLAM proposes recording a list of changes that each particle makes to its parent.

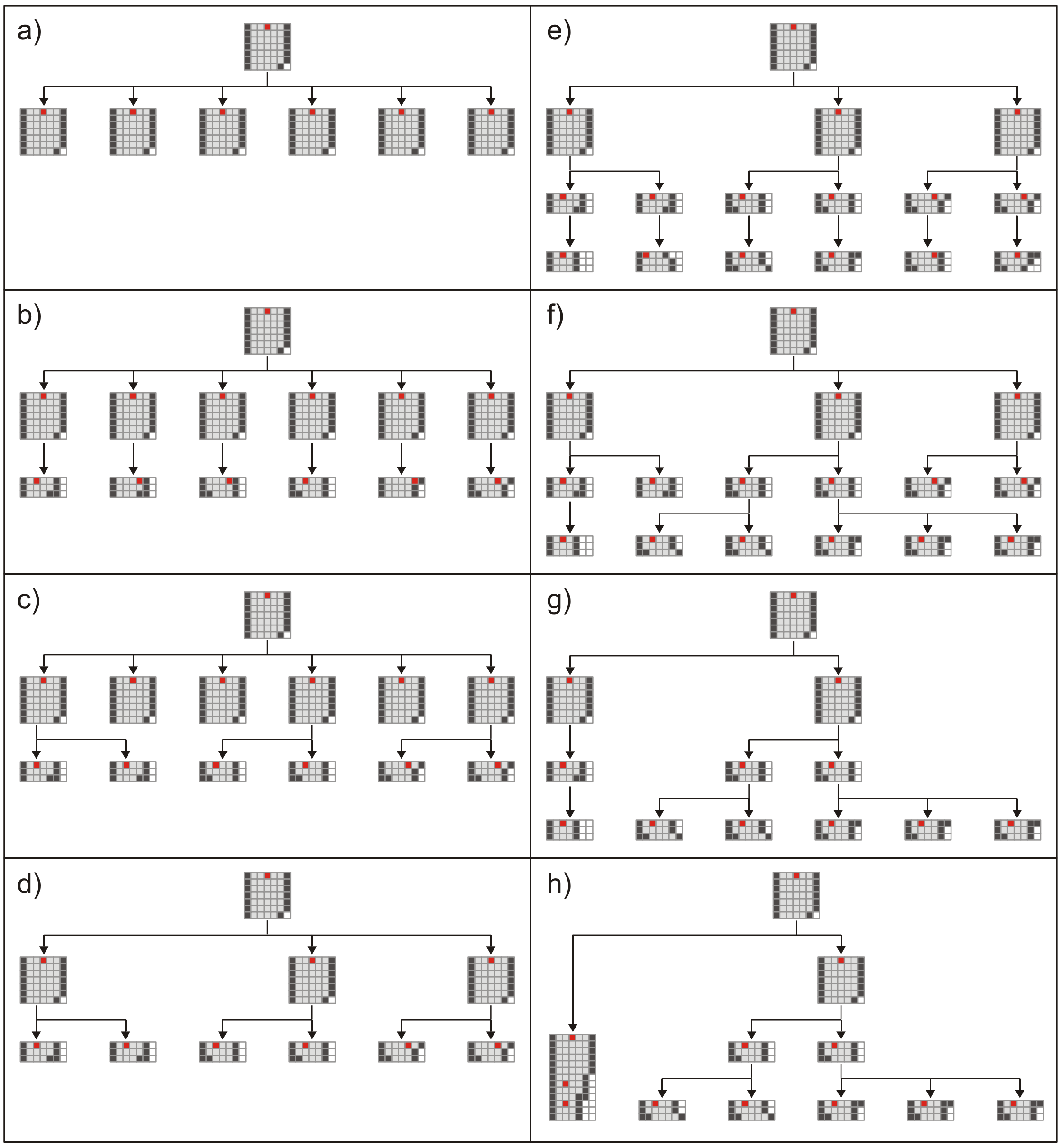

Figure 3.10: Example of particle ancestry tree maintenance

Thus DP-SLAM maintains a so called: *particle ancestry tree*, that does not forget the old particles, because to construct the entire map it is necessary not only one particle but also its ancestors. However this creates a new problem: the height of the particle ancestry tree will be linear with respect to the amount of iterations (each iteration will create a new set of particles). DP-SLAM solves this problem by defining a method of collapsing certain branches of the tree. Any particle that does not produce any surviving children can simply be removed; this may cause a series of ancestor nodes removal. Additionally, when a particle has only a single child, it is possible to merge this particle child with the particle parent and can be treated as a single particle. This "pruning" technique is explained in Figure 3.10.

Figure 3.10 (a) depicts the beginning of the process. At the top of the figure is a single particle, where the robot's pose is represented by a red square, and the current map in gray scale. This one particle is resampled many times, to give a number of identical children. The, these new particles are each propagated forward using the motion model. Thus, in Figure 3.10 (b), each particle represents a different pose, and each has a different set of map updates. Then these particles are weighed, based on how well the new updates are in agreement with the existing map, and finally, the particles are randomly resampled proportionately based on these weights, see Figure 3.10 (c).

At this point some particles have greater weight than others, and therefore were resampled more than once. Because the number of particles at each iteration is kept constant, consequently there are other particles which were not resampled. These particles (childless particles), can be removed from the ancestry tree, due to they will have no influence on any future particles, see Figure 3.10 (d).

In Figure 3.10 (e) and (f), the new set of particles are again propagated forward, and then weighed and resampled. However, on the right of Figure 3.10 (f), there is a pair of childless particles which can be removed and when this is done, their common parent will no longer have any children. Thus, this older ancestor can also be removed, as shown in Figure 3.10 (g). Also on the left of Figure 3.10 (f), if the childless ancestor particle is removed, there will be a chain of ancestor particles (on the left of Figure 3.10 (g)), each with one child. Therefore, these nodes can all be merged into a single ancestor particle and consequently collapsing the chain (on the left of Figure 3.10 (h)).

Maintaining the particle ancestry tree in this manner it is guaranteed that the tree will have a branching factor of at least two, and the depth of the tree will be no greater than the number of particles in each generation [6].

3.2.3.3. Hierarchical SLAM

The DP-SLAM provides an accurate and efficient method for building maps. However, there are some trajectories, which cover a sufficient amount of distance before completing a cycle, for which the accuracy of the map can degrade [6]. Small errors are accumulated over several iterations, and although the resulting map may look locally consistent, there is a large total error, which is more evident when the robot closes a large loop. This behavior over large distances is known as “drift”. It is a significant problem faced by essentially all current SLAM algorithms [6].

As a consequence of violated assumptions or as a consequence of particle filtering it is hard to avoid drift. Errors come from three sources: insufficient number of particles, coarse precision, and resampling itself (particle depletion). The consequence of these errors is a gradual but inevitable accumulation resulting from faults to sample, differentiate, or remember a state vector that is sufficiently close to the true state.

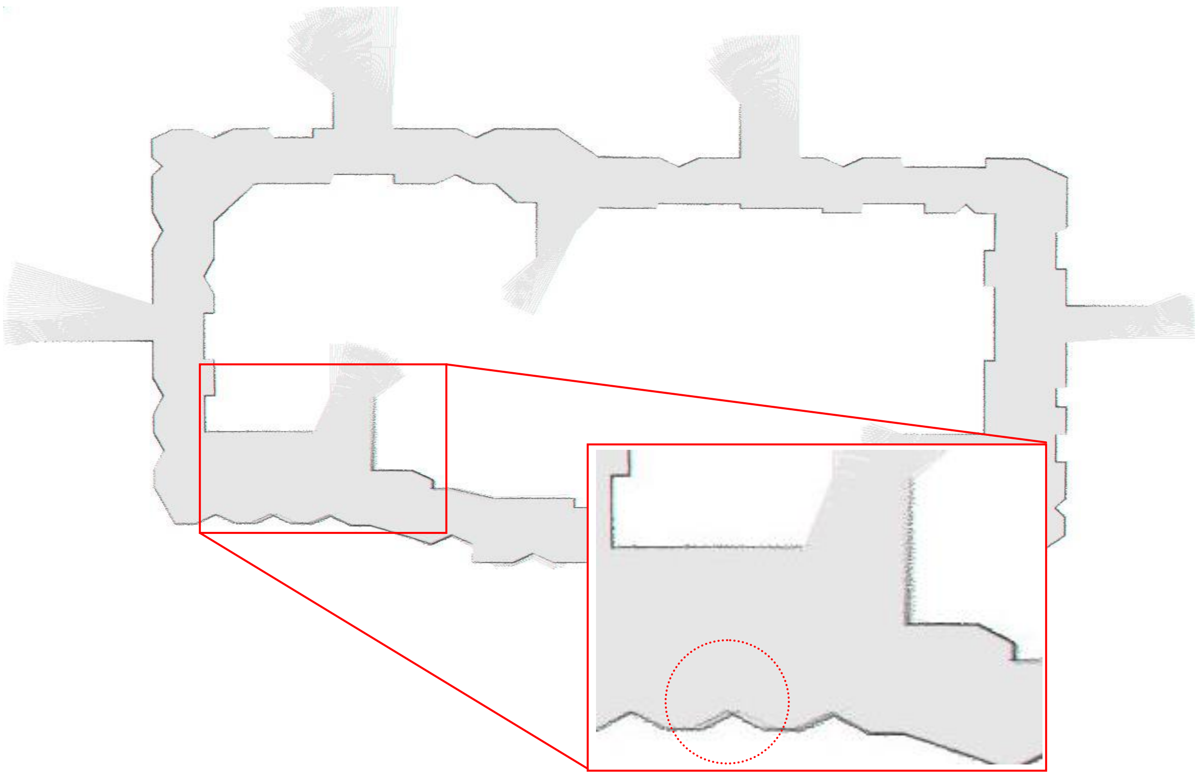

Figure 3.11: Simulated environment (60 x 40 m).

Figure 3.11 shows a loop-closed simulated environment. This map consists of 183 LRF scans. It was build using DP-SLAM (without hierarchical SLAM) with 2800 particles. This loop is large enough that particle diversity is insufficient to correct the small errors that occur.

The reason that a non-hierarchical method cannot manage this data is the extreme longevity of the uncertainty. In a large loop, small ambiguities in the beginning of the map are not resolved for many thousand iterations [6]. Non hierarchical DP-SLAM requires a huge number of particles to maintain this early particle diversity.

3.2.3.4.
Hierarchical Algorithm

DP-SLAM uses two levels Hierarchical-SLAM where the lowest level models the physical process (SLAM itself), while the higher level models errors in the lower level.

"Since the total drift over trajectory is assumed to be a summation of many small, largely independent sources of error, it can be well approximated by Gaussian distribution" [6]. Thus DP-SLAM states that the effects of drift on low level maps can be precisely approximated by perturbations on the robot's trajectory endpoints used to construct a low level map.

DP-SLAM uses a standard SLAM algorithm for the low level mapping process. The low level algorithm input is a small portion of the robot's trajectory, along with the associated observations (range scans). This low level SLAM process runs normally, and its output (a trajectory) is treated as distribution over motions (motion model) in the higher level SLAM process, to which additional noise from drift is added. So the output from each of small mapping is the input for a new SLAM process, working at a higher level of time steps.

Because the sampled trajectory is treated as an atomic motion, this defines the placement of the associated observation. “The observation model at the high level is then just the collection of observations that were made at each step along this trajectory” [6].

The high level SLAM loop for each high level particle is summarized as follows [6]:

1. Sample a high level SLAM state (high level map and robot state).

2. Perturb the sampled robot state by adding random drift.

3. Sample a low level trajectory from the distributions over trajectories returned by the low level SLAM process.

4. Compute a high-level weight by evaluating the trajectory and robot observations against the sampled high level map, starting from the perturbed robot state.

5. Update the high level map based upon the new observations.

Figure 3.12 shows an example of hierarchical SLAM. The entire map is divided into 10 small maps (light green and light blue to distinguish between them). Notice that when the loop is closing, the best path until there (represented by red lines) has a misalignment. This means that there is something wrong in its trajectory. Because it is using hierarchical DP-SLAM there is enough particle diversity and the ambiguities in the beginning of the map can be resolved for, now, 9 iterations (10 small maps).

Thus, resolving ambiguities leads to the map from Figure 3.13. Here the best path (red lines) is different one and therefore the map it carries, a better one, is different too.

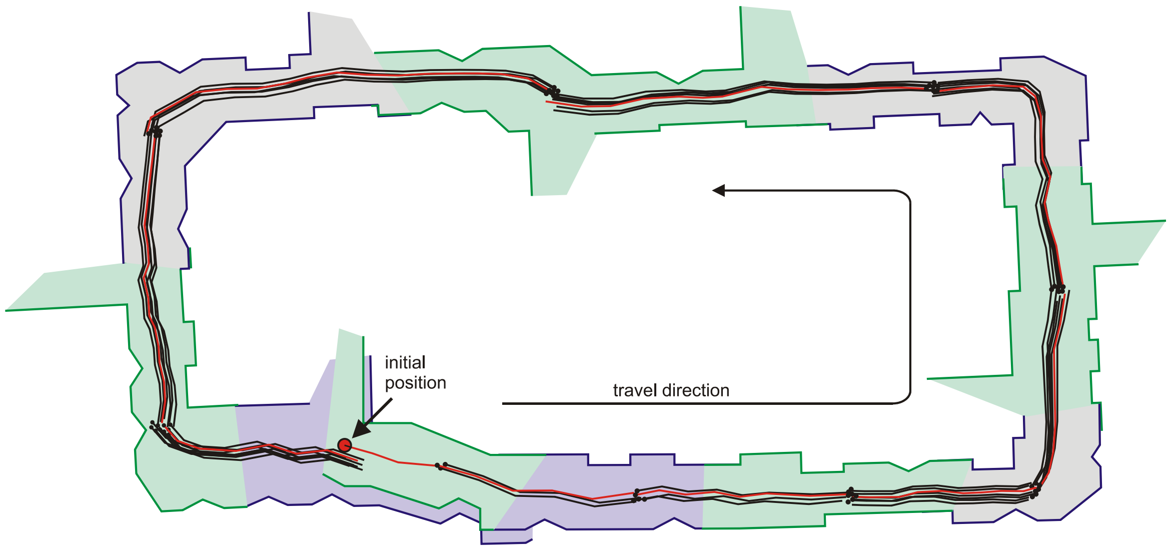

Figure 3.12: Mapping closing a loop. Each black dot is the perturbed endpoints of trajectories.

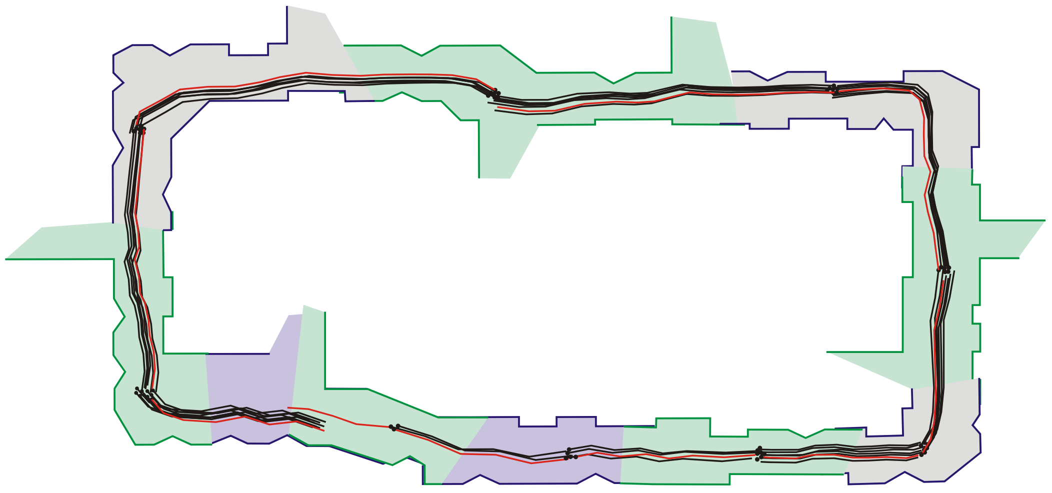

Figure 3.13: Map after ambiguities are resolved.

It is possible to implement the hierarchical SLAM for multiple levels for providing more robustness. This idea of hierarchical SLAM is not restricted to be used solely with DP-SLAM; this method could be effective when used with any other SLAM method [6].

3.3. 3D SLAM Review

Existing SLAM methods produce a two-dimensional cross section of the world, and robot motion is restricted to motion within this plane. However the assumption of a 2D world is unrealistic: wheeled robots traveling across uneven terrain and underwater autonomous vehicles, can all move with six degrees of freedom, three translational and three angular. For robots to operate in this environment, it is not only need to track these three new degrees of motion, but also to maintain a three dimensional representation of the environment.

3D mapping has some advantages compared with 2D [1]:

- 3D maps facilitate navigation. Many robot environments possess significant variation in occupancy in the vertical dimension. Modeling this can greatly reduce the danger of colliding with an obstacle.
- Many robot tasks require three-dimensional information, such as tasks involving the localization and retrieval of objects or people.
- 3D maps carry much information for a potential user of the maps. If one builds a map only for the sake or robot navigation, then the SLAM enforcements would be very few. However, if the map is acquired for later use by a person, 3D information can be absolutely critical.

Some methods exist for three-dimensional motion. They tend to represent the world in terms of a few sparse, pint-sized landmarks. These maps, while useful for localization, and possible for navigation, give very little information about the presence of objects in the world. In [24] a SLAM framework based on 3D landmarks for indoor environment with stereo vision is shown. Reference [25] shows a real-time 3D SLAM is constructed using wide-angle vision.

Carnegie Mellon University´s Mine Mapping project is a notable example of volumetric three dimensional maps, using a series of LRF set at different angles [26]. Using a combined method of both local and global scan matching techniques, a two-dimensional occupancy grid is created. Thus, with the corresponding trajectory from the robot, the remaining three-dimensional data are filled in to create the volumetric maps. Reference [27] presents an EKF-based 3D SLAM, which uses planar features probabilistically extracted from dense three-dimensional point clouds generated by a rotated 2D LRF. A similar work [28] presents SLAM from visual landmarks and 3D planes, modeling the environment as a set of planar surfaces and lines. These planar surfaces and lines are extracted by fusing data from a camera and a 3D LRF.

Also DP-SLAM [6] proposes a 3D grid map representation. This representation brings two types of challenges, technical and dimensional. The technical problems are mainly issues of sensing. In particular, odometry is unable to detect any motion in the three new degrees of freedom. The dimensional challenges arise from a new dimension added to the problem. The resources needed to deal with SLAM grow exponentially, so that merely extending previous methods is infeasible on any computer architecture.

However, this thesis is focused in indoor structured environments. Assuming a flat terrain, the localization given by the 2D DP-SLAM, can be used to project the corresponding 3D points. Thus a 3D map is constructed, composed by a set of points (a point cloud). This proposed method has similarities with the one presented in [26] where 3D maps are obtained by using the 2D pose information via the geometric projections.

Chapter 5 will show some results by applying DP-SLAM in simulated data. After creating a 2D map, the DP-SLAM algorithm gives the best estimated path. Using this, the corresponding 3D points are projected. The implemented simulator is discussed in detail in the next chapter.

4.
Detailed Implementation

4.1.
EKF SLAM

The Extended Kalman Filter (EKF) fuses all available information about the system's state to compute a state estimate. This is accomplished through a recursive three-stage cycle consisting of *prediction*, *observation* and *update* steps.

1. Prediction

This step involves computing $\overline{\lambda_t}$ and $\overline{\Sigma}_t$.

As seen in eq. (3.20), $\overline{\lambda_t}$ depends on u_t and λ_{t-1}. Using a naïve example, the control u_t could be one of two types: the first specifies the translational and rotational velocities, and the second specifies odometry information (such as distance traveled, angle turned). That is:

$$u_t = \begin{bmatrix} v_t \\ \omega_t \end{bmatrix} \quad \text{or} \quad u_t = \begin{bmatrix} d \\ \varphi \end{bmatrix} \tag{4.1}$$

Thus, the uncertainty of the control u_t is given by its covariance matrices:

$$U = \begin{bmatrix} \sigma_v & 0 \\ 0 & \sigma_\omega \end{bmatrix} \quad \text{or} \quad U = \begin{bmatrix} \sigma_d & 0 \\ 0 & \sigma_\varphi \end{bmatrix} \tag{4.2}$$

Using a landmark map representation, λ_{t-1} is a vector containing the robot and landmark positions at one time step earlier. That is:

$$\lambda_{t-1} = [\underbrace{Rx_{t-1} \quad Ry_{t-1} \quad R\theta_{t-1}}_{\text{Robot position}} \quad \underbrace{L_1x_{t-1} \quad L_1y_{t-1}}_{\text{Landmark 1 position}} \quad \ldots \quad \underbrace{L_nx_{t-1} \quad L_ny_{t-1}}_{\text{Landmark n position}}]^T \tag{4.3}$$

Figure 4.1 shows the robot position at the previous time step, *t–1*, and the predicted robot position made by the odometry information in a Cartesian plane. The predicted state vector $\bar{\lambda}_t$ is given by

$$f(u_t, \lambda_{t-1}) = \begin{bmatrix} \bar{R}x \\ \bar{R}y \\ \bar{R}\theta \end{bmatrix} = \begin{bmatrix} Rx_{t-1} + d\cos(R\theta_{t-1} + \varphi) \\ Ry_{t-1} + d\sin(R\theta_{t-1} + \varphi) \\ R\theta_{t-1} + \varphi \end{bmatrix} \tag{4.4}$$

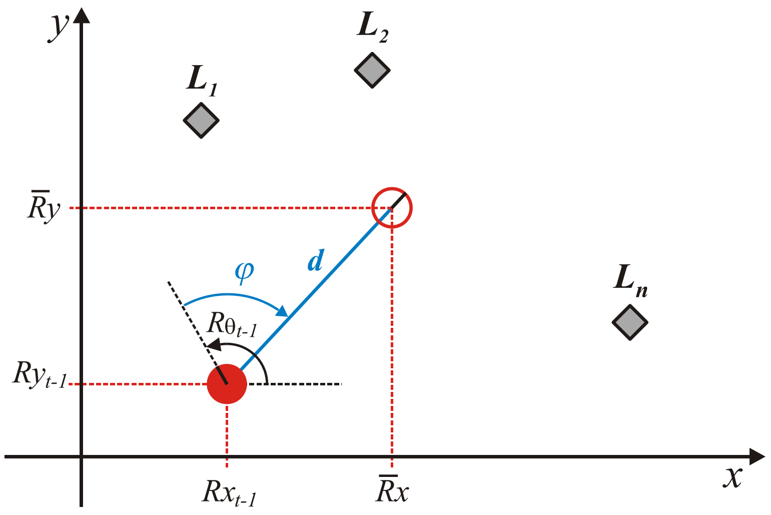

Figure 4.1: Robot position (red fill circle) at time *t–1* , and predicted robot position (white filled circle).

Notice however, that it is not necessary to predict landmark positions. Thus, the predicted state vector $\bar{\lambda}_t$ is now

$$\bar{\lambda}_t = \begin{bmatrix} \bar{R}x & \bar{R}y & \bar{R}\theta & \bar{L}_1x & \bar{L}_1y & \bar{L}_2x & \bar{L}_2y & \ldots & \bar{L}_nx & \bar{L}_ny \end{bmatrix}^T$$

where

$$\begin{bmatrix} \bar{L}_1x & \bar{L}_1y & \bar{L}_2x & \bar{L}_2y & \ldots & \bar{L}_nx & \bar{L}_ny \end{bmatrix}^T = \begin{bmatrix} L_1x_{t-1} & L_1y_{t-1} & L_2x_{t-1} & L_2y_{t-1} & \ldots & L_nx_{t-1} & L_ny_{t-1} \end{bmatrix}^T$$

In order to compute the predicted covariance $\bar{\Sigma}_t$, as in eq. (3.21), F_t is given by:

$$F_t = \frac{\partial f(u_t, \lambda_{t-1})}{\partial_{\lambda_{t-1}}} = \begin{bmatrix} 1 & 0 & -d\sin(R\theta_{t-1}+\varphi) \\ 0 & 1 & d\cos(R\theta_{t-1}+\varphi) \\ 0 & 0 & 1 \end{bmatrix} \tag{4.5}$$

Notice that F_t is a matrix of size *m* x *m*, where *m* is the dimension of the state vector (3+2*n*), being *n* the number of landmarks. However since the environment is stationary, again, movement of landmarks does not need to be predicted, thus the remaining elements in F_t are zero.

P_t is given by eq. (4.6) where *U* was described in eq. (4.2) and Jf_{u_t} is given by:

$$Jf_{u_t} = \frac{\partial f(u_t, \lambda_{t-1})}{\partial_{u_t}} = \begin{bmatrix} \cos(R\theta_{t-1}+\varphi) & -d\sin(R\theta_{t-1}+\varphi) \\ \sin(R\theta_{t-1}+\varphi) & d\cos(R\theta_{t-1}+\varphi) \\ 0 & 1 \end{bmatrix} \tag{4.6}$$

$$P_t = Jf_{u_t}\, U\, Jf_{u_t}^T \tag{4.7}$$

In the same way, Jf_{u_t} is of size *m* x 2; however the elements related to landmarks are zero. Thus the mean $\overline{\lambda}_t$ is the predicted state vector of size (3+2*n*) x 1 and $\overline{\Sigma}_t$ the predicted covariance matrix of size (3+2*n*) x (3+2*n*).

2. Observation

The observation step computes the innovation vector and the innovation covariance, that is $\left[z_t - h(\overline{\lambda}_t)\right]$ and $\left(H_t\, \overline{\Sigma}_t\, H_t^T + Q\right)$ in the eq. (3.23) and eq. (3.22), respectively.

The perception function, $h(\overline{\lambda}_t)$, that represents the predicted landmark position seen from the predicted robot position is shown in Figure 4.2.

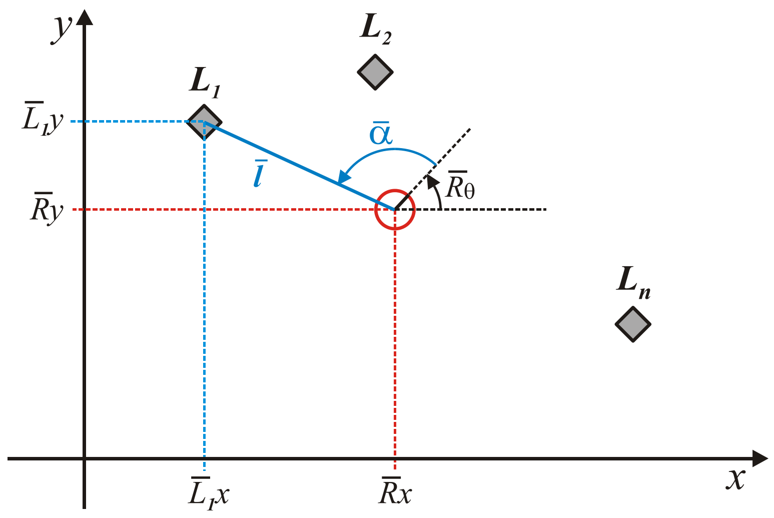

Figure 4.2: Predicted landmark position seen from the predicted robot position

In the same Cartesian plane, the predicted distance and angle ($\bar{l}$ and $\bar{\alpha}$) from the predicted robot position to the landmark L_1, is given by eq. (4.8):

$$h(\bar{\lambda}) = \begin{bmatrix} \bar{l} \\ \bar{\alpha} \end{bmatrix} = \begin{bmatrix} \sqrt{(\bar{L}_1 x - \bar{R}x)^2 + (\bar{L}_1 y - \bar{R}y)^2} \\ \arctan(\bar{L}_1 y - \bar{R}y / \bar{L}_1 x - \bar{R}x) - \bar{R}\theta \end{bmatrix} \tag{4.8}$$

Note that $h(\bar{\lambda}_t)$ shown in eq. (4.8) is written for the Landmark 1, in the same way it must be computed for the n landmarks. Thus, the size of the vectors $h(\bar{\lambda}_t)$ and the z_t is $2n$.

To compute the matrix H_t, the Jacobian of h at $\bar{\lambda}_t$ is given by

$$H_t = \frac{\partial h(\bar{\lambda})}{\partial_{\bar{\lambda}}} = \begin{bmatrix} \frac{\partial}{\partial \bar{R}x}\bar{l} & \frac{\partial}{\partial \bar{R}y}\bar{l} & \frac{\partial}{\partial \bar{R}\theta}\bar{l} & \frac{\partial}{\partial \bar{L}_1 x}\bar{l} & \frac{\partial}{\partial \bar{L}_1 y}\bar{l} \\ \frac{\partial}{\partial \bar{R}x}\bar{\alpha} & \frac{\partial}{\partial \bar{R}y}\bar{\alpha} & \frac{\partial}{\partial \bar{R}\theta}\bar{\alpha} & \frac{\partial}{\partial \bar{L}_1 x}\bar{\alpha} & \frac{\partial}{\partial \bar{L}_1 y}\bar{\alpha} \end{bmatrix} \tag{4.9}$$

$$H_t = \begin{bmatrix} \frac{-d_x}{\sqrt{d_x^2 + d_y^2}} & \frac{-d_y}{\sqrt{d_x^2 + d_y^2}} & \boldsymbol{0} & \frac{d_x}{\sqrt{d_x^2 + d_y^2}} & \frac{d_y}{\sqrt{d_x^2 + d_y^2}} \\ \frac{d_y}{d_x^2 + d_y^2} & \frac{-d_x}{d_x^2 + d_y^2} & -1 & \frac{-d_y}{d_x^2 + d_y^2} & \frac{d_x}{d_x^2 + d_y^2} \end{bmatrix}$$

where

$$d_x = \bar{L}_1 x - \bar{R}x \quad \text{and} \quad dy = \bar{L}_1 y - \bar{R}y$$

Notice however, that eq. (4.9) shows H_t using only the Landmark 1, thus the true size of H_t is 2 x (3+2n).

$$H_t = \frac{\partial h(\bar{\lambda})}{\partial_{\bar{\lambda}}} = \begin{bmatrix} \frac{\partial}{\partial \bar{R}} \bar{\boldsymbol{l}} & \frac{\partial}{\partial L_1} \bar{\boldsymbol{l}} & \cdots & \frac{\partial}{\partial L_n} \bar{\boldsymbol{l}} \\ \frac{\partial}{\partial \bar{R}} \overline{\alpha} & \frac{\partial}{\partial L_1} \overline{\alpha} & \cdots & \frac{\partial}{\partial L_n} \overline{\alpha} \end{bmatrix} \tag{4.10}$$

and Q_t represents the covariance matrix for the sensor noise:

$$Q = \begin{bmatrix} \sigma_l & 0 \\ 0 & \sigma_\alpha \end{bmatrix} \tag{4.11}$$

3. Update

Finally, this last step computes the desired λ_t and Σ_t, using eq. (3.22), eq. (3.23) and eq. (3.24).

It is important to point out that in the beginning, where the robot starts the mapping process, it may not see all landmarks, or not even one. Therefore, as the robot moves through the environment, the state vector λ_t grows. Thus, when a new landmark is acquired, the state vector is augmented. Figure 4.3 shows how the robot sees a new landmark (*p*) at distance *l* and at angle *α*; eq. (4.12) and eq. (4.13) show how this is modeled.

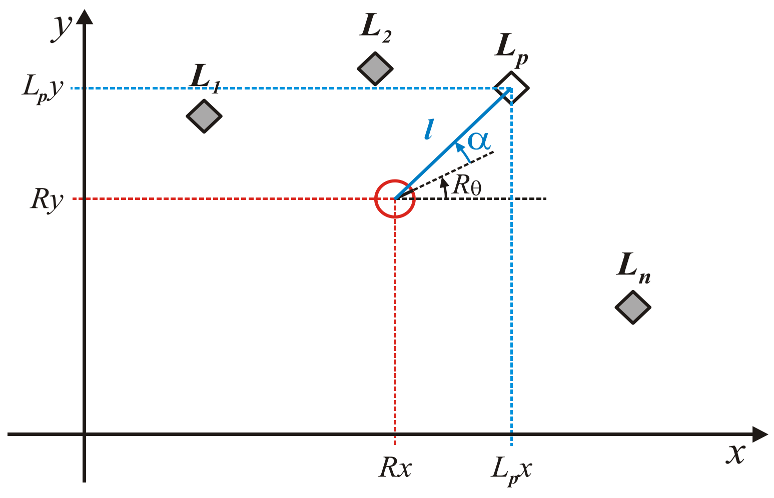

Figure 4.3: New landmark $\boldsymbol{L_p}$, is added to the state vector.

$$zp = \begin{bmatrix} L_p x \\ L_p y \end{bmatrix} = \begin{bmatrix} Rx + \boldsymbol{l}\cos(R\theta + \alpha) \\ Ry + \boldsymbol{l}\sin(R\theta + \alpha) \end{bmatrix} \tag{4.12}$$

$$\lambda_t := \begin{bmatrix} \lambda_t \\ L_p \end{bmatrix} \tag{4.13}$$

As it was seen in Section 3.2.2, the covariance matrix Σ_t, represents the relationships landmarks-robot and landmarks-landmarks (because the robot's pose uncertainty correlates landmark positions), these relationships are shown in eq. (4.14).

$$\Sigma_t = \begin{bmatrix} \boxed{\begin{matrix} C_{RR} \\ \text{(3x3)} \end{matrix}} & \boxed{\begin{matrix} C_{RL_1} \\ \text{(3x2)} \end{matrix}} & \cdots & \boxed{\begin{matrix} C_{RL_n} \\ \text{(3x2)} \end{matrix}} \\ \boxed{\begin{matrix} C_{RL_1}{}^T \\ \text{(2x3)} \end{matrix}} & \boxed{\begin{matrix} C_{L_1L_1} \\ \text{(2x2)} \end{matrix}} & \cdots & \boxed{\begin{matrix} C_{L_1L_n} \\ \text{(2x2)} \end{matrix}} \\ \vdots & \vdots & \ddots & \\ \boxed{\begin{matrix} C_{RL_n}{}^T \\ \text{(2x3)} \end{matrix}} & \boxed{\begin{matrix} C_{L_1L_n}{}^T \\ \text{(2x2)} \end{matrix}} & & \boxed{\begin{matrix} C_{L_nL_n} \\ \text{(2x2)} \end{matrix}} \end{bmatrix} \tag{4.14}$$

In the same way the covariance matrix Σ_t grows in dimension to include the new landmark. To do this, the covariance matrices, C_{LpLp} (L_p to L_p), C_{RLp} (robot to L_p) and C_{L1Lp} … C_{LnLp} (all old landmarks L_1... L_n to L_p) are computed by eq. (4.15), eq. (4.16) and eq. (4.17), respectively.

$$C_{LpLp} = \underset{Rx,Ry,R\theta}{Jz_p}\; C_{RR}\; \underset{Rx,Ry,R\theta}{Jz_p}^{T} + \underset{l,\alpha}{Jz_p}\; Q_t\; \underset{l,\alpha}{Jz_p}^{T} \tag{4.15}$$

$$C_{RLp} = \underset{Rx,Ry,R\theta}{Jzp}\; C_{RR} \tag{4.16}$$

$$C_{L_1Lp} \ldots C_{LnLp} = \underset{Rx,Ry,R\theta}{Jz_p} \begin{bmatrix} C_{RL_1} & \ldots & C_{RL_n} \end{bmatrix} \tag{4.17}$$

where Jz_p are the Jacobians:

$$\underset{Rx,Ry,R\theta}{Jz_p} = \begin{bmatrix} \frac{\partial}{\partial Rx} L_p x & \frac{\partial}{\partial Ry} L_p x & \frac{\partial}{\partial R\theta} L_p x \\ \frac{\partial}{\partial Rx} L_p y & \frac{\partial}{\partial Ry} L_p y & \frac{\partial}{\partial R\theta} L_p y \end{bmatrix} = \begin{bmatrix} 1 & 0 & -\boldsymbol{l}\cos(R\theta + \alpha) \\ 0 & 1 & \boldsymbol{l}\sin(R\theta + \alpha) \end{bmatrix} \tag{4.18}$$

$$\underset{l,\alpha}{Jz_p} = \begin{bmatrix} \frac{\partial}{\partial \boldsymbol{l}} L_p x & \frac{\partial}{\partial \alpha} L_p x \\ \frac{\partial}{\partial \boldsymbol{l}} L_p y & \frac{\partial}{\partial \alpha} L_p y \end{bmatrix} = \begin{bmatrix} \cos(R\theta + \alpha) & -\boldsymbol{l}\sin(R\theta + \alpha) \\ \sin(R\theta + \alpha) & \boldsymbol{l}\cos(R\theta + \alpha) \end{bmatrix} \tag{4.19}$$

Finally, the augmented covariance matrix looks like eq. (4.20), representing now: $n{:}=n+1$ landmarks.

$$\Sigma_t = \begin{bmatrix} \boxed{\begin{matrix} C_{RR} \\ \text{(3x3)} \end{matrix}} & \boxed{\begin{matrix} C_{RL_1} \\ \text{(3x2)} \end{matrix}} & \cdots & \boxed{\begin{matrix} C_{RL_n} \\ \text{(3x2)} \end{matrix}} & \boxed{\begin{matrix} C_{RL_p} \\ \text{(3x2)} \end{matrix}} \\ \boxed{\begin{matrix} C_{RL_1}^{T} \\ \text{(2x3)} \end{matrix}} & \boxed{\begin{matrix} C_{L_1L_1} \\ \text{(2x2)} \end{matrix}} & \cdots & \boxed{\begin{matrix} C_{L_1L_n} \\ \text{(2x2)} \end{matrix}} & \boxed{\begin{matrix} C_{L_1L_p} \\ \text{(2x2)} \end{matrix}} \\ \vdots & \vdots & \ddots & & \vdots \\ \boxed{\begin{matrix} C_{RL_n}^{T} \\ \text{(2x3)} \end{matrix}} & \boxed{\begin{matrix} C_{L_1L_n}^{T} \\ \text{(2x2)} \end{matrix}} & & \boxed{\begin{matrix} C_{L_nL_n} \\ \text{(2x2)} \end{matrix}} & \boxed{\begin{matrix} C_{L_nL_p} \\ \text{(2x2)} \end{matrix}} \\ \boxed{\begin{matrix} C_{RL_p}^{T} \\ \text{(2x3)} \end{matrix}} & \boxed{\begin{matrix} C_{L_1L_p}^{T} \\ \text{(2x2)} \end{matrix}} & \cdots & \boxed{\begin{matrix} C_{L_nL_p}^{T} \\ \text{(2x2)} \end{matrix}} & \boxed{\begin{matrix} C_{L_pL_p} \\ \text{(2x2)} \end{matrix}} \end{bmatrix} \qquad (4.20)$$

4.2. FastSLAM

The Fast Slam algorithm receives as input the previous distribution $p(x_{t-1})$, as a particle set $\Phi_{t-1} := \{\langle s_{t-1}^{i} \rangle / i = 1...N\}$, the odometry (or control) information u_t, and the landmark measurements z_t. From the idea exposed in Section 2.2.4, the FastSLAM algorithm uses the following steps.

1. Each particle i representing the robot position at time t–1, R_{t-1}^{i}, from the set Φ_{t-1}, is moved following the control vector u_t and the motion model.

$$u_t = \begin{bmatrix} v_t \\ \omega_t \end{bmatrix} \quad \text{or} \quad u_t = \begin{bmatrix} d_t \\ \varphi_t \end{bmatrix} \qquad (4.21)$$

Table 4.1 shows an algorithm [1] for sampling from the motion model $p(R_t | u_t, R_{t-1})$ to generate a random pose R_t^i. Lines 1 and 2 perturb the commanded control parameters with noise, drawn from the error parameters α_1 to α_6 (a detailed explanation of these error parameters can be found in [1]). The noise values are then used to generate the sample's new pose in lines 4 through 7.

Table 4.1: Sample Motion Model Algorithm [1]

```
Sample Motion Model_algorithm ($R_{t-1}$, $u_t$)
1:    $\hat{v} = v_t + sample(\alpha_1 |v_t| + \alpha_1 |\omega_t|)$
2:    $\hat{\omega} = \omega_t + sample(\alpha_3 |v_t| + \alpha_4 |\omega_t|)$
3:    $\hat{\gamma} = sample(\alpha_5 |v_t| + \alpha_6 |\omega_t|)$
4:    $Rx_t = Rx_{t-1} - \frac{\hat{v}}{\hat{\omega}} \sin(R\theta_{t-1}) + \frac{\hat{v}}{\hat{\omega}} \sin(R\theta_{t-1} + \hat{\omega}\Delta t)$
5     $Ry_t = Ry_{t-1} + \frac{\hat{v}}{\hat{\omega}} \cos(R\theta_{t-1}) - \frac{\hat{v}}{\hat{\omega}} \cos(R\theta_{t-1} + \hat{\omega}\Delta t)$
6:    $R\theta_t = R\theta_{t-1} + \hat{\omega}\Delta t + \hat{\gamma}\Delta t$
7:    return $R_t = (Rx_t, Ry_t, R\theta_t)$
```

Figure 4.4 illustrates the outcome of this sampling routine. A temporal particle set $\hat{\Phi} = \{R_t^1, R_t^2, \ldots R_t^p\}$ containing all the samples is created, where p is the number of samples (particles).

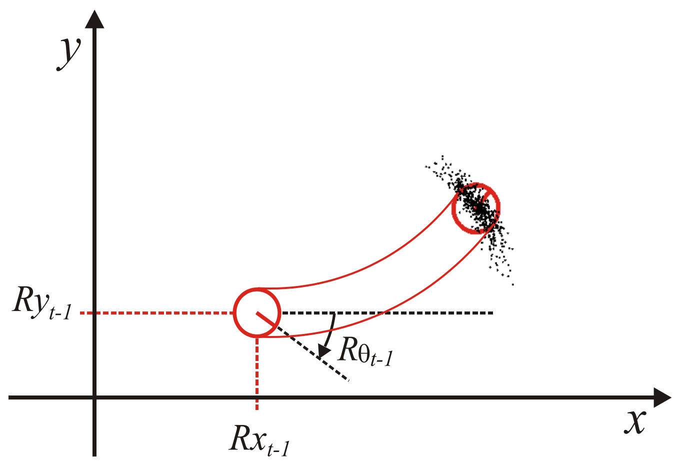

Figure 4.4: Sampling. Each black dot represents a possible robot position.

2. Update the estimation of landmarks, using the EKF, the set $\hat{\Phi}$ of robot poses samples created in step 1, and the landmark measurements z_t.

   Because the jth landmark positions ($L_j^i x_{t-1}$, $L_j^i y_{t-1}$) is known at time t–1 as well as the poses ($R^i x_t, R^i y_t$) and rotations ($R^i \theta_t$) of each particle (obtained in step 1), it is possible to compute the distance and angle between them, as shown in Figure 4.5, where $\hat{r}_j^i$ and $\hat{\phi}_j^i$ are the distance and angle between particle *i* and landmark *j*.

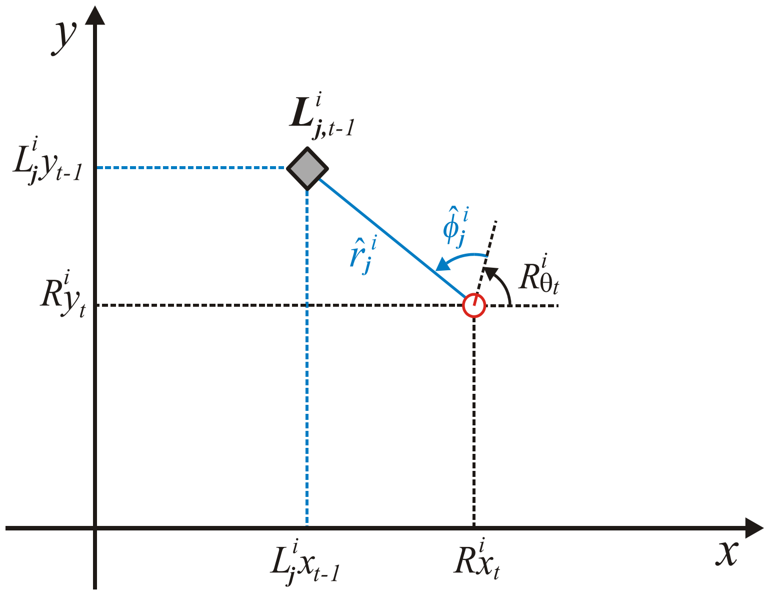

Figure 4.5: Distance and rotation between particle *i* and landmark *j*.

Thus, function *h* used by the EKF is given by:

$$h_j^i = \begin{bmatrix} \hat{r}_j^i \\ \hat{\phi}_j^i \end{bmatrix} = \begin{bmatrix} \sqrt{(L_j^i x_{t-1} - R^i x_t)^2 + (L_j^i y_{t-1} - R^i y_t)^2} \\ \arctan((L_j^i y_{t-1} - R^i y_t)/(L_j^i x_{t-1} - R^i x_t)) - R^i \theta_t \end{bmatrix} \tag{4.22}$$

and the Jacobian of h_j^i, named H_j^i, is

$$H_j^i = \frac{\partial h_j^i}{\partial_{L_{j,t-1}}} = \begin{bmatrix} \frac{\partial}{\partial_{L_j x_{t-1}}} \hat{r}_j^i & \frac{\partial}{\partial_{L_j y_{t-1}}} \hat{r}_j^i \\ \frac{\partial}{\partial_{L_j x_{t-1}}} \hat{\phi}_j^i & \frac{\partial}{\partial_{L_j y_{t-1}}} \hat{\phi}_j^i \end{bmatrix} = \begin{bmatrix} \frac{a}{\sqrt{a^2+b^2}} & \frac{b}{\sqrt{a^2+b^2}} \\ \frac{-b}{a^2+b^2} & \frac{a}{a^2+b^2} \end{bmatrix} \tag{4.23}$$

where

$$a = L_j^i x_{t-1} - R^i x_t \qquad b = L_j^i y_{t-1} - R^i y_t$$

In addition, the covariance of the landmark positions $\Sigma^i_{j,t-1}$ is known. Thus, the landmark updates are computed as follows:

$$S^i_j = H^i_j \Sigma^i_{j,t-1} H^{i\,T}_j + Q \tag{4.24}$$

$$W^i_j = \Sigma^i_{j,t-1} H^{i\,T}_j S^{i\,-1}_j \tag{4.25}$$

$$Z = z_{j,t} - h^i_j \tag{4.26}$$

$$\lambda^i_{j,t} = \lambda^i_{j,t-1} + W^i_2 Z \tag{4.27}$$

$$\Sigma^i_{j,t} = \Sigma^i_{j,t-1} - W^i_j S^i_j W^{i\,T}_j \tag{4.28}$$

where $z_{j,t}$ is the j^{th} landmark sensor observation in z_t and Q represents the covariance matrix for the sensor noise, that is:

$$Q = \begin{bmatrix} \sigma_d & 0 \\ 0 & \sigma_\phi \end{bmatrix} \tag{4.29}$$

The following figure shows the updated landmark j for the particle i, namely $L^i_{j,t}$, represented by the blue arrow.

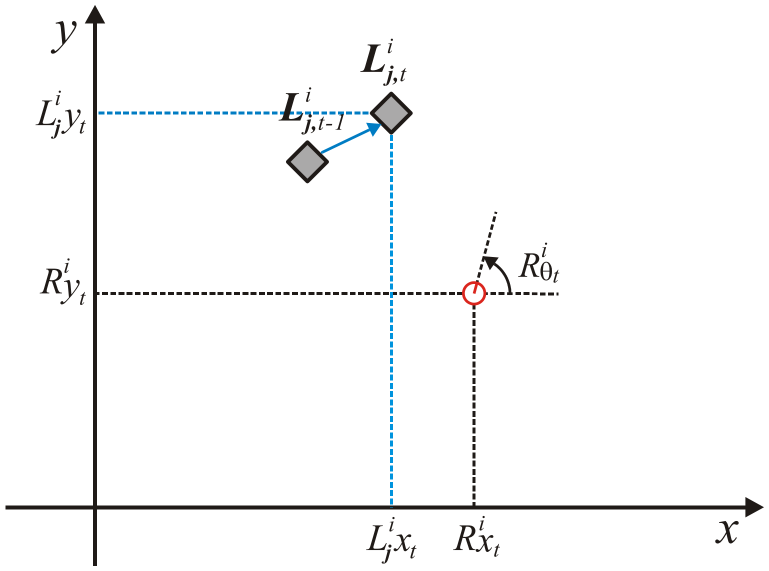

Figure 4.6: Updated landmark *j* for the particle *i*.

Note that this update is made for landmark *j* and particle *i*, thus it must be repeated *n* x *p* times, being *n* the number of observed landmarks at time *t* (the unobserved landmarks are not updated) and *p* the number of particles.

This set of median and covariance are added to the temporal particles set, as follows:

$$\begin{aligned}\hat{\Phi} = \{&R_t^1, \lambda_{1,t}^1, \Sigma_{1,t}^1, \ldots, \lambda_{n,t}^1, \Sigma_{n,t}^1, \\ &R_t^2, \lambda_{1,t}^2, \Sigma_{1,t}^2, \ldots, \lambda_{n,t}^2, \Sigma_{n,t}^2, \\ &R_t^p, \lambda_{1,t}^p, \Sigma_{1,t}^p, \ldots, \lambda_{n,t}^p, \Sigma_{n,t}^p\}\end{aligned} \tag{4.30}$$

3. Assign the weight for each particle. Using the measurement vector z_t, each particle of the temporal particle set $\hat{\Phi}$ is evaluated.

   Because the *j*th updated landmark positions ($L_j^i x_t$, $L_j^i y_t$) and the poses ($R^i x_t$, $R^i y_t$) and rotations ($R^i \theta_t$) of each particle is known (obtained in the 1), it is possible, once more, to compute the distance and angle between them, as shown in Figure 4.7, where r_j^i and ϕ_j^i are the distance and angle between particle *i* and the updated landmark *j*.

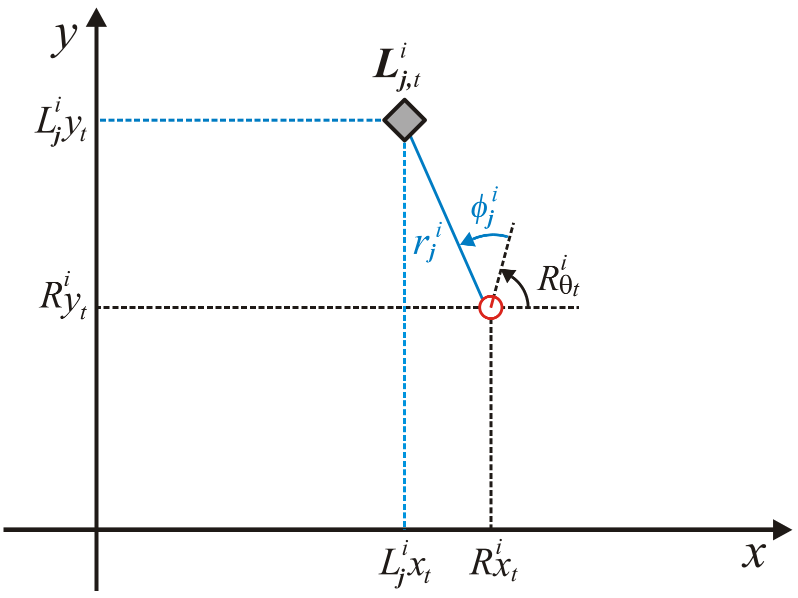

Figure 4.7: Distance and rotation between particle *i* and updated landmark *j*.

Now, the function h_j^i is

$$h_j^i = \begin{bmatrix} r_j^i \\ \phi_j^i \end{bmatrix} = \begin{bmatrix} \sqrt{(L_j^i x_t - R^i x_t)^2 + (L_j^i y_t - R^i y_t)^2} \\ \arctan((L_j^i y_t - R^i y_t)/(L_j^i x_t - R^i x_t)) - R^i \theta_t \end{bmatrix} \tag{4.31}$$

and the Jacobian of h_j^i, defined as H_j^i, becomes

$$H_j^i = \frac{\partial h_j^i}{\partial_{L_{j,t}}} = \begin{bmatrix} \frac{a}{\sqrt{a^2+b^2}} & \frac{b}{\sqrt{a^2+b^2}} \\ \frac{-b}{a^2+b^2} & \frac{a}{a^2+b^2} \end{bmatrix} \tag{4.32}$$

where

$$a = L_j^i x_t - R^i x_t \qquad b = L_j^i y_t - R^i y_t$$

The updated covariance of the landmark positions $\Sigma_{j,t}^i$ is also known. Thus, the importance factors (weights) can be computed, as follows:

Table 4.2: Compute weights algorithm;

```
Compute weights_algorithm ($\hat{\Phi}$ , $z_t$)
1:    for $i$ =1 to $p$ do
2:    $w_t^i = 1$
3:        for $j$=1 to $n$ do
4             $U_j^i = H_j^i \Sigma_{j,t}^i H_j^{i\,T} + Q$
5:            $w_t^i := w_t^i * \det(2\pi U_j^i)^{-\frac{1}{2}} \exp\{-\frac{1}{2}(z_{j,t} - h_j^i)^T U_j^{i\,-1}(z_{j,t} - h_j^i)\}$
6:        end for
7:    end for
```

where, once again, $z_{j,t}$ is the j^{th} landmark sensor observation. This set of importance factors is added to the temporal particles set:

$$\begin{aligned}\hat{\Phi} = \{ & w_t^1, R_t^1, \lambda_{1,t}^1, \Sigma_{1,t}^1, \ldots, \lambda_{n,t}^1, \Sigma_{n,t}^1, \\ & w_t^2, R_t^2, \lambda_{1,t}^2, \Sigma_{1,t}^2, \ldots, \lambda_{n,t}^2, \Sigma_{n,t}^2, \\ & w_t^p, R_t^p, \lambda_{1,t}^p, \Sigma_{1,t}^p, \ldots, \lambda_{n,t}^p, \Sigma_{n,t}^p \}\end{aligned} \tag{4.33}$$

4. Finally, resample. Each particle, in the temporal particle set, is drawn (with replacement) with a probability proportional to its importance factor.

   Prior to resampling, the weights of particles should be normalized such that they sum up to one. Then, compute the cumulative probability density function (*cdf*) which defines intervals that reflect each particle "share" of the total probability, as illustrated Figure 4.8. Draw *p* times one particle by generating *p* independent uniformly distributed random numbers *r* in the interval [0,1]; obviously the "heaviest" particles are more likely to be drawn.

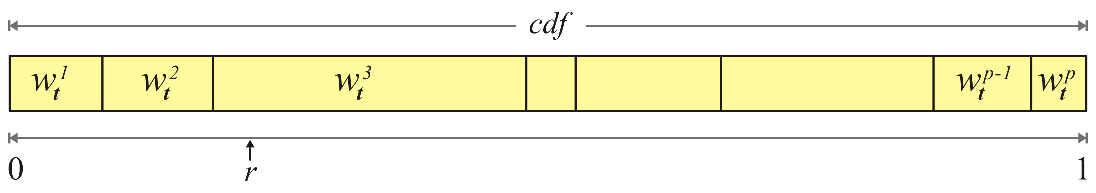

Figure 4.8: Cumulative probability distribution and a random number *r*.

The output of resampling step is a new set Φ_t that possesses many duplicates, since particles are drawn with replacement. This new set is distributed according to the desired posterior $p(x_t)$.

5. If the measurement vector z_t, introduces a new landmark never seen before, this needs to be included into the set of particles, as follows.

The new observed landmark in z_t consist of its distance r_q and its angle φ_q referenced to the unknown true robot position, as shown in Figure 4.9 and eq. (4.34).

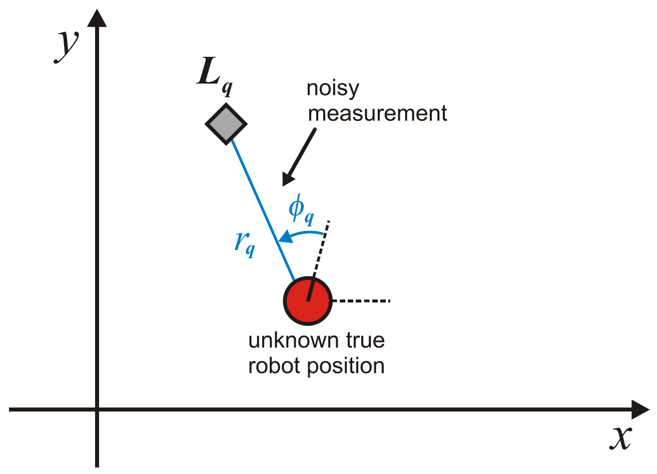

Figure 4.9: New observed landmark L_q.

$$L_q = \begin{bmatrix} r_q \\ \phi_q \end{bmatrix} \tag{4.34}$$

The new landmark L_q must be included within each particle in the particle set through its mean and covariance. Thus, for each particle, function h_q^i and its Jacobian H_q^i are given by:

$$h_q^i = \begin{bmatrix} x_q^i \\ y_q^i \end{bmatrix} = \begin{bmatrix} R^i x_t + r_q \cos(R^i\theta_t + \phi_q) \\ R^i y_t + r_q \sin(R^i\theta_t + \phi_q) \end{bmatrix} \tag{4.35}$$

$$H_q^i = \frac{\partial h_q^i}{\partial_{L_q}} = \begin{bmatrix} \cos(R^i\theta_t + \phi_q) & -r_n \sin(R^i\theta_t + \phi_q) \\ \sin(R^i\theta_t + \phi_q) & r_n \cos(R^i\theta_t + \phi_q) \end{bmatrix} \tag{4.36}$$

The mean is $\lambda_{q,t}^i = h_j^i$ and the covariance, $\Sigma_{q,t}^i$, is computed using the covariance matrix for the sensor noise Q:

$$\Sigma_{q,t}^{i} = H_q^i Q H_q^{i\,T} \tag{4.37}$$

Now the particle set Φ_t has a new landmark incorporated, making the number of total landmarks become n:=*n+1*.

4.3. Simulator

To test the grid mapping algorithm, it is necessary to acquire data from a LRF mounted on a robot that moves along a structured environment. It is also possible to evaluate the algorithm from simulations of both the environment and the LRF readings, as long as noise is introduced in the process.

The simulation of the robot perception based on LRF provides several advantages. First of all, it is cheaper than experimenting with a real device. The simulator gives the opportunity to concentrate more on the intelligence algorithms such as localization and mapping (SLAM). Developing the simulator is easier than building a new robot or perception system [29], due to the testability of many configurations.

The simulator used in this work is implemented on Matlab®, explaining as follows.

4.3.1. 3D Environment Simulation

The element used in the simulator to represent the structured environment is the plane. All structured environment elements are approximated using planes; straight walls, curved walls, doors, windows, floors, ceilings, etc, can be modeled using a group of rectangles. Figure 4.10 shows an environment constructed in such a way.

Each rectangle in this simulator is defined by four points, from which their equation obtained. Thus taking, three points (*a*,*b*,*c*) of the four given points, the equation of the plane that contains this rectangle is given by:

$$n_x(x-a_x)+n_y(y-a_y)+n_z(z-a_z)=0 \tag{4.38}$$

where

$$\begin{bmatrix} n_x \\ n_y \\ n_z \end{bmatrix} = (\boldsymbol{b}-\boldsymbol{a})\times(\boldsymbol{c}-\boldsymbol{a}) = \left(\begin{bmatrix} b_x \\ b_y \\ b_z \end{bmatrix} - \begin{bmatrix} a_x \\ a_y \\ a_z \end{bmatrix}\right) \times \left(\begin{bmatrix} c_x \\ c_y \\ c_z \end{bmatrix} - \begin{bmatrix} a_x \\ a_y \\ a_z \end{bmatrix}\right) \tag{4.39}$$

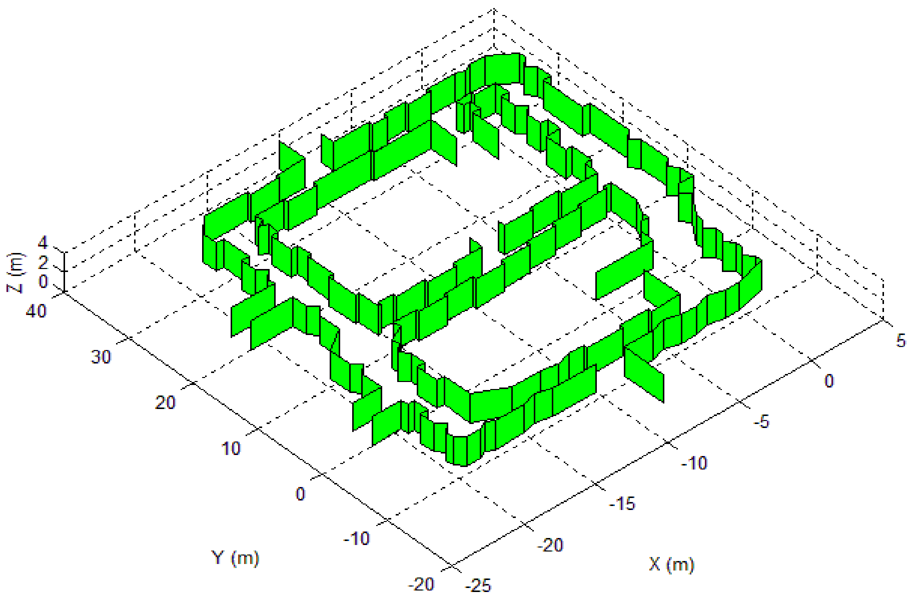

Figure 4.10: Simulated structured environment using rectangles.

4.3.2.
LRF Simulation

The working principle of the LRF, also known as a LIDAR, is shown in Figure 4.11. In the presented simulation, laser ray data are assumed 1° apart, from

-90° to 90°. Note that these values are adjustable parameters in the simulator, which can vary depending on the simulated LRF model.

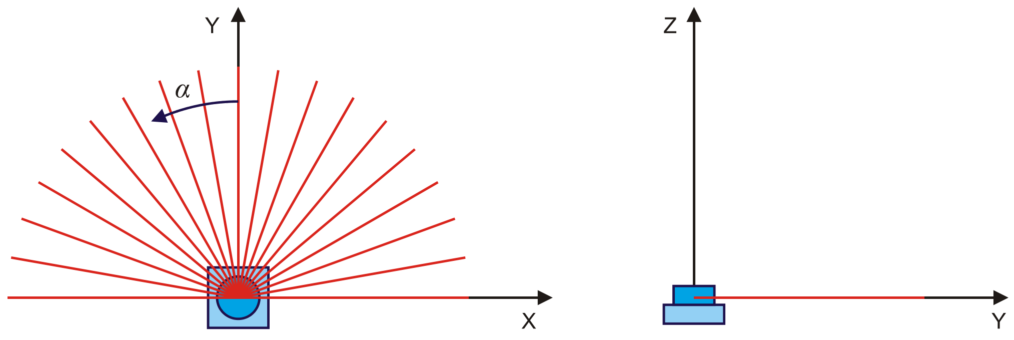

Figure 4.11: Laser ray from a simulated LRF.

Other adjustable parameters from the simulator are shown in Table 4.3.

Table 4.3: Adjustable parameters on simulated LRF.

Parameter	**Units**
Field of view	± rad
Operating range	m
Angular resolution	rad
Statistical Error	± mm, ±%, stdv (mm)

To acquire 3D data, the simulated LRF can be routed along its axis *X*, from 0° to 90° as shown in Figure 4.12, emulating a rotational support for the 2D LRF.

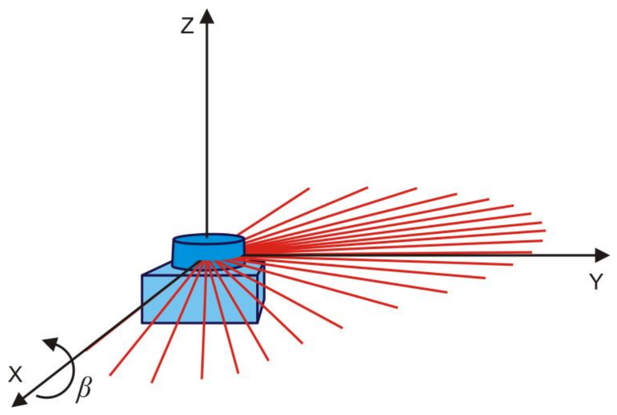

Figure 4.12: Simulated LRF rotation to acquire 3D data

Each measured laser ray is modeled as a vector in the polar system (*r, α, β*), with the origin as the point where the rays come from, where *r* represents the measured range, the rotation in the *Z* axis is given by *α*, and the rotation in *X* is given by *β*.

Simulated measurements are obtained by merging the simulated LRF routines with the models of the simulated environment. The point that defines the position of the LRF in the environment is the same point where the rays come from. Thus, the position and rotation of the LRF (in the environment and therefore in a global coordinate system) is given by four variables: *x, y, z* and *θ*, where *θ* is the rotation on an axis parallel to the Z axis of the global coordinate system.

With the LRF's rays and its position and rotation in the global coordinate system, the equation for each ray vector is constructed. Using the two points (***a*** and ***b***) that define a ray vector, the line equation in 3D is given by

$$\frac{(x-a_x)}{c_x} = \frac{(y-a_y)}{c_y} = \frac{(z-a_z)}{c_z} \tag{4.40}$$

where

$$\begin{bmatrix} c_x \\ c_y \\ c_z \end{bmatrix} = (\boldsymbol{b}-\boldsymbol{a}) = \left(\begin{bmatrix} b_x \\ b_y \\ b_z \end{bmatrix} - \begin{bmatrix} a_x \\ a_y \\ a_z \end{bmatrix} \right) \tag{4.41}$$

Finally, virtual data is acquired equating the line equation (of each ray vector) and the plane equation (of each plane), solving it to find the intersection points, and then computing the distances r, between these points and the LRF.

Figure 4.13 and Figure 4.14 show a scan where the position of the virtual LRF sensor is $x = 2.0$, $y = 12.3$, $z = 0.4$ and $\theta = 30°$ while the angle α ranges from -90° to 90° (181 rays), with a constant angle $\beta = 10°$.

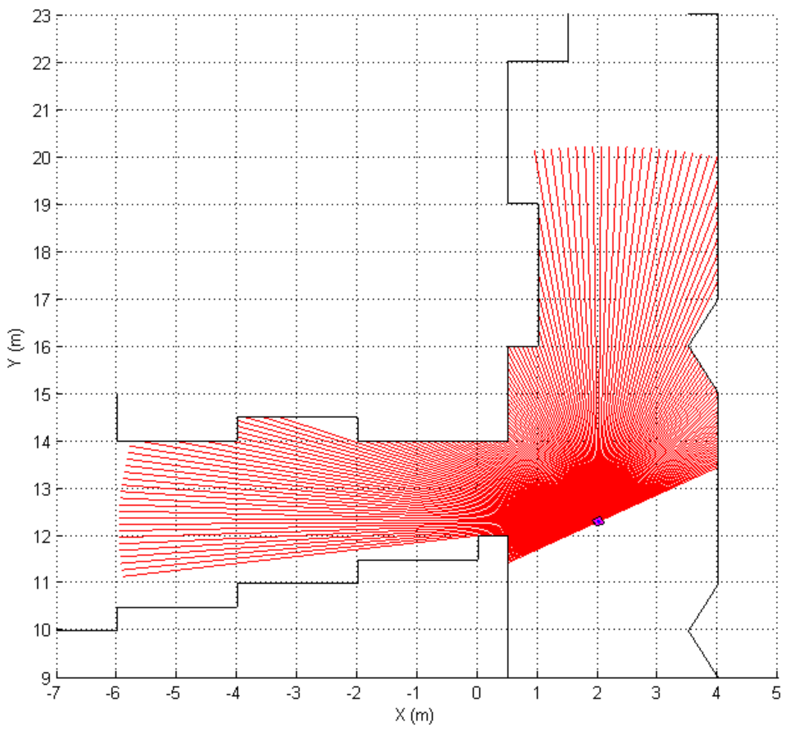

Figure 4.13: Virtual LRF readings in a simulated environment (top view).

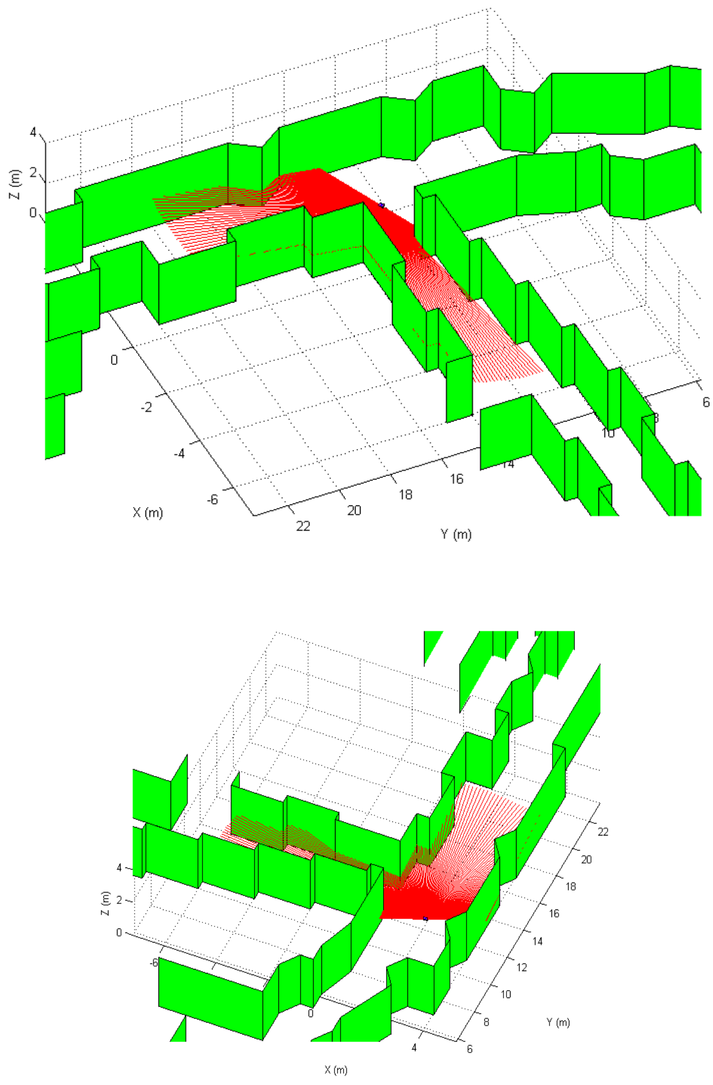

Figure 4.14: Virtual LRF readings in a simulated environment, from two different points of view.

4.3.3. Error introduction in virtual data

The LRF suffers from two types of errors: systematic and statistical. Systematic error can be reduced to acceptable limits by a good calibration or replacing the faulty sensor. However statistical errors are always present in the measurements. Thus for LRFs, each manufacturer gives in general the following three ways to represent the statistical error:

- **By standard deviation**. The standard deviations (stdv) of the measurements are given. For example the LRF SICK, model LMS200, has a stdv of 5mm, and the model LMS291 has a stdv of 10mm.
- **By a percentage of the measurement or by a fixed number**. For instance, the LRF SICK, model LMS291-S05 has an error of +/- 10mm.
- **By a fixed number until a certain range, and beyond that by a percentage**. For instance, the LRF HOKUYO, model URG-04LX, has an error of +/- 10mm in the range from 0 to 1m and, beyond that, 1% of the measurement. The model URG-04LX-UG01 has an error of +/- 30mm in the range from 0 to 1m and beyond that, 3% of the measurement.

These ways of expressing the error can be simulated and introduced in the distances *r*, virtually measured from the presented simulator.

The above presented simulator description just focused in its basic functionalities, however there are innumerable improvements that can be made, especially regarding the performance in time response. Solving equations for many planes/rectangles and lines is computationally expensive. Reference [30] a simulated 3D laser measurement system is presented, based on LMS SICK 200 mounted on a rotational platform. This simulator uses multi core processing power to generate 3D data. In [31] a simulator for airborne altimetric LIDAR is presented. This simulator is conceived having three components: terrain component, sensor component and platform component.

4.4. Scan Matching

One of the objectives of this work is to map an environment without using odometry information. Thus, the unique available information is taken from the scans made by the Laser Range Finder (LRF). To estimate the robot movement, the alignment of two consecutive scans needs to be performed.

It is important to notice that the scan matching searches for the displacement between two consecutive scans, but this displacement is not necessarily the robot displacement, since LRF may be mounted away from the robot center. To calculate the robot movement it is necessary to know where the LRF is situated on the robot, specifically where the LRF is located with respect to the coordinate system of the robot**.**

As described in Section 2.3.3, the scan matching method used in this work is the Normal Distribution Transform (NDT). This method was selected basically because it has a featureless representation of the environment, consequently it doesn’t need search for correspondences in the scans.

NDT uses Newton´s algorithm to minimize the function $\boldsymbol{f} = -score$. In most systems, the initial estimate of the solution is given by odometry information. But large error in the initial position estimate can contribute to the non-convergence of the algorithm.

Therefore, to generate a robust algorithm, in this work a Genetic Algorithm (GA) is used for optimization, from the Differential Evolution routines described in Section 2.4.5.

4.4.1. Differential Evolution Optimization for NDT

First, let’s rewrite eq. (2.15)

$$score(\boldsymbol{p}) = \sum_i \exp\left(-\frac{(x_i' - q_i)^{\mathrm{T}} \Sigma_{\mathrm{i}}^{-1} (x_i' - q_i)}{2} \right) \tag{4.42}$$

The outline of this optimization, given two scans (the *first* and the *second* one), is as follows:

1. Build the NDT of the *first* scan, as described in Section 2.3.3.
2. Use the *first* scan to evaluate the distribution of its points using eq. (4.42). This means that the vector of parameters must be $\boldsymbol{p} = [0\ 0\ 0]^T$ and the *score*(***p***) will give a value that is the maximum possible. This is,

because the same scan is used to build the NDT and to evaluate the score. Let's call this maximum value ***A***.

3. Filter the *second* scan, in order to eliminate regions with high density readings (this will be explained in Section 4.4.3).
4. Initialize the ED algorithm, giving it the filtered *second* scan and the function ***A***–*score*(***p***) as the fitness function. That is, ED should minimize this function, estimating the vector ***p*** and evaluating the filtered *second* scan into the NDT of the *first* scan.

The use of ED is robust and useful to estimate the vector ***p***, which in this 2D case is composed by the translation (Δx, Δy) and rotation ($\Delta\theta$) between scans. This tree displacement values are the variables to be codified; thus, one chromosome is composed as:

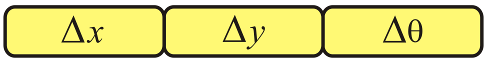

Figure 4.15: Chromosome composition

and are represented by real numbers. The fitness function, as exposed above, is given by:

$$Fitness = \boldsymbol{A} - \sum_i \exp\left(- \frac{(\boldsymbol{x}_i' - \boldsymbol{q}_i)^T \Sigma_i^{-1} (\boldsymbol{x}_i' - \boldsymbol{q}_i)}{2} \right) \qquad (4.43)$$

- **The Stopping Criterion**

The stopping criterion used in this optimization is given by two values. The first is the Fitness value; thus, the optimizations stops if the fitness values is less than 1.0 (this value was acquired empirically). The second stopping criterion is the number of generations, established in 50 generations; although this criterion value is varied for analysis purposes in Section 5.1.1.

- **The Search Space**

Looking up in real data, references [32] and [33], most robot displacements are in its face direction; lateral movements are minimal because they are due to sliding. Another behavior in robots movements is that backward displacements are few and short. Thus, the search space for the three variables in the estimated vector p is:

Table 4.4: Search space for vector ***p***

Variable	Min value	Max value
Δx	-0.25 m	0.25 m
Δy	-0.50 m	1.00 m
$\Delta \theta$	-20.00 °	20.00 °

In this way, the translation and rotation between two scans is limited by this search space. These values were empirically defined such that they guarantee enough similar information in two consecutive scans in order to mach them.

This search space and the LRF's scanning frequency (which will be discussed later) therefore might limit the maximum lineal and angular velocity of the robot. However, the LRF's scans are sufficiently fast for most achievable robot speeds for non-airborne systems. Therefore, the search space plays a minor role in limiting the robot speed.

- **DE Parameters**

The following parameters used in DE for scan matching optimization were empirically acquired.

Table 4.5: DE Optimization Parameters.

Parameter	Value
Population size (*NP*)	100
Number of generations	50
Scaling Factor (*F*)	1.00
Crossover constant (*CR*)	0.95

Some consideration should be taken into account before using this ED optimization, as explained next.

4.4.2. Parameters and Considerations

a. Environment considerations

The environment to be mapped needs variety. E.g. long corridors without doors or any wall-shape variations will lead to poor scan matching performance, the ED will result in an estimated vector $\boldsymbol{p} = [0\ 0\ 0]$. How long these corridors can be without compromising scan matching depends on the LRF's maximum range, e.g., if the LRF's range is 8m, then the length of such corridor should be less than this value. But note that there are LRFs such as SICKs that have more than 50 meters in range.

In the same way, the width of these corridors should be less than LRF's range, to ensure that the robot will pickup data from both sides (left and right) of the sensor position.

b. LRF Considerations

Perhaps the most known LRF in Robotic is the SICK. SICK has a set of LRFs for many applications, and the most popular being the family of

LMS-200. Thus, for example, the SICK LMS-200-3016 model has the following main features [35]:

Table 4.6: SICK LMS-200-3016 features.

Field of view	180 °	
Scanning Frequency	75 Hz	
Operating range	0 m … 80 m	
Angular resolution	0.25° , 0.5°, 1.0°	
Systematic Error	+/- 15mm	
Statistical Error	+/- 5mm	

The scanning frequency of the above SICK is 75Hz, meaning 13.33 ms per scan. Thus with such data, it is possible to calculate the maximum linear and angular velocity of the LRF in order to guarantee that the movement of the robot does not affect the LRF's readings.

The following simplified equations could help to estimate these maximum speed as a function of the LRF's scanning frequency.

$$v_{\max} = \varepsilon_t * f_s \tag{4.44}$$

$$\omega_{\max} = \varepsilon_r * f_s \tag{4.45}$$

where f_s is the scanning frequency of the LRF, and the parameters ε_t and ε_r are the maximum error introduced by the robot's movement into the scan readings. For example, if the desired error must be at most 5mm in translation, and the scanning frequency of the LRF is 75 Hz, then the maximum speed of the LRF is $\boldsymbol{v}_{max} = 0.375$ m/s, while for a desired error of up to 0.25° in rotation, then $\boldsymbol{w}_{max} = 0.327$ rad/s.

Note that this maximum values in translation are referred to LRF speeds, which are not necessarily the same as the robot speed, depending on where the LRF is mounted on the robot and if the robot is making a turn.

4.4.3. Scan Filtering

The value of eq. (4.42) is influenced by the density of the readings. Regions with higher reading density are produced when the robot is close to a wall, thus eq. (4.42) results in higher values in this regions, see Figure 4.16. This situation is not desirable, as seen in [35]. The ED optimization could give us mismatched scans, as Figure 4.17, since such oversampling in one small region could negatively affect the matching of regions further away.

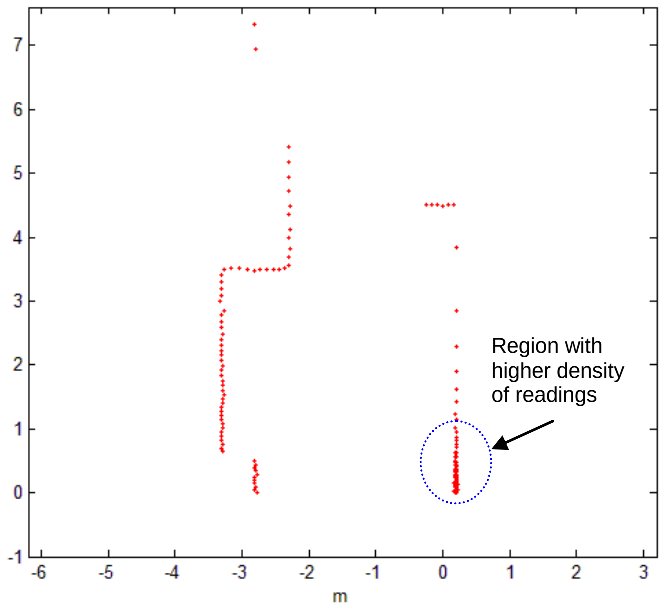

Figure 4.16: Density regions produced by a robot situated close to the right wall.

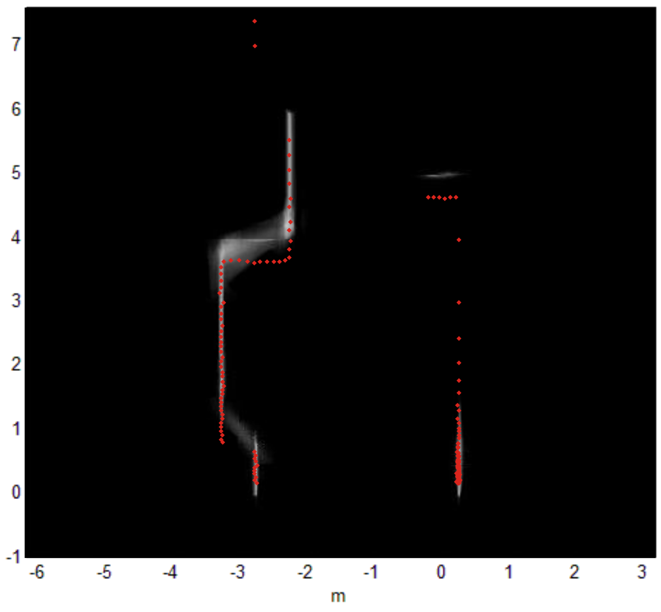

Figure 4.17: Mismatched scans, showing the NDT of a *first scan* (grayscale) and a *second scan* (red dots). The right-bottom wall produces a high number of readings, bringing down the second scan and compromising the match.

To overcome this situation this work uses the approach used by [36], replacing small clouds of close points by their center of gravity. This has the effect of smoothing the distribution of points over the scan. It also greatly reduces the number of scan points, without loosing too much information.

The idea behind this filter is to move a circular window with fixed radius over the scan and to replace the readings inside the window with their center of gravity. The radius of the window defines the minimum distance between the points in the filtered scan. This radius has to be defined experimentally. Low values for this parameter do not solve the influence of the readings density, while high values may render the resulting scan too sparse. In this work, this parameter is set to 10 cm.

Figure 4.18 shows the same scan points of Figure 4.16, before filtering (left) and after filtering (right). Reducing the number of scan points also improves the speed of the ED optimization.

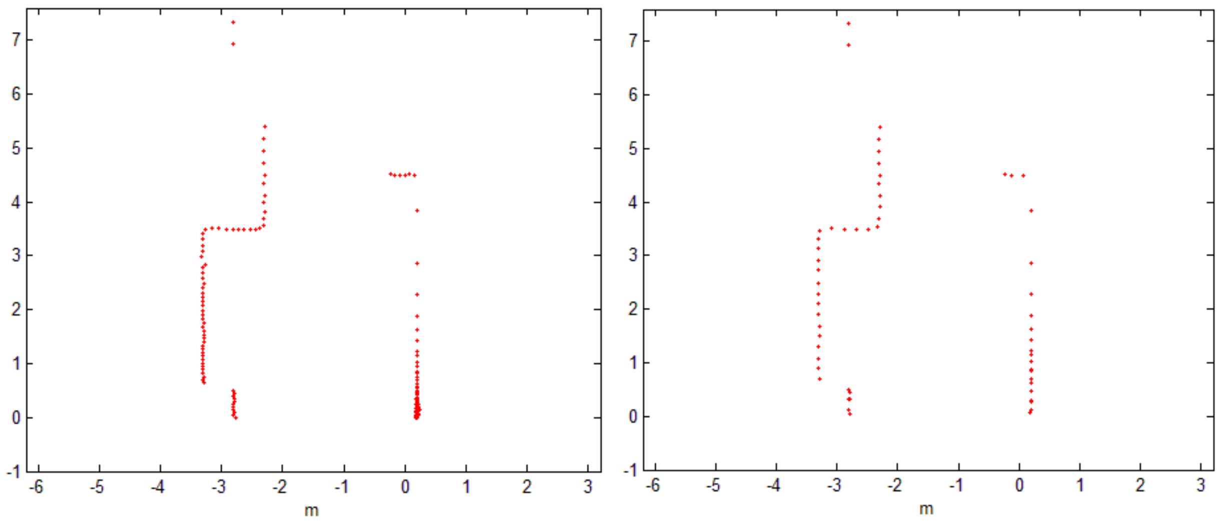

Figure 4.18: Scan filtering. Original scan with 181 points (left) and filtered scan with 59 points (right).

4.5. DP-SLAM

The DP-SLAM algorithm is presented in this work in the form of flowcharts. The detailed implementation of DP-SLAM is too extensive to be presented here. However the code used in this work is free, available to download from [33]. This code was modified in this work to include scan matching as a motion model, as explained later.

As explained in Section 3.2.3, DP-SLAM uses a hierarchical algorithm. The relationships between the low and high levels are shown in Figure 4.19. Here, the input data is composed by the odometry and the range scans. Thus, each position, estimated by the odometry reading, has attached its range scan. A piece of data is used as input to low level SLAM. The output is the best estimated trajectory attached with its corresponding range scans.

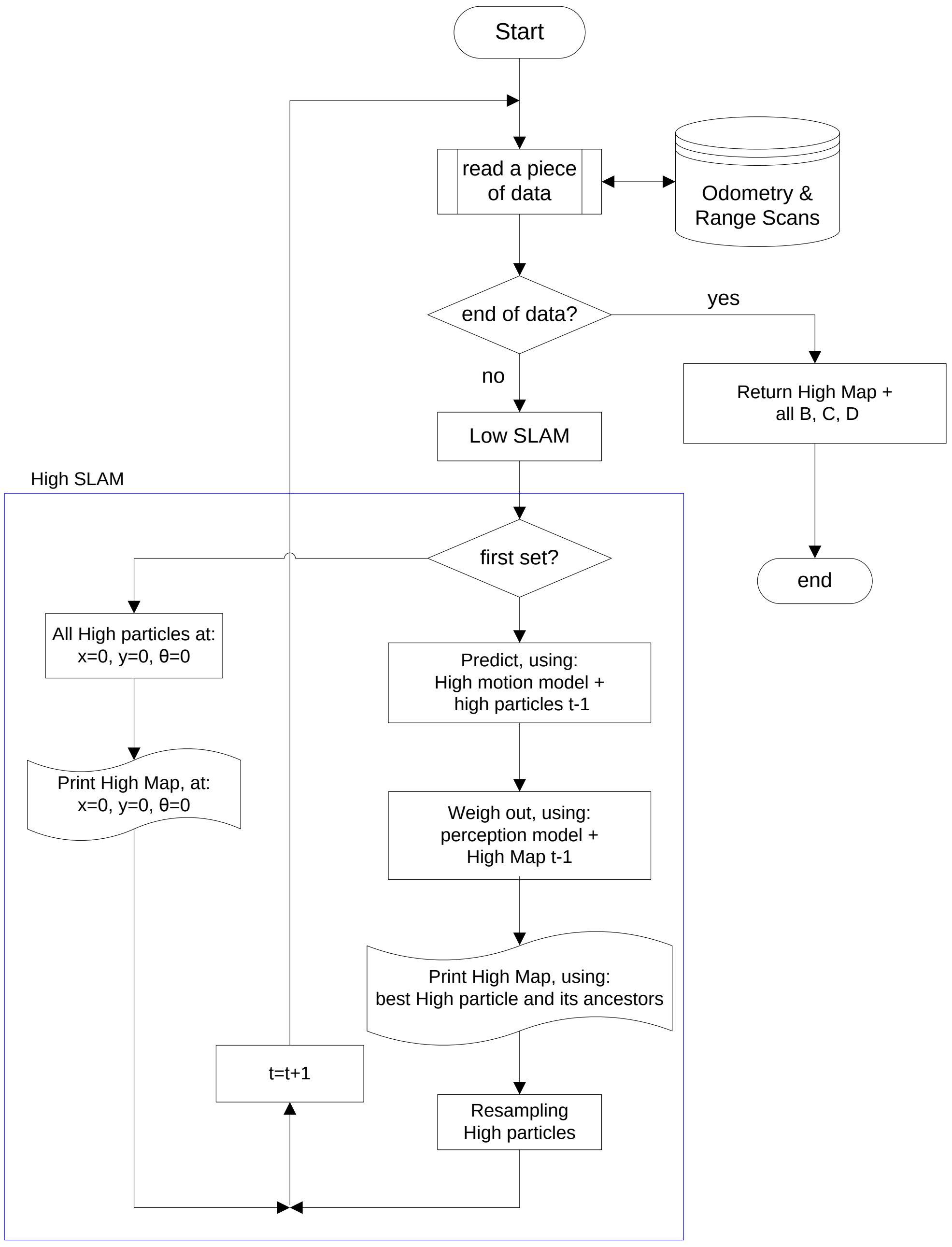
Start
read a piece of data
Odometry & Range Scans
end of data?
yes
no
Return High Map + all B, C, D
Low SLAM
end
High SLAM
first set?
All High particles at: x=0, y=0, θ=0
Predict, using: High motion model + high particles t-1
Print High Map, at: x=0, y=0, θ=0
Weigh out, using: perception model + High Map t-1
Print High Map, using: best High particle and its ancestors
t=t+1
Resampling High particles

Figure 4.19: DP-SLAM flow chart

Figure 4.20 shows the low SLAM flowchart. Notice that, in the beginning, all los particles are located in an initial position, and using the firs data scan a low-map is printed. This initial position and low-map is used by the subsequent *t+1* iteration.

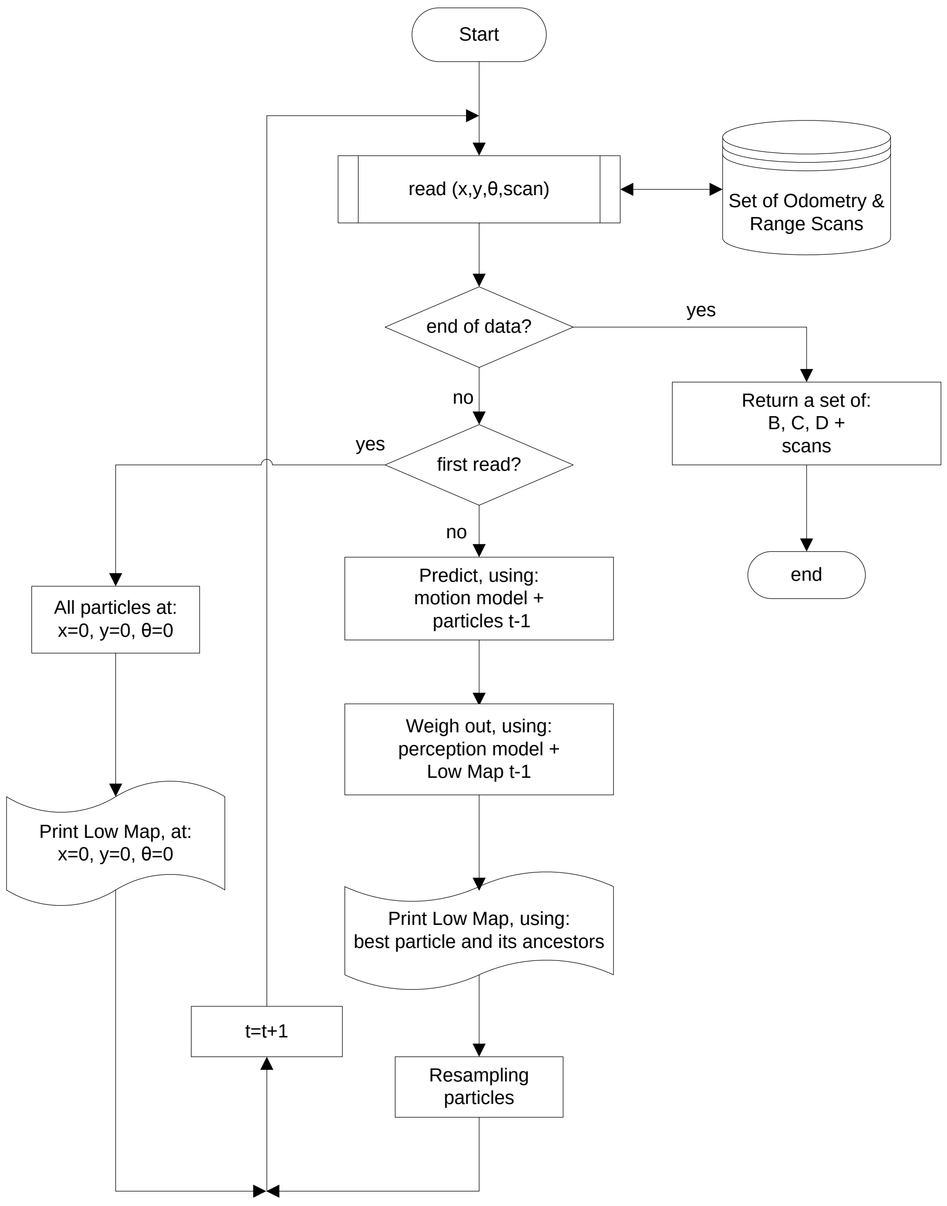
Start
read (x,y,θ,scan)
Set of Odometry & Range Scans
end of data?
yes
no
Return a set of: B, C, D + scans
end
yes
first read?
no
Predict, using: motion model + particles t-1
All particles at: x=0, y=0, θ=0
Weigh out, using: perception model + Low Map t-1
Print Low Map, at: x=0, y=0, θ=0
Print Low Map, using: best particle and its ancestors
t=t+1
Resampling particles

Figure 4.20: Low (level) DP-SLAM flow chart

As show in Section 3.2.3, DP-SALAM uses a particle filter to track the robot position. Thus the motion model is used to predict (i.e. generate samples) and the perception model is used for particles weighing. A low-map is printed each iteration, using the best particle and its ancestors. Note that the best particle at iteration *t*, may not be a child of the best particle at iteration *t–1*.

The output of the Low SLAM (LSLAM) is used by the High SLAM (HSLAM), as shown in the Figure 4.19. Note that HSLAM is slightly similar to LSLAM, but instead of sampling robot positions, HSLAM samples robot trajectories. Also both low an high, use the same perception model, but their laser variances are different. The LSLAM is the basic SLAM algorithm, working unperturbed while the HSLAM is working with slightly different data and as such, requires a different laser noise model. With a “rigid” trajectory passed up from the LSLAM, there is less room for minor perturbations, and certain amount of assumed drift. All of this is included in the high level laser variance, which needs to be correspondingly larger [6]. Empirical results show that using a standard deviation of 7cm at the higher level works well [6].

Finally the High SLAM output is the best High Map and robot path.

4.5.1.
Motion Model

The motion model proposed by Eliazar [6], is shown in eq. (4.46).

$$\begin{bmatrix} R^i x_t \\ R^i y_t \\ R^i \theta_t \end{bmatrix} = \begin{bmatrix} R^i x_{t-1} + D\cos(R^i\theta_{t-1} + B/2) + C\cos(R^i\theta_{t-1} + (B+\pi)/2) \\ R^i y_{t-1} + D\sin(R^i\theta_{t-1} + B/2) + C\sin(R^i\theta_{t-1} + (B+\pi)/2) \\ R^i\theta_{t-1} + B \end{bmatrix} \tag{4.46}$$

The new position R_t=[Rx_t , Ry_t , $R\theta_t$] depends on the last robot position R_{t-1} and the parameters *B*, *C* and *D*. The value ($R\theta_{t-1}$ + *B/2*) is called the major axis movement, and both *B* and *D* are expected to be distributed normally distributed with respect to the reported odometry values *b* and *d* (amount of rotational and translational movement, respectively). But the mean of each *B* and *D* will scale linearly with both *b* and *d*, while the variance will scale with b^2 and d^2. *C* is an extra lateral translation term, which is present to model shift in the orthogonal direction of the major axis. This axis, called minor axis, is at angle ($R\theta_{t-1}$ + *(B+π)/2*). In this view, *B*, *C* and *D* are all conditionally Gaussian given *b* and *d*:

$$\begin{aligned} B &\sim \mathcal{N}(d\mu_{Bd} + b\mu_{Bb}, d^2\sigma^2_{Bd} + b^2\sigma^2_{Bb}) \\ C &\sim \mathcal{N}(d\mu_{Cd} + b\mu_{Cb}, d^2\sigma^2_{Cd} + b^2\sigma^2_{Cb}) \\ D &\sim \mathcal{N}(d\mu_{Dd} + b\mu_{Db}, d^2\sigma^2_{Dd} + b^2\sigma^2_{Db}) \end{aligned}$$

where μ_{Ax} is the coefficient for the contribution of the odometry term x to the mean of the distribution over A. DP-SLAM uses an automatic parameter estimator to obtain these μ_{Ax}.

Note that the above implementations assume that odometry readings are available. This work, on the other hand, does not make use of odometry information. This is obtained instead from scan matching. In this way, the “scan odometry” consist of tree displacements: Δx, Δy, $\Delta\theta$, displacements that are referenced to the current robot position. Because scan matching is used, no extra lateral displacement needs to be considered. In the implemented approach, two consecutive scans are taken from two different points in the environment, as shown in Figure 4.21.

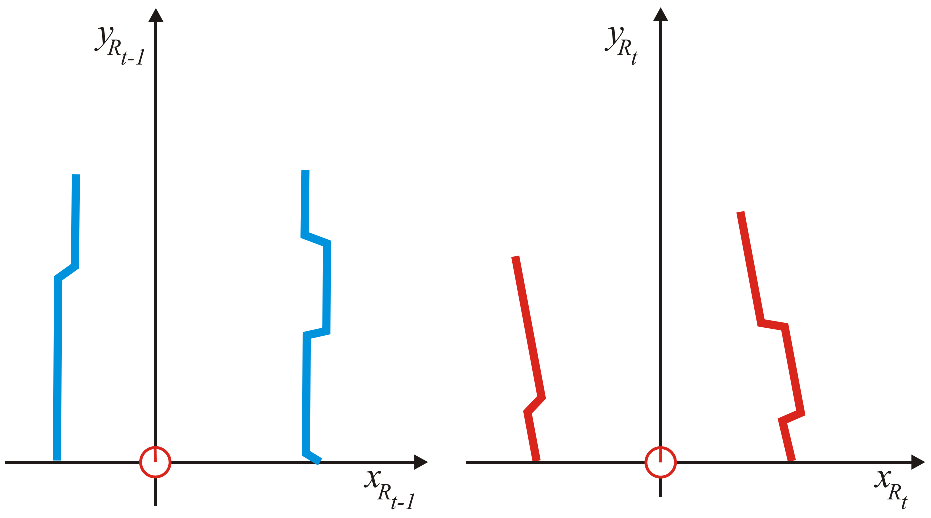

Figure 4.22 (left) shows the environment from the first, or current, robot position point of view, and (right) shows it from the second robot position.

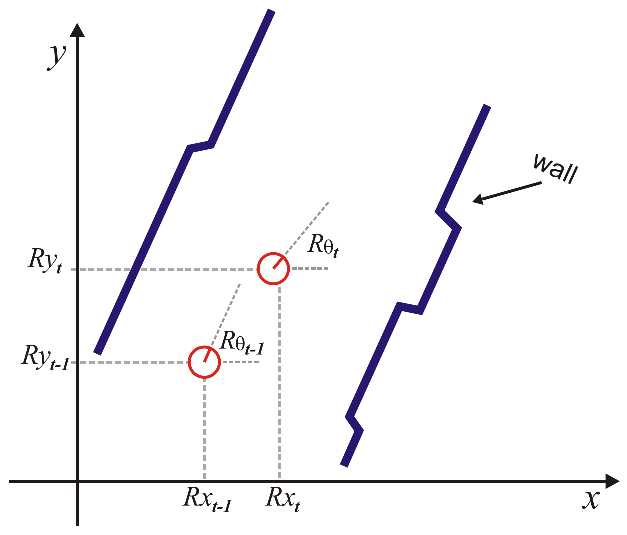

Figure 4.21: Two consecutive robot positions in an environment.

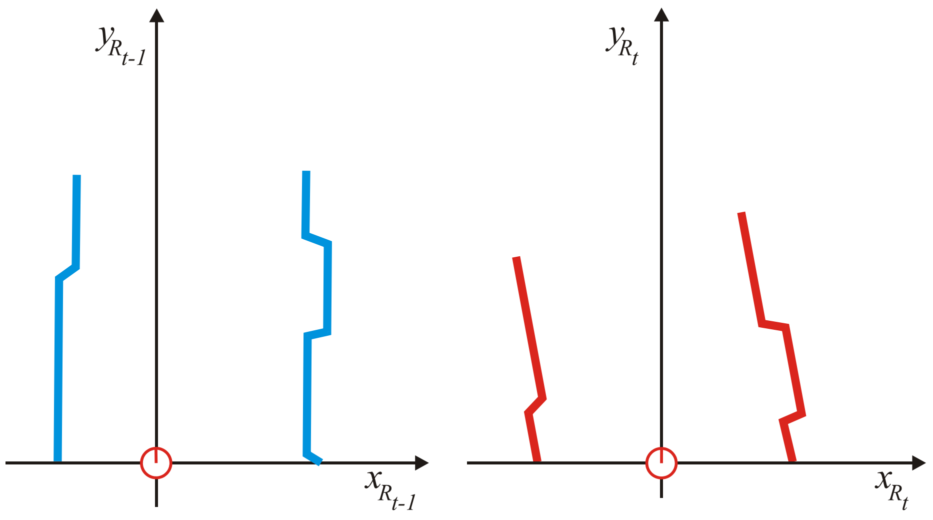

Figure 4.22: Environment seen from the current robot position (left) and second robot position (right).

Thus, the scan matching process searches for an alignment of both scans, by rotating and translating the second scan onto the first scan coordinate system, to obtain the actual robot displacements Δx, Δy, $\Delta \theta$. The aligned scans are shown in Figure 4.23.

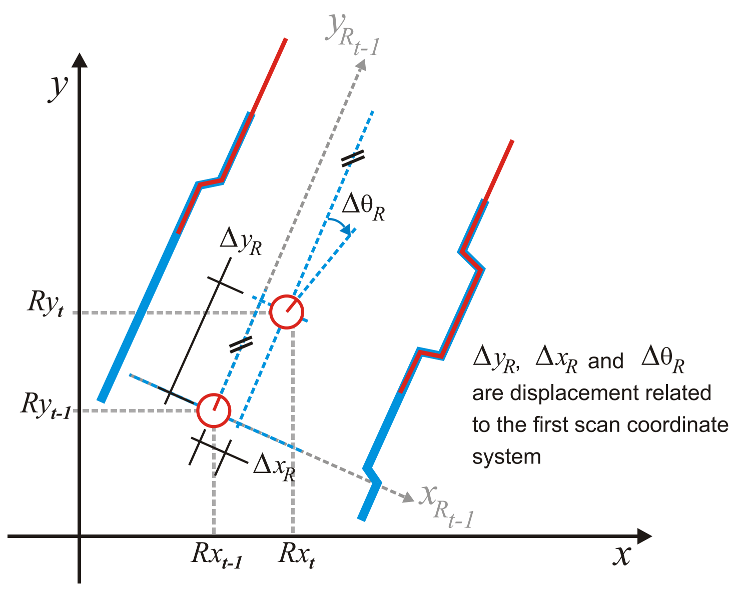
$y_{R_{t-1}}$
y
$\Delta\theta_R$
Δy_R
Ry_t
Ry_{t-1}
Δx_R
$x_{R_{t-1}}$
Rx_{t-1}
Rx_t
x
Δy_R, Δx_R and $\Delta\theta_R$ are displacement related to the first scan coordinate system

Figure 4.23: Aligned scans in a global coordinate system, displacements Δy_R, Δx_R and $\Delta\theta_R$ are related to the first scan coordinate system.

Assuming a perfect scan matching, eq. (4.47) gives the new robot position by

$$\begin{bmatrix} R^i x_t \\ R^i y_t \\ R^i \theta_t \end{bmatrix} = \begin{bmatrix} R^i x_{t-1} + d\cos(\alpha) \\ R^i y_{t-1} + d\sin(\alpha) \\ R^i \theta_{t-1} + \Delta\theta \end{bmatrix} \tag{4.47}$$

where:

$$d = \sqrt{(\Delta x)^2 + (\Delta y)^2} \quad \text{and} \quad \alpha = R^i\theta_{t-1} - \pi/2 + \operatorname{atan2}(\Delta y, \Delta x)$$

However, because the scan matching process isn't perfect, it will give us an approximation of Δx, Δy, and $\Delta\theta$. It is expected that these approximations are distributed according to a distribution shape. The shape of this distribution must be acquired empirically by comparing the approximated displacement, after convergence of the scan matching, with actual position (estimated or simulated), as explained in Chapter 5. Table 4.7 shows an algorithm to sample from this scan matching motion model, $(R_t | u_t, R_{t-1})$, to generate a random poses R_t^i. Lines 1 through 3 perturb the "scan odometry" parameters with noise, drawn from the error parameters v_x, v_y and v_θ (they will be explained in Chapter 5). The noise values are then used to generate the new sample pose in lines 4 through 8. of the algorithm.

Table 4.7: Sample scan matching motion model algorithm, where atan2(Δy, Δx) is defined as the generalization of the arc-tangent function of $\Delta y/\Delta x$ over [0, 2π].

```
Sample SM Motion Model algorithm ($R_{t-1}, u_t$)
1:    $\Delta\hat{x} = \Delta x + sample(v_x)$
2:    $\Delta\hat{y} = \Delta y + sample(v_y)$
3:    $\Delta\hat{\theta} = \Delta\theta + sample(v_\theta)$
4:    $d = \sqrt{(\Delta\hat{x})^2 + (\Delta\hat{y})^2}$
5:    $\alpha = R\theta_{t-1} - \pi/2 + \mathrm{atan2}(\Delta\hat{y}, \Delta\hat{x})$
6:    $Rx_t = Rx_{t-1} + d\cos(\alpha)$
7:    $Ry_t = Ry_{t-1} + d\sin(\alpha)$
8:    $R\theta_t = R\theta_{t-1} + \Delta\hat{\theta}$
9:    return $R_t = (Rx_t, Ry_t, R\theta_t)$
```

Finally, the LSLAM output in Figure 4.20, using the proposed motion model, is a set of changes between positions $\Delta\hat{x}$, $\Delta\hat{y}$, $\Delta\hat{z}$ and its corresponding range scans.

4.5.2. High Motion Model

As seen in Section 3.2.3.4, DP-SLAM states that the effects of drift on low level maps can be accurately approximated by perturbations to the endpoints of the robot trajectory used to construct a low level map.

By sampling drift only at endpoints, it will fail to sample some of the internal structure that is possible in drifts, e.g., it will fail to distinguish between a linear drift and a spiral drift pattern with the same endpoints. However, the existence of significant, complicated drift patterns within a map segment would violate the assumption of moderate accuracy and local consistency within the low level mapper [6].

The “motion” model in high SLAM is assumed to be Gaussian, and evenly distributed about the lateral axes. The specific values for these variances are highly mutable, affected by the specific SLAM algorithm used at the low level, and the amount of resources used, as well as elements from the robot or the environment [6].

Figure 4.24 shows how the high motion model works. As shown in Figure 4.19 the first set of data received from the low SLAM is simply printed in the high map at zero position. This is shown in the Figure 4.24, the first set of data is a set of variables $\Delta\hat{x}, \Delta\hat{y}, \Delta\hat{z}$, (represented by a red line) along with its scans (represented by the green region of the figure).

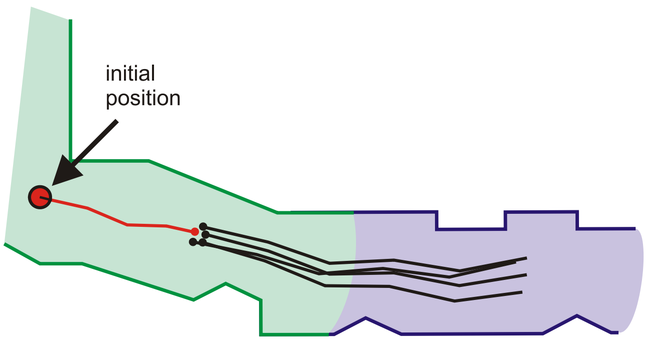

Figure 4.24: High Motion Model

The second set of data received from the low SLAM (black line) is not connected with the endpoint of the first set (red dot). Instead, it is linked with many samples (black dots), generated by applying the high motion model at the first endpoint (red dot). Notice, however, that Figure 4.24 shows the second set of scans (piece of map in blue color) only for one sample (the best sample); thus it is understood that high SLAM keeps a different map for each sample. Note that the motion model generates samples not only disturbing the endpoint position, but also the endpoint rotation.

In the next chapter the presented algorithms are evaluated, both using simulated data and real experimental data taken from the literature.

5. Tests and results

This chapter presents results obtained using the proposed method on simulated and real data. First, it is analyzed the scan matching optimization; after that, the Scan Matching Motion Model is detailed presented, then some 2D results are shown using DP-SLAM; and finally a simulated and a real 3D map example are presented.

5.1. Scan Matching

5.1.1. Optimization Parameters Influence

Because this analysis uses simulated data, the truth robot displacement values, Δx, Δy, $\Delta\theta$; are known exactly; this will help us to test the optimization parameters influence on the scan matching process.

As shown in Section 4.4.2, the optimization using genetic algorithm depends on the size of the population and the number of generations. The Figure 5.1 and Figure 5.2 present the error displacement obtained by scan matching, showing the population size influence in DE optimization (the number of generation is kept fixed, in this case *generations* = 50), this experiment has 366 simulated robot poses and were acquired by simulating an standard deviation error of 15 mm.

Notice that in Figure 5.1, small population leads to non-convergence and consequently the estimated displacement surfers from hug errors, as shown in this case for population size of 20 and 40.

In the other hand Figure 5.2, shows the same experiment using a larger population; here the peaks have been significantly reduced in size and number (see the scale).

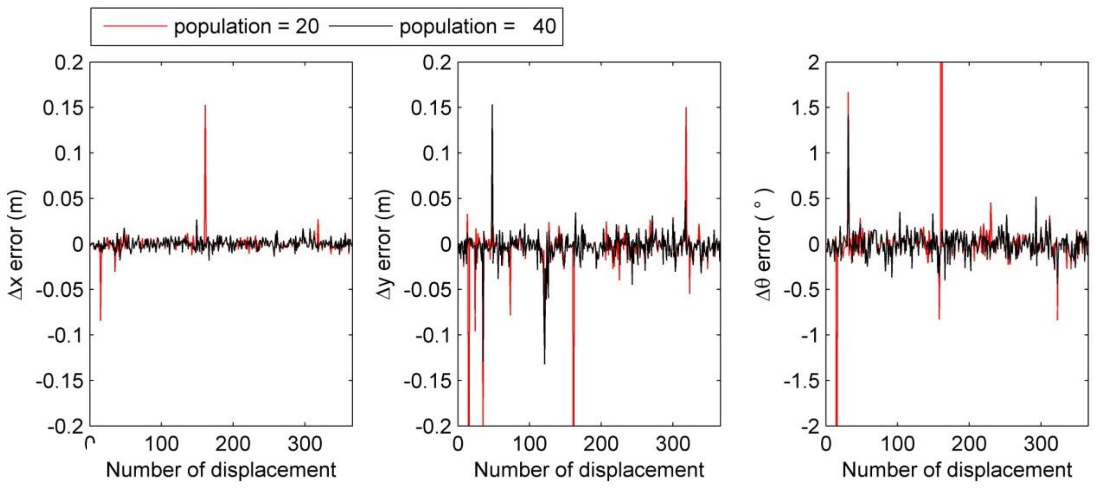

Figure 5.1: Error in displacement, Δx, Δy, $\Delta\theta$, influenced by population size (20 and 40) in DE optimization.

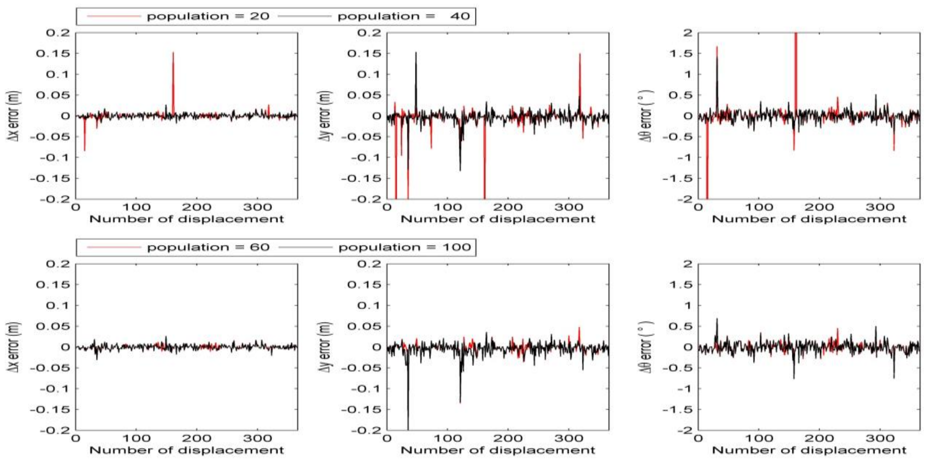

Figure 5.2: Error in displacement, Δx, Δy, $\Delta\theta$, influenced by population size (60 and 100) in DE optimization.

Figure 5.3 and Figure 5.4 show the error displacement, when the population size is fixed to 100 and the generation number is varied. The effect of generation increase is to improve the precision in displacement estimation. As seen in Figure 5.3 (for 15 and 30 generations), although convergence has been guaranteed, there are not enough generations to significantly improve the estimation.

On the other hand, Figure 5.4, shows a refined estimation by increasing the generation number (50 and 75 generations).

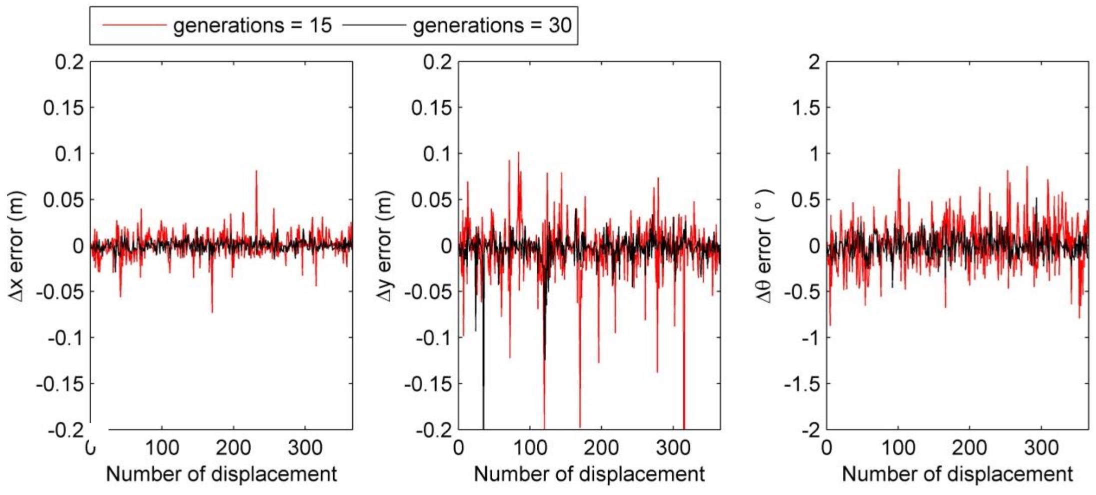

Figure 5.3: Error in displacement, Δx, Δy, $\Delta\theta$, influenced by number of generations (15 and 30) in DE optimization.

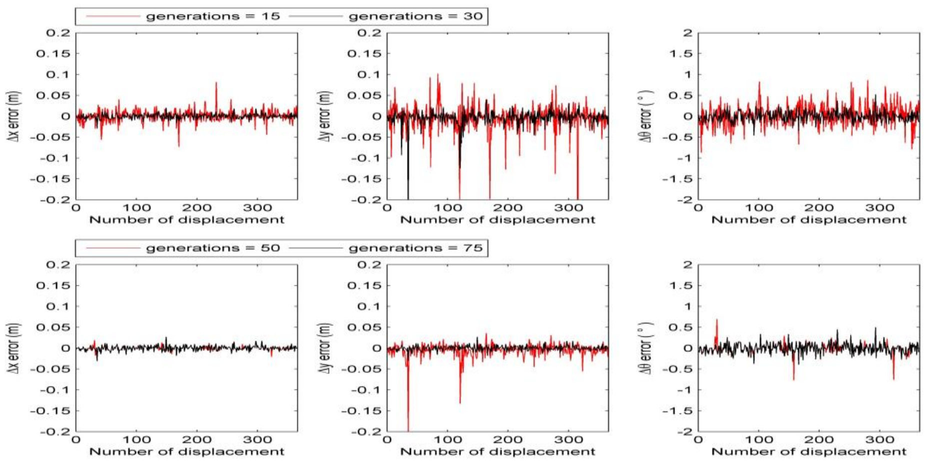

Figure 5.4: Error in displacement, Δx, Δy, $\Delta\theta$, influenced by number of generations (50 and 75) in DE optimization.

5.1.2. LRF Error Influence

Another important scan matching parameter is the LRF error. Using the same simulated environment and simulated robot poses, error in laser range is introduced by adding a random value picked from a Gaussian distribution with zero mean and a variable standard deviation (stdv). In this case, the standard deviations are between 15mm and 80mm.

Figure 5.5 and Figure 5.6 show the LRF error influence in DE optimization. This simulation uses a fixed population size, 100, and a fixed number of generations, 50, showing that the greater the laser range error the worse the estimated displacement. Note however that DE optimization is robust, even if the error displacements increase.

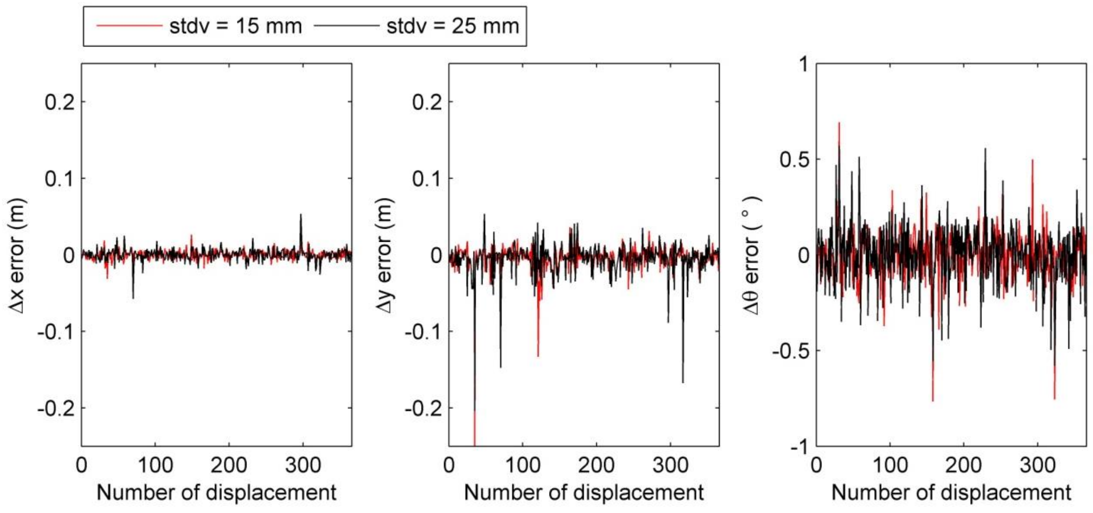

Figure 5.5: Displacement error, Δx, Δy, $\Delta\theta$, influenced by LRF error (stdv= 15mm and stdv=25mm) in DE optimization.

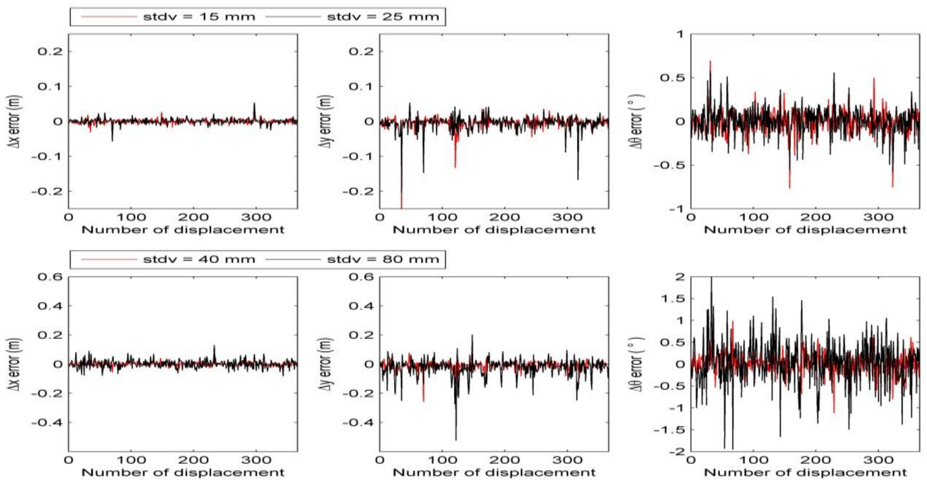

Figure 5.6: Displacement error, Δx, Δy, $\Delta\theta$, influenced by LRF error (stdv= 40mm and stdv=80mm) in DE optimization.

As explained in the introduction of this work, although technology offers increasingly accurate position sensors, even small measurement errors can accumulate and compromise the localization accuracy. This becomes evident when programming a robot to return to its original position after traveling a long distance, based only on its sensor readings. In this case, our position “sensor” is the scan matching process.

Figure 5.7 shows the accumulated error in robot position, where (robot poses are marked in capital letters according to Figure 5.8). This error represents the Euclidean distance between the estimated and true robot simulated robot position. Note that the error inevitably grows as the robot pose number increases.

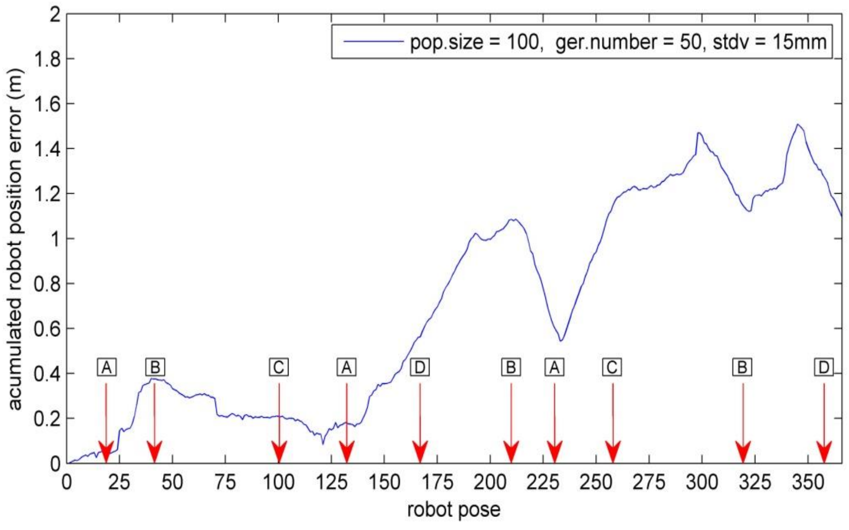

Figure 5.7: Accumulated error in robot position due to imperfect scan matching.

Figure 5.8 shows the simulated environment used for all theses scan matching experiments. It also shows the true (red line) and estimated (blue line) robot path acquired by scan matching. Figure 5.9 shows the map for the estimated robot path, showing the growing misalignments due to accumulated small errors in scan matching process.

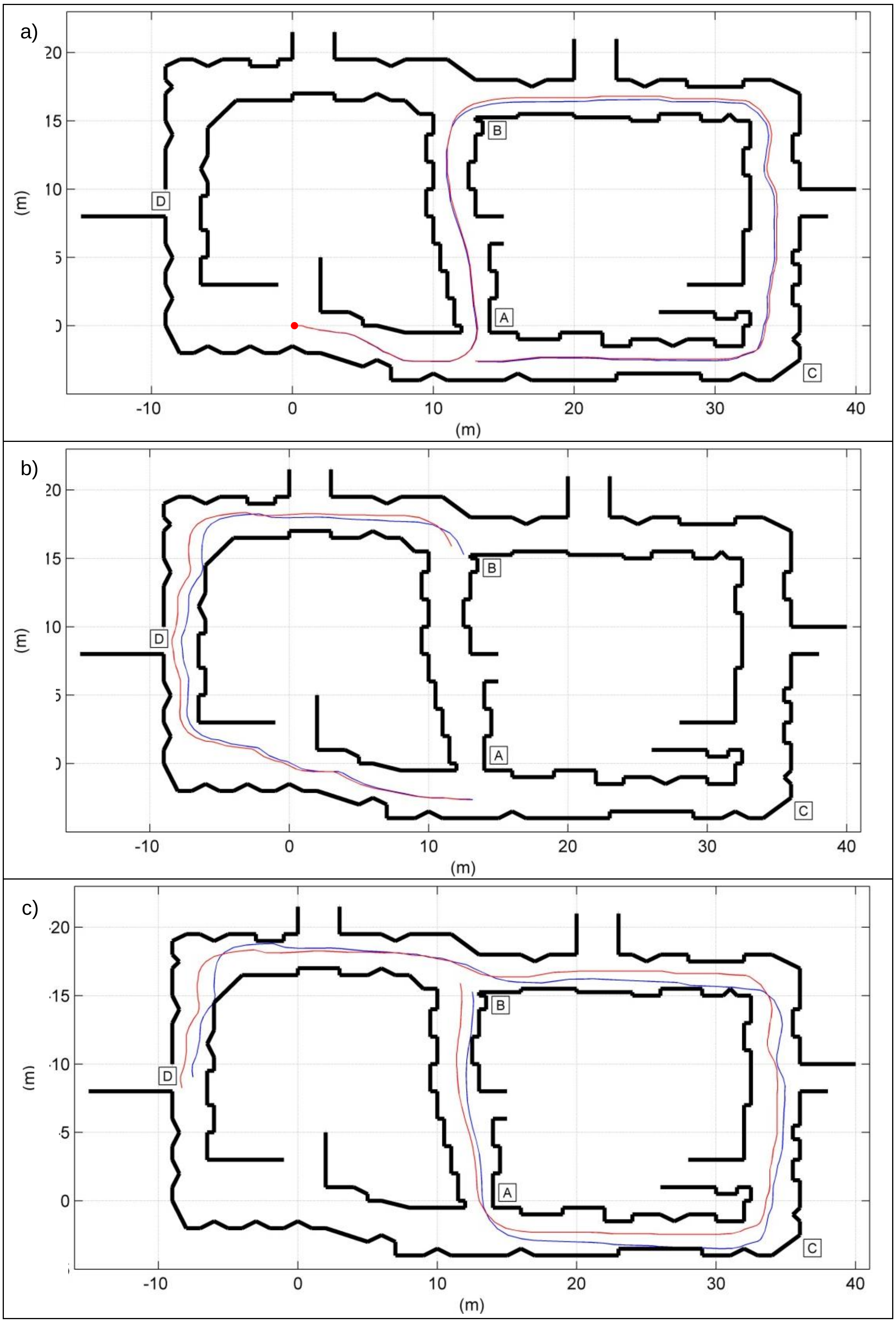

Figure 5.8: Robot trajectories, showing the true path (red line) and estimated path (blue line). a) Robot starts from zero position (red dot), goes through positions A, B, C and A. b) Robot traveling A, D, B. c) Robot completes the course through B, A, C, B and D.

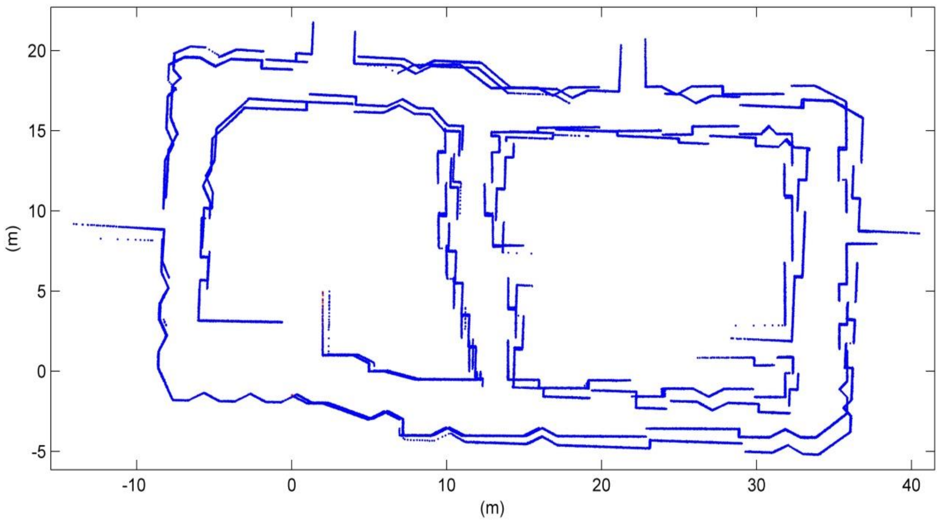

Figure 5.9: Map acquired using scan matching process in the simulated environment.

5.1.3. Scan Matching in Real Data

To analyze the proposed method using real experimental data, it is necessary to have the true robot position in the environment. But this would require expensive motion detector sensors and an external measurement, which are usually not available. Thus, in this work, the analysis made with real data collected from the literature focuses on the study of the convergence on DE optimization. As was seen in Section 4.4.1, the fitness function to minimize has been defined as ***A***-*score*(***p***), which should be close to zero for a good match.

The performance of the proposed method is evaluated with real data from four experiments from the literature.

The first experiment comes from the second floor of the Duke University Computer Science Department (the second floor of the D-Wing of the LSRC building) [32]. This contains 551 robot poses and uses a LRF with 8m maximum range. This data includes odometry information, which is removed to show the efficiency of the presented approach using a single LRF. Figure 5.10 shows the fitness function value for each of the 550 robot displacements, acquired using the proposed method. The fitness value will rarely be close to zero, because two consecutive will never be the same, unless the robot does not make any movement and the sensors didn't have uncertainties. The fitness values for "D-Wing" experiments show some peaks. Empirically, it is possible to state that values below 30 have a greater probability of convergence in DE optimization.

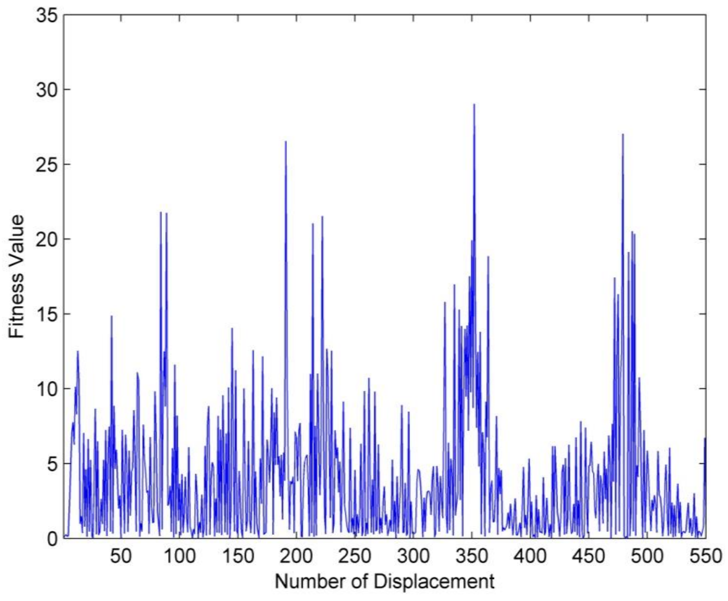

Figure 5.10: Fitness values for "D-Wing" experiment.

Since all fitness values are below 30, this experiment has a greater probability of not having non-convergence problems. This can be confirmed on the resulting map, shown in Figure 5.11. This figure shows the "D-Wing" experiment, which is a closed loop indoor structured environment. It can be observed also the resulting misalignment due to cumulative error in scan matching.

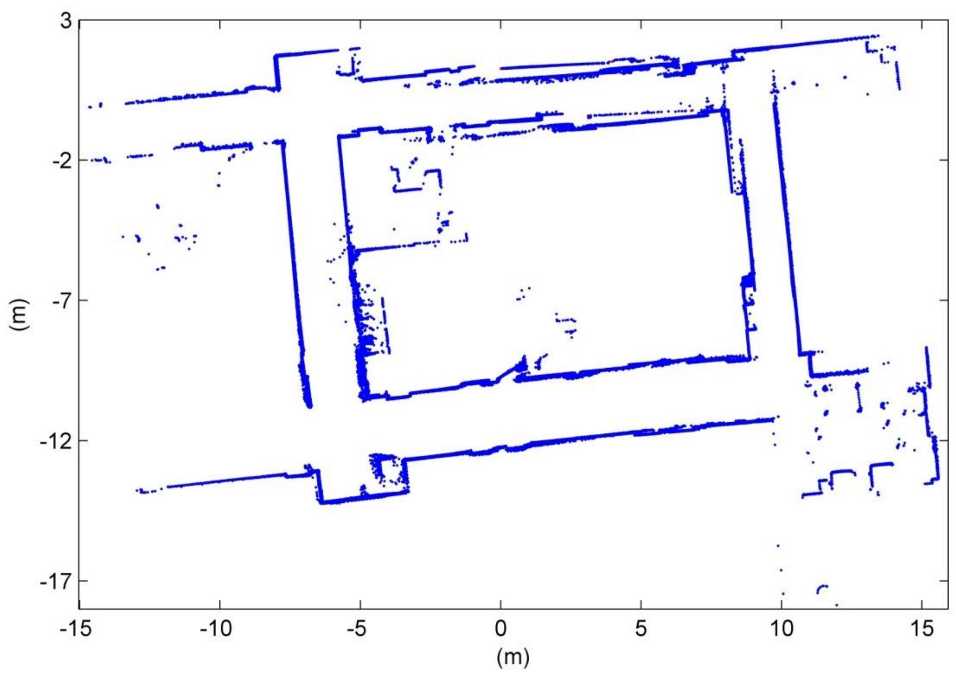

Figure 5.11: “D-Wing” experiment acquired using the proposed scan matching process, without the use of odometry data.

The second experiment also comes from the Duke University Computer Science Department, a long stretch of the second floor of the C-Wing of LSRC – pharmacology [32]. This contains 1,106 robot poses and uses a LRF with 8m maximum range. Once again the odometry data is removed for tow show that it is not needed in the SLAM process using the presented methods. Figure 5.12 shows the fitness function value for each of the 1105 robot displacements, acquired using the proposed method.

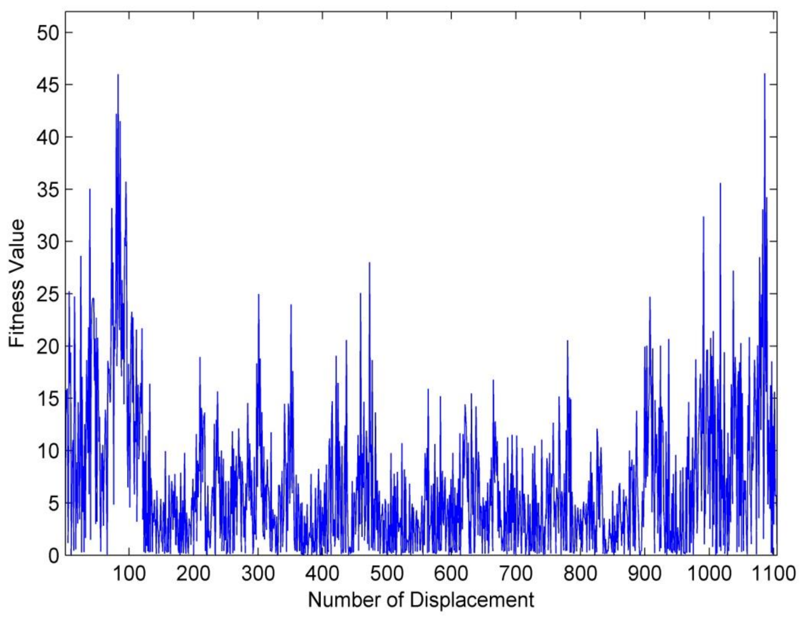

Figure 5.12: Fitness values for “C-Wing” experiment

This figure shows a few peaks (12 in total) larger than the empirically estimated threshold 30. They have a higher probability of resulting in non-convergence in DE optimization. To determine their convergence, they have to be inspected by simple observation.

Figure 5.13 shows the “C-Wing” experiment, which is also a loop closed indoor structured environment. Note also it the misalignment due to cumulative error in scan matching.

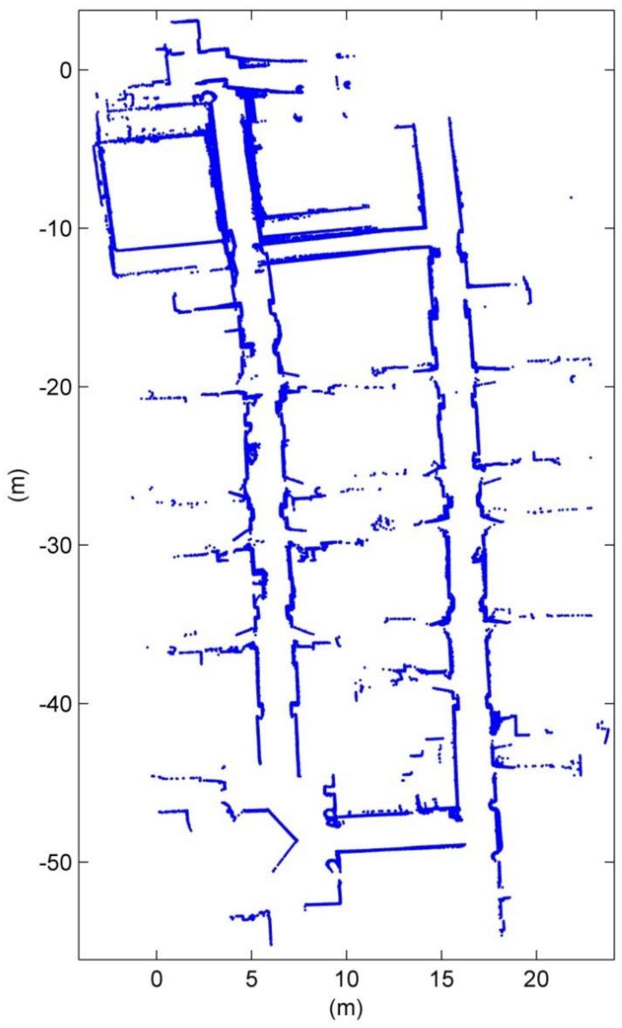

Figure 5.13: “C-Wing” experiment acquired using the proposed scan matching process, without the use of odometry data.

The third experiment comes from the Department of DIIGA at the Engineering University in Ancona [33]. This set contains 9,382 robot poses and uses a LRF of 80m of maximum range. Once again the odometry data is removed. To decrease the computational effort, only 1 robot pose out of every 5 was used in this evaluation, resulting in a number of robot poses of only 1,875. In Figure 5.14 the fitness function value is shown for each of the 1,874 robot displacements, calculated using the proposed method.

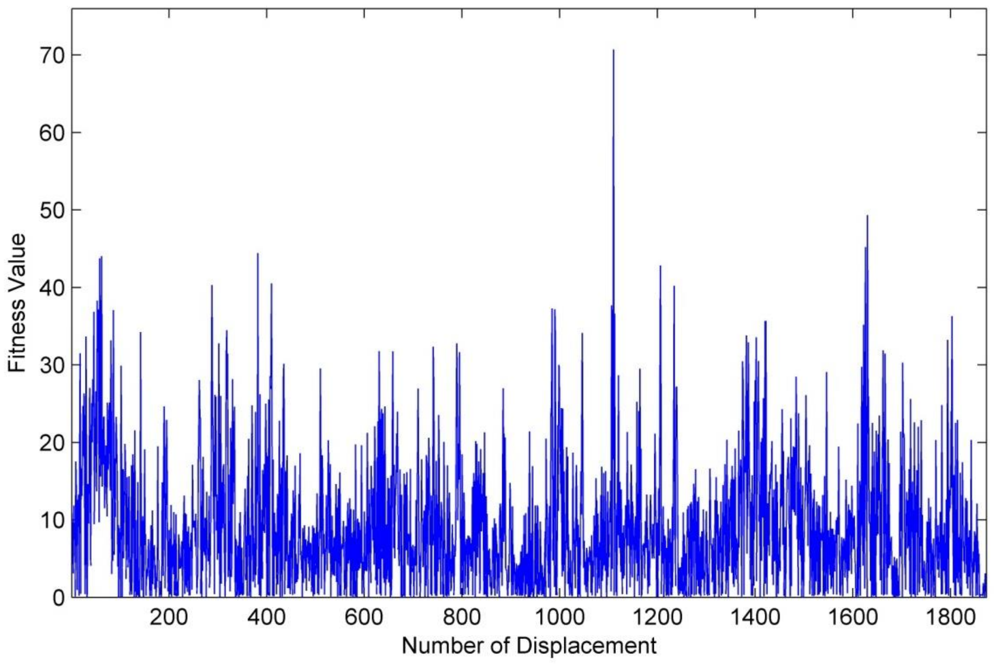

Figure 5.14: Fitness values for “Diiga” experiment.

This figure shows some peaks (50 in total) greater than 30. They have a probability of being a non-convergence in DE optimization.

The Figure 5.15 shows the “Diiga” experiment.

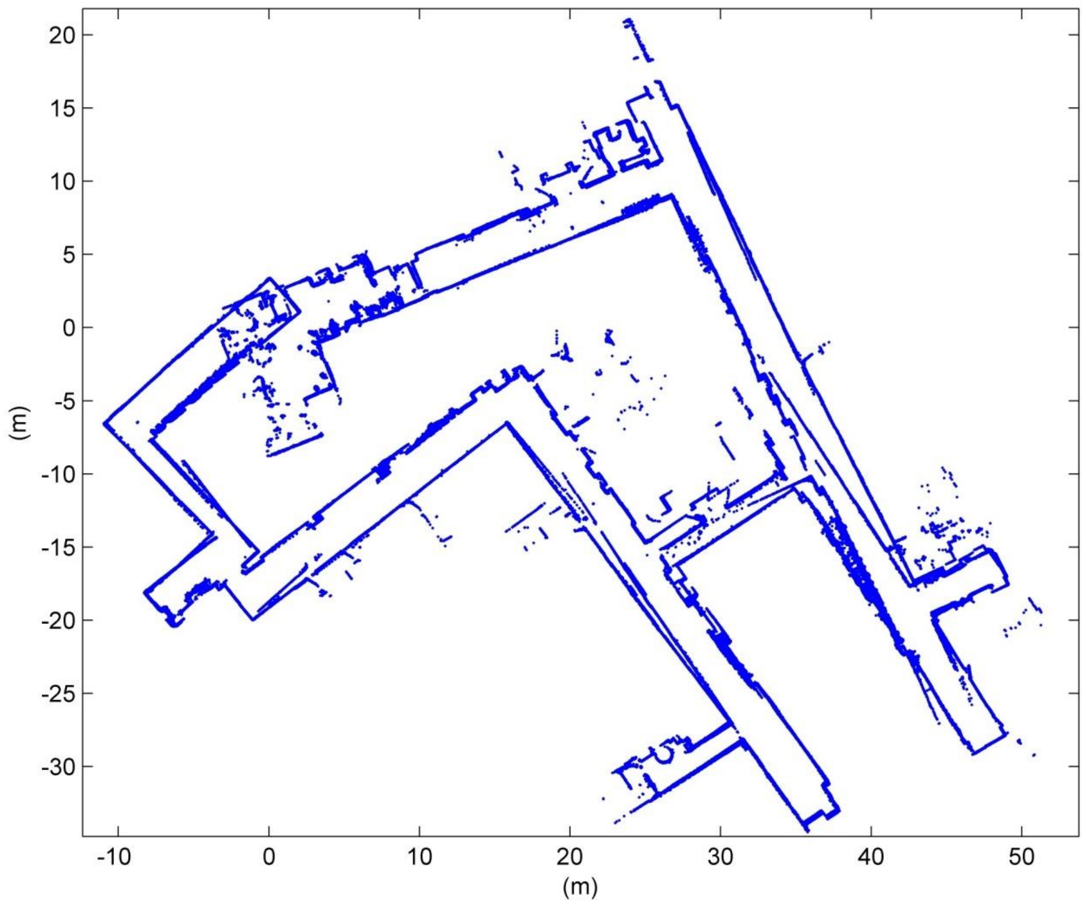

Figure 5.15: “Diiga” experiment acquired using the proposed scan matching process, without the use of odometry data.

The fourth experiment comes from the Kvarntorp mine, near to Örebro, Sweden [37]. It contains 95 robot poses with 3D scans; again the odometry data was removed.

Figure 5.16 shows the fitness function value for each of the 94 robot displacements, acquired using the proposed method. In this experiment, there are 36 fitness values greater than 30. This means that 37% of the matches are poor matches, consequently this produces a poor map as shown in Figure 5.17.

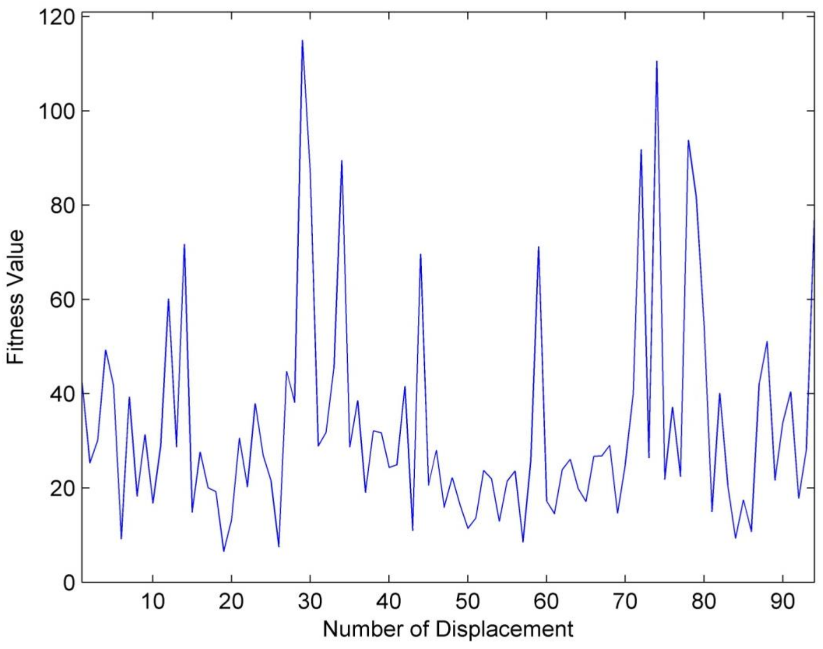

Figure 5.16: Fitness values for “Mine” experiment

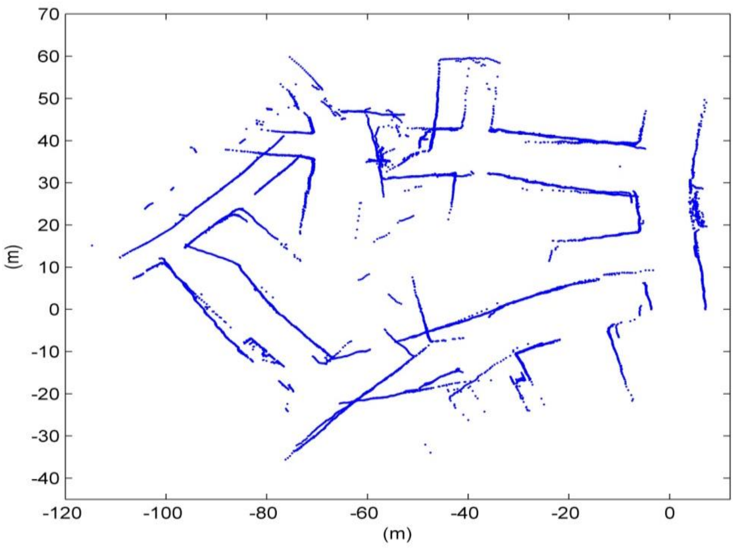

Figure 5.17: Poor map of “Mina” experiment.

This poor map is because scans were taken out of the search space parameters described in Section 4.4.2, **Error! Reference source not found.**. The simple solution that comes out is to increase these parameter ranges. But this is a risky solution, because this could lead to false positives and the map would end up worse.

In this case de adopted solution was to increase the NTD cell size to 4000mm (originally it was defined to 1000mm, as described in Section 2.3.3). This adopted solution has the effect of blurring the NDT representation and consequently facilitates the optimization convergence. However, this scaling increase only helps the translation optimization; rotations, on the other hand, can't be scaled. Thus to solve this problem, misaligned matches are ran individually on DE optimization, increasing or decreasing the rotation search space depending on the case.

Obviously, this is computationally intensive, but it is necessary to allow the proposed method to be successful even in the situations where the matching process is not guarantee.

The resulting map, after increasing the NTD cell size, but before running individually misaligned matches, was already shown in Figure 5.17. The map after running individually misaligned matches and varying the rotation search space is shown in Figure 5.18.

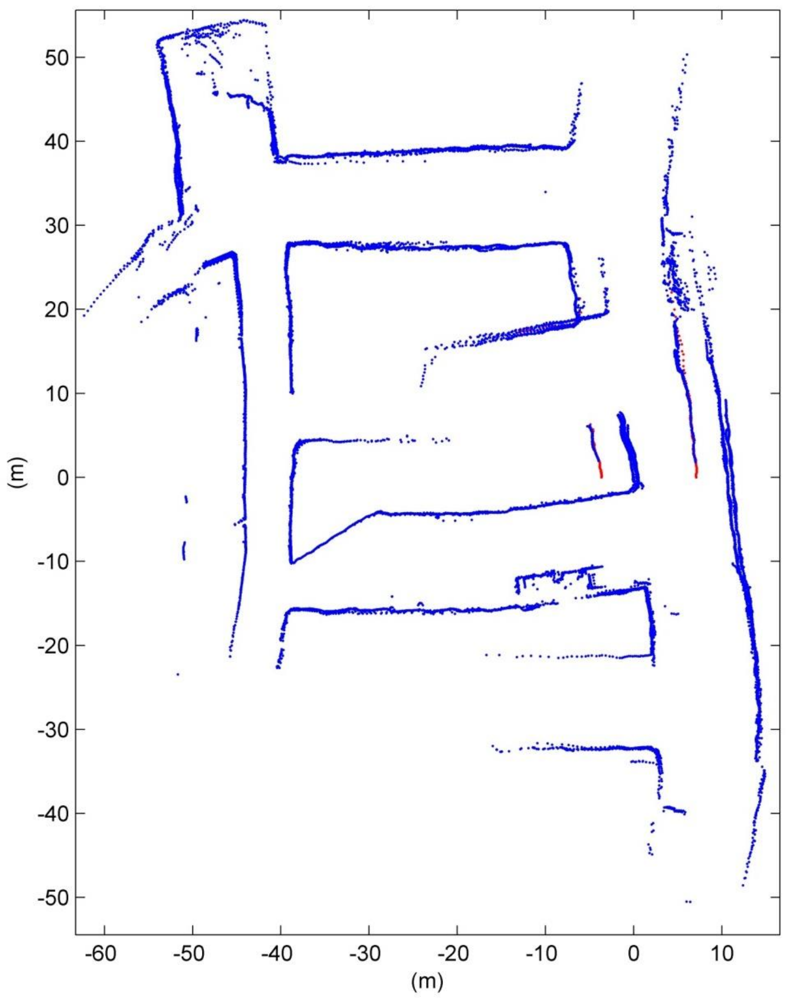

Figure 5.18: “Mina” experiment acquired using scan matching process

5.2. Motion Model

The analysis made using the fitness value on DE optimization helps to determine the quality of the obtained map. But there are some fitness values (in special in the “Diiga” experiment) greater than 30. In these cases, it is advised to manually examine these critical parts from the map. This, of course, suggests the need of a non automatic mapping, for such large fitness values. These results can be viewed as a first mapping step. The scan matching errors are managed in a second mapping step: the motion model in DP-SLAM.

In fact, computing the displacement error histogram (using the simulated experiment), they are distributed as Gaussians, as shown in Figure 5.19.

The distribution error in Δy (movement along robot's facing direction) as shown in Figure 5.19(c), can be approximated by a Gaussian with zero mean and standard deviation of 0.02m plus another Gaussian with mean on -0.20m and standard deviation of 0.10m. However, because always the robot movement is along its facing direction (unless it has significant slippage), the distribution error in Δx is different, and can be approximated by a simple Gaussian, as shown in Figure 5.19(a). In the same way, the distribution error in $\Delta\theta$ can be approximated by a Gaussian, as shown in Figure 5.19(b).

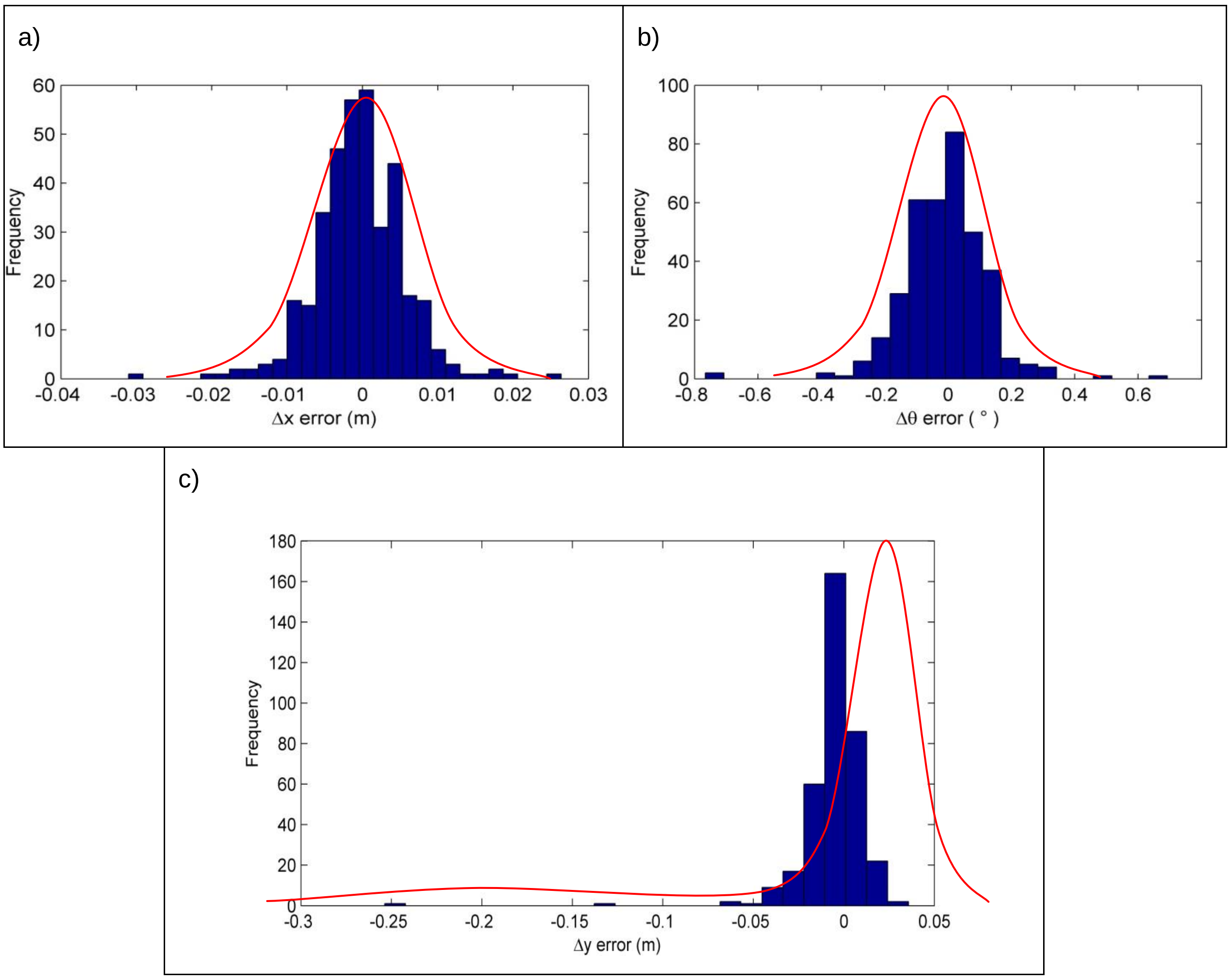

Figure 5.19: Error distribution in displacement: a) Δx, b) $\Delta\theta$ and c) Δy

These displacement errors in Δy are evident when looking in detail the maps acquired.

Figure 5.20 shows an example of this displacement error, taken from the experiment on a simulated environment from Section 5.1.

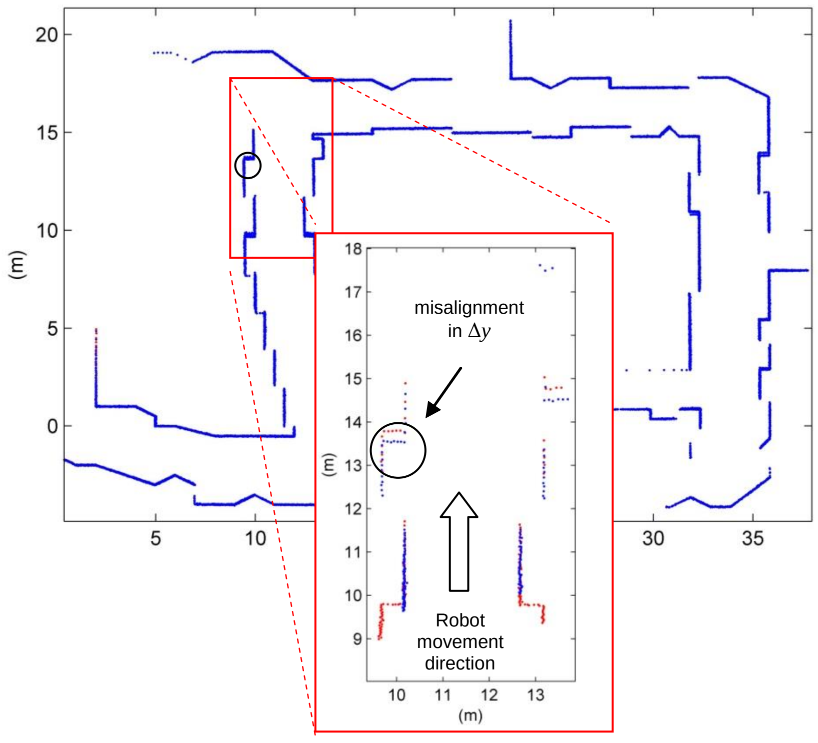

Figure 5.20: Misalignment in Δy (respect to the current robot position).

The averages and standard deviations of these three movements are the parameters used in the proposed motion model. It is expected that scan matching in real data follows the same distribution shapes, but it doesn't mean that the parameter values are the same.

The most complicated error parameter is related to the robot's face displacement, Δy. One important thing observed in real data, using the proposed scan matching, is that error displacements in this movement direction could depend on robot velocity. Figure 5.21 shows this idea: after a robot displacement in the time step Δt, the actual position is $R_t = [Rx_t \ Ry_t \ R\theta_t]$, but the scan matching gives a displacement $\boldsymbol{p} = [\Delta x \ \ \Delta y \ \ \Delta\theta]$ where Δy is near to cero or, in the best case, a value much lower than the actual displacement Δy_R. Thus the mean of the small

Gaussian in Figure 5.19(c), would be in $-\lambda$, where $\lambda = |\Delta t \cdot V_R|$ and V_R is the robot velocity.

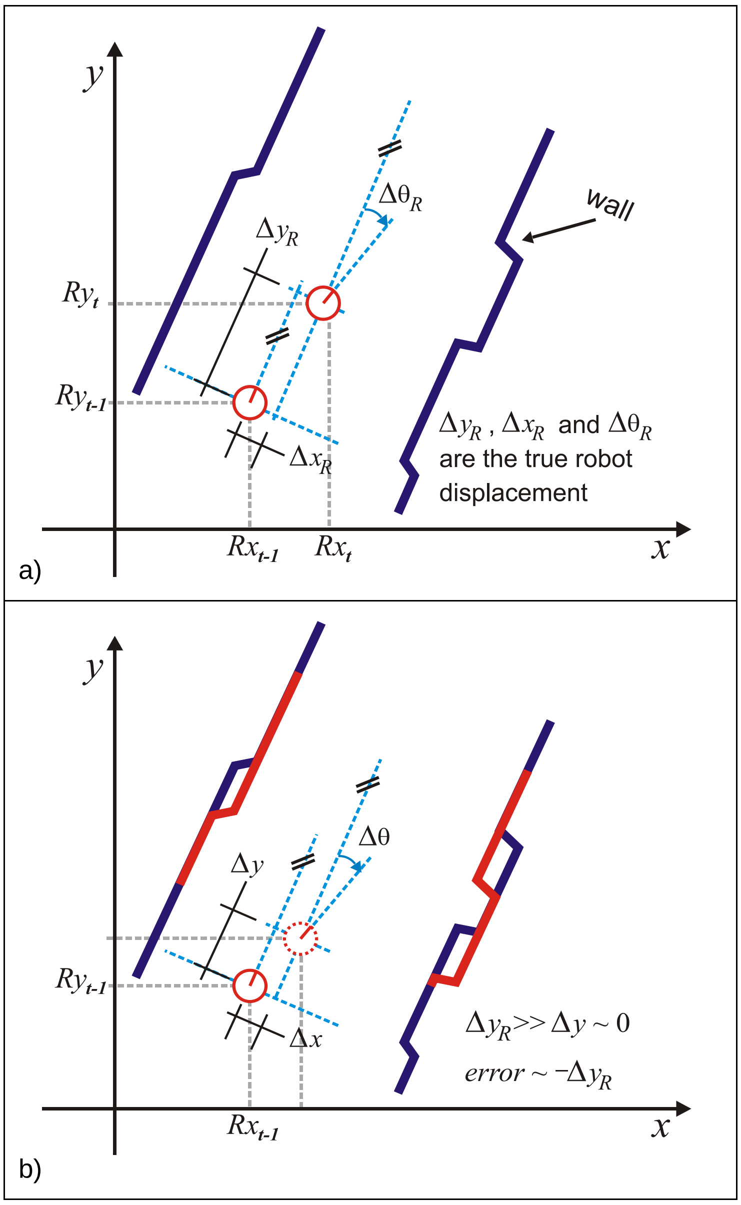

Figure 5.21: a) The true robot displacement. b) The displacement given by scan matching, showing that the most common error is in Δy.

Since one of the objectives in this work is no to use odometers, such robots with a single LRF cannot directly measure their velocity. However, it is possible to use the instants when the scans were taken and, in this way, compute the robot velocity(estimated using the displacement between scans on *t-2* and *t–1* and the time interval between them). Note, however, that this value need not be exact and could be approximated; this is an advantageous consequence of using a probabilistic approach.

Misalignments in Δy were also found in real data, as shown in Figure 5.22. Another important thing observed in real data is the fact that large displacement in Δy corresponds to small rotations $\Delta\theta$; this behavior is shown in Figure 5.23. This fact gives a restriction to the proposed motion model. Thus only when scan matching reports a small rotation, the motion model will be able to sample from the small Gaussian in Figure 5.19(c). The standard deviation assumed for this small Gaussian is $\sigma = (\lambda/2)$. On the other hand, the higher Gaussian in the same figure is assumed with zero mean and standard deviation: $\sigma = 0.02\text{m} + abs(\Delta y/10)$.

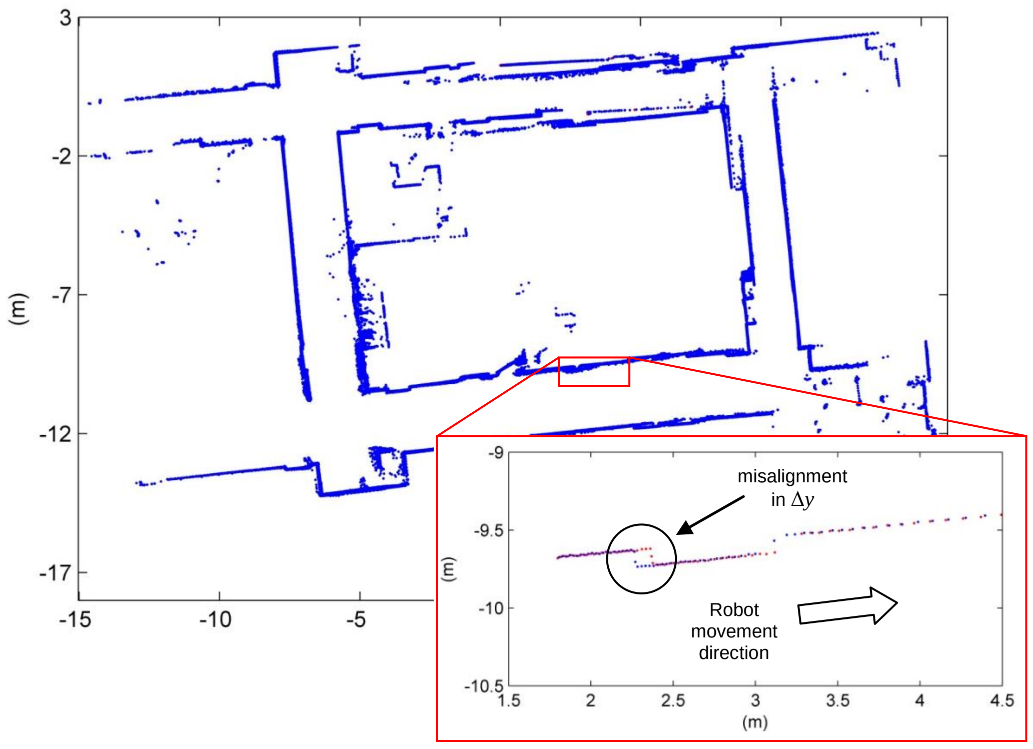

Figure 5.22: Misalignment in Δy (D-Wing experiment)

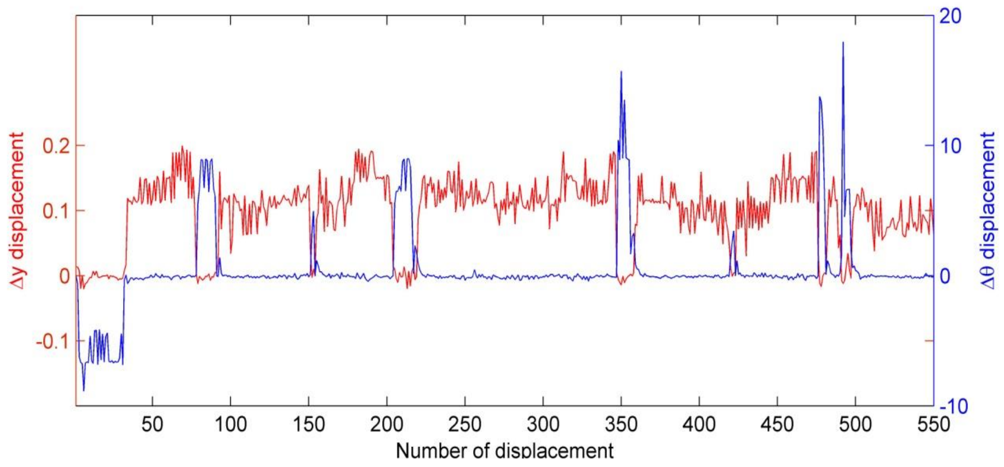

Figure 5.23: Larger displacement in Δy correspond to small rotations $\Delta\theta$ (D-Wing experiment).

The displacement error in Δx follows the distribution shape from Figure 5.19(a), which is simpler than the Δy error distribution, since it could simply be approximated by a zero mean Gaussian with standard deviation $\sigma = 0.02\text{m} + abs(\Delta x/10)$. In the same way the error in $\Delta\theta$ is approximated by a zero mean Gaussian with $\sigma = 0.5° + abs(\Delta\theta/10)$.

The final motion model is shown in Table 5.1, Table 5.2 and Table 5.3. Note that this algorithm is a more detailed version than the one from Table 4.7.

Table 5.1: Proposed Scan Matching Motion Model.

```
Sample SM Motion Model algorithm ($R_{t-1}$, $u_t$)
1:  $\Delta\hat{x} = \Delta x + sampleA(0.02\text{m} + abs(\Delta x/10))$
2:  $\Delta\hat{y} = \Delta y + sampleB(0.02\text{m} + abs(\Delta y/10), \lambda, \Delta\theta)$
3:  $\Delta\hat{\theta} = \Delta\theta + sampleA(0.5° + abs(\Delta\theta/10))$
4:  $d = \sqrt{(\Delta\hat{x})^2 + (\Delta\hat{y})^2}$
5:  $\alpha = R\theta_{t-1} - \pi/2 + \text{atan2}(\Delta\hat{y}, \Delta\hat{x})$
6:  $Rx_t = Rx_{t-1} + d\cos(\alpha)$
7:  $Ry_t = Ry_{t-1} + d\sin(\alpha)$
8:  $R\theta_t = R\theta_{t-1} + \Delta\hat{\theta}$
9:  return $R_t = (Rx_t, Ry_t, R\theta_t)$
```

Table 5.2: Approximate algorithm to sampling from normal distribution [1]

sampleA: sample_normal_distritubtion (v)	
1:	$return\ \frac{v}{6}\sum_{i=1}^{12} rand(-1,1)$

Table 5.3: Approximated Algorithm to sample from the Δy distribution error.

sampleB (v, λ , $\Delta\theta$)	
1:	$x = rand(0,1)$
2:	if ($x > 0.95$) && ($\Delta\theta < 3°$)
3:	*return* $sampleA(\lambda/2) + \lambda$
4:	else
5:	*return* $sampleA(v)$

5.3. DP-SLAM

From the incorporation of the motion model in the DP-SLAM algorithms, improved 2D maps are now obtained from the simulated environment and the experimental ones taken from the literature.

Figure 5.24 shows the simulated environment as 2D grid map. This map was acquired using 1000 particles in the LSLAM and 1500 particles in the HSLAM, with a resolution of 50mm.

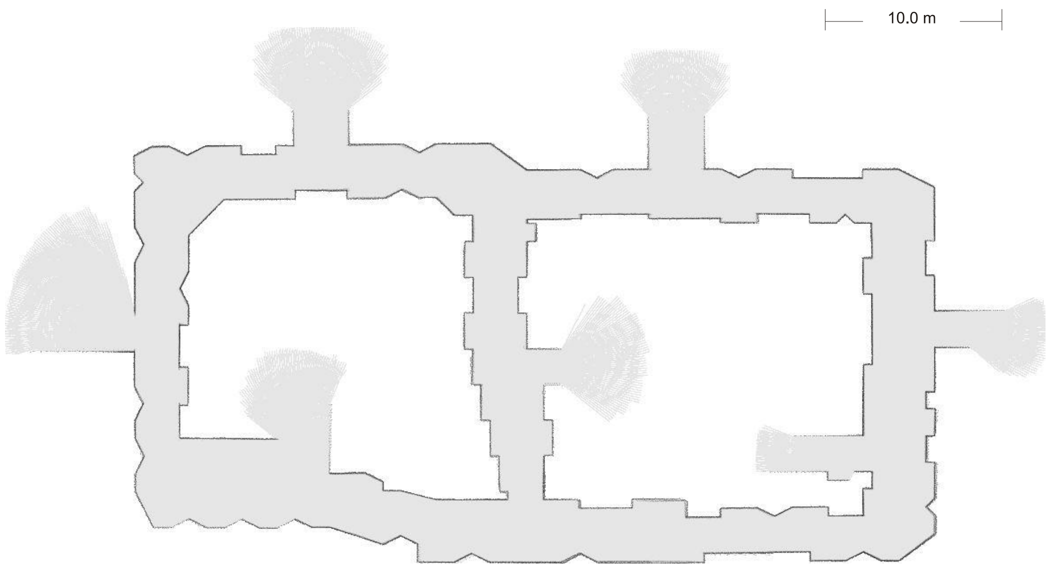

Figure 5.24: 2D grid map from the simulated environment experiment, obtained with DP-SLAM using the proposed motion model.

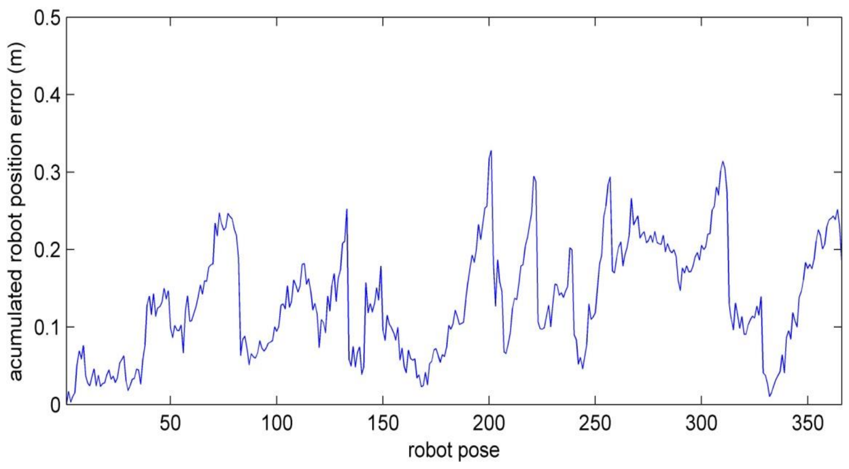

Figure 5.25: Accumulated error position obtained with DP-SLAM using the proposed motion model, on simulated experiment.

Figure 5.25 shows the accumulated error in robot position. Comparing this figure with Figure 5.7, it is clear that the error does not increase with time, being kept mostly under 300mm. Figure 5.26, Figure 5.27 and Figure 5.28 show the histograms of the errors in Δx, Δy, $\Delta\theta$.

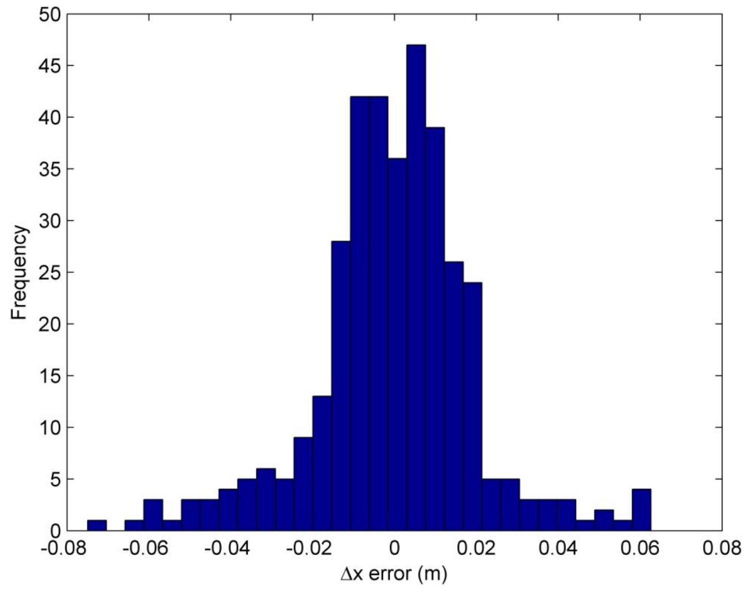

Figure 5.26: Error distribution in Δx obtained with DP-SLAM using the proposed motion model.

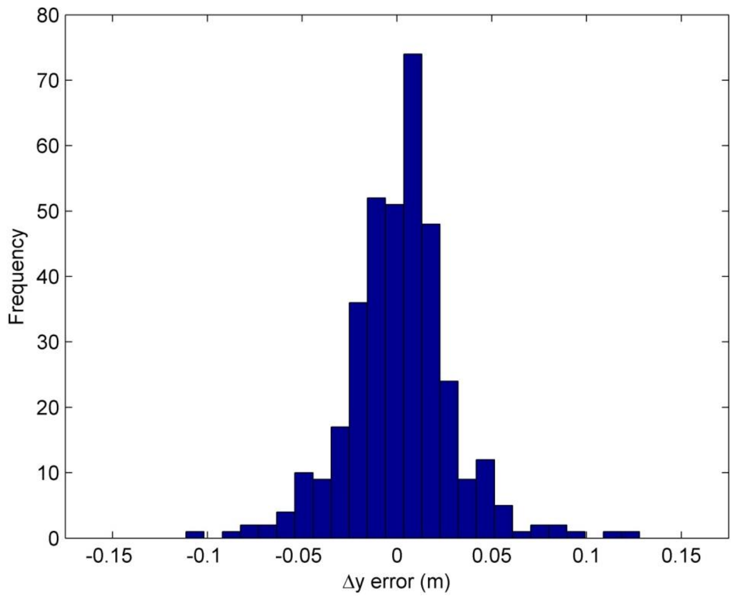

Figure 5.27: Error distribution in Δy obtained with DP-SLAM using the proposed motion model.

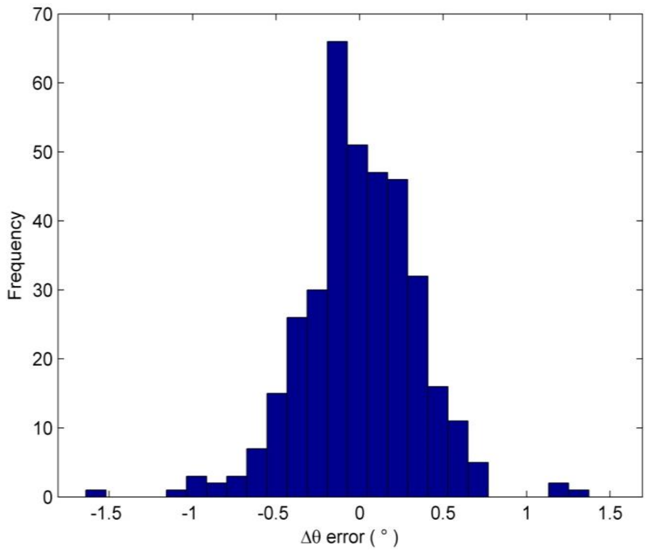

Figure 5.28: Error distribution in $\Delta\theta$ obtained with DP-SLAM using the proposed motion model.

Figure 5.29 shows another simulated environment that was also shown in

Figure **3.11**. The difference between them is that now the map is better because was built using hierarchical DP-SLAM. Thus, 1000 particles were used in the LSLAM and 1000 particles in the HSLAM, with a resolution of 50mm.

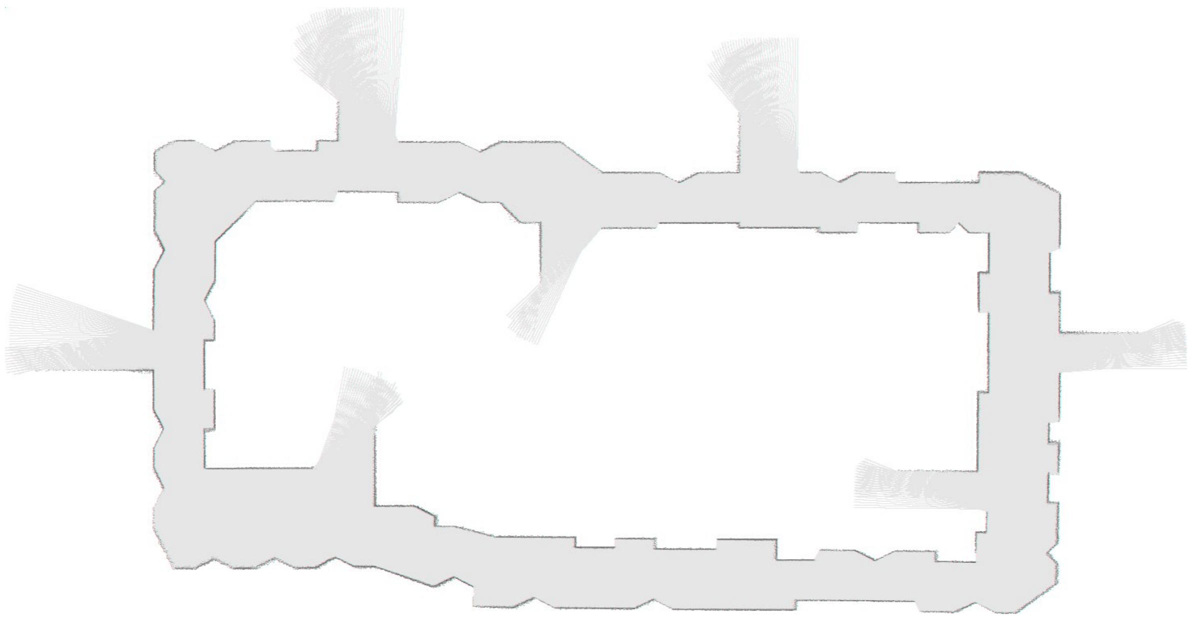

Figure 5.29: 2D grid map from simulated environment presented in

Figure 3.11.

Let’s now apply the proposed method to the experimental data from the literature. The first real experiment (D-Wing) in the form of 2D grid map is shown in Figure 5.30. This map was acquired using 500 particles in the LSLAM and 600 particles in the HSLAM, and it has a resolution of 50mm.

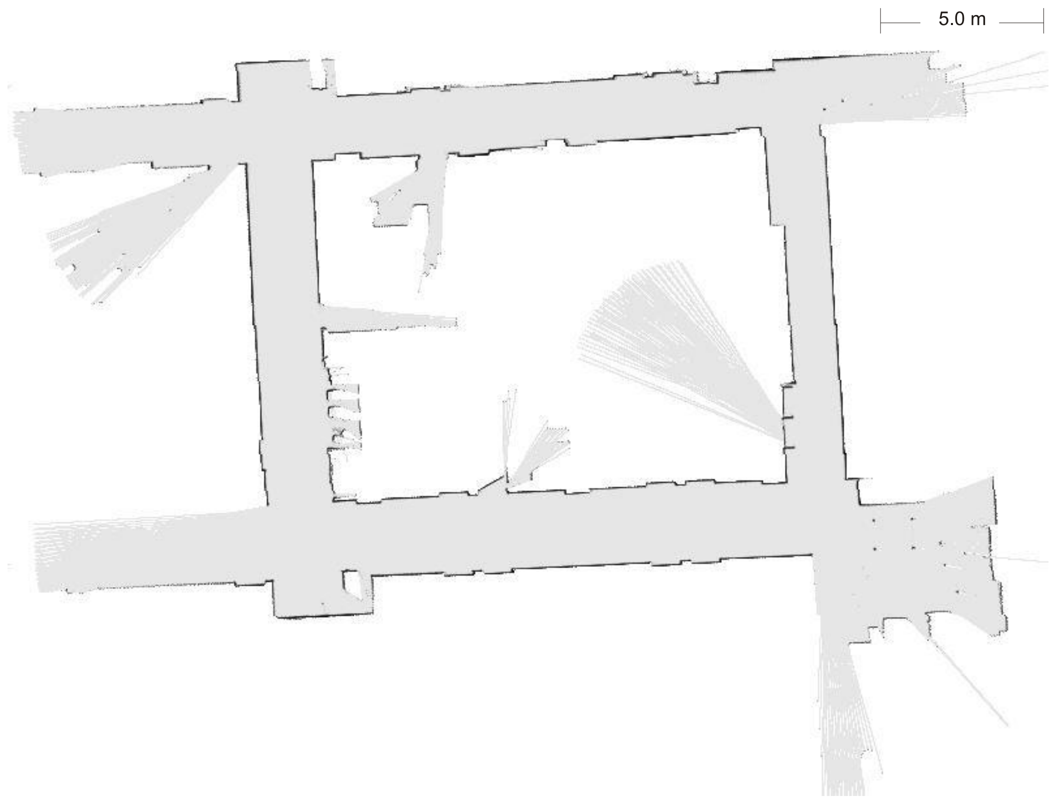

Figure 5.30: 2D grid map of “D-wing” experiment, acquired with DP-SLAM using the proposed motion model.

The second real experiment (C-Wing) in the form of 2D grid map is shown in Figure 5.31. This map was acquired using 600 particles in the LSLAM and 1,300 particles in the HSLAM, and a resolution of 40mm.

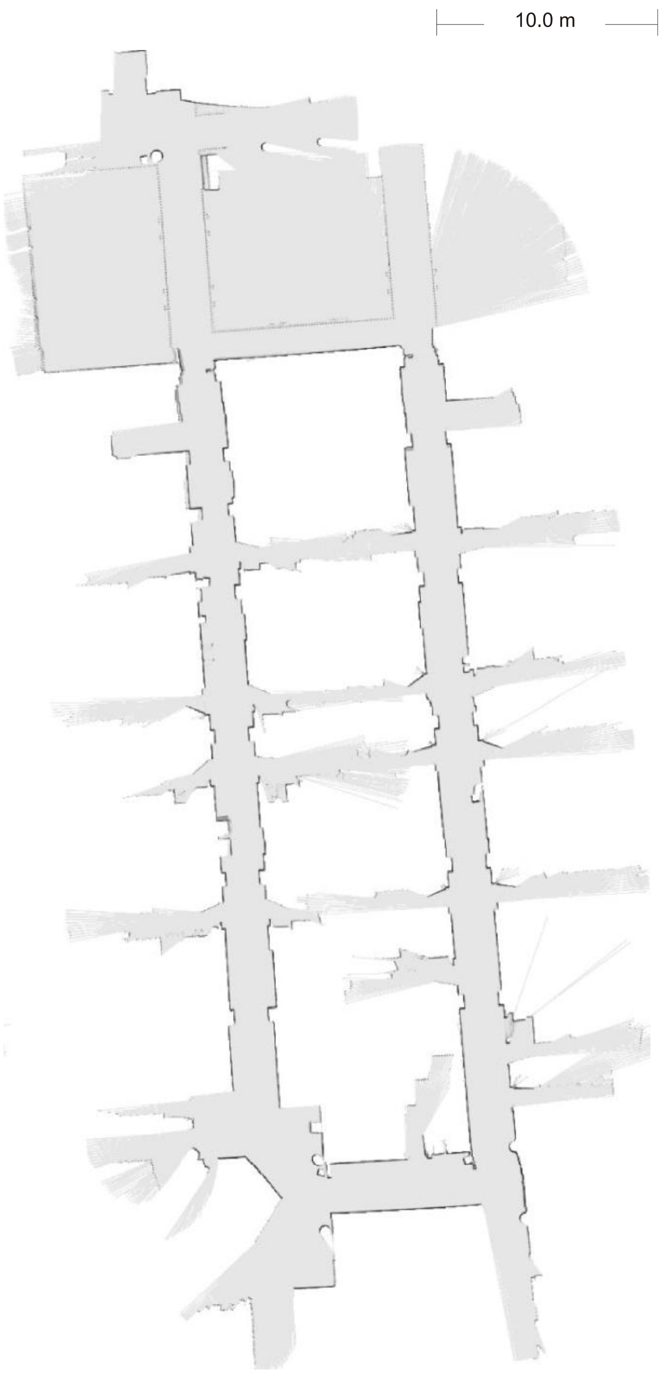

Figure 5.31: 2D grid map of “C-wing” experiment, acquired with DP-SLAM using the proposed motion model.

The third real experiment (“Diiga”) in the form of 2D grid map is shown in Figure 5.32. This map was acquired using 600 particles in the LSLAM and 1800 particles in the HSLAM, and it has a resolution of 40mm.

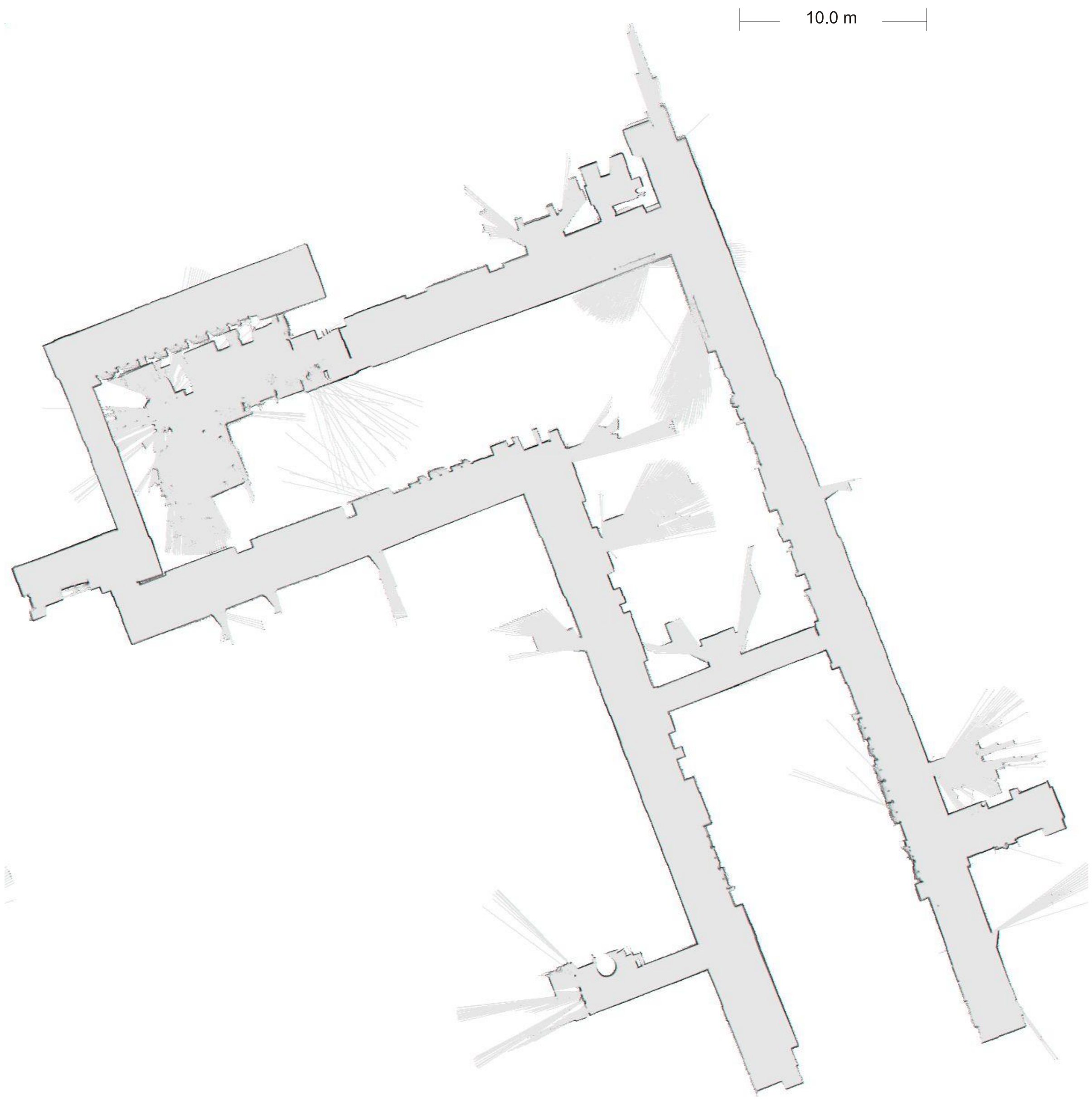

Figure 5.32: 2D grid map of "Diiga" experiment, acquired with DP-SLAM using the proposed motion model.

Finally, the fourth real experiment ("Mine") in the form of 2D grid map is shown in Figure 5.33. This map was acquired using only the LSLAM with 1,200 particles, with a 50 mm of resolution.

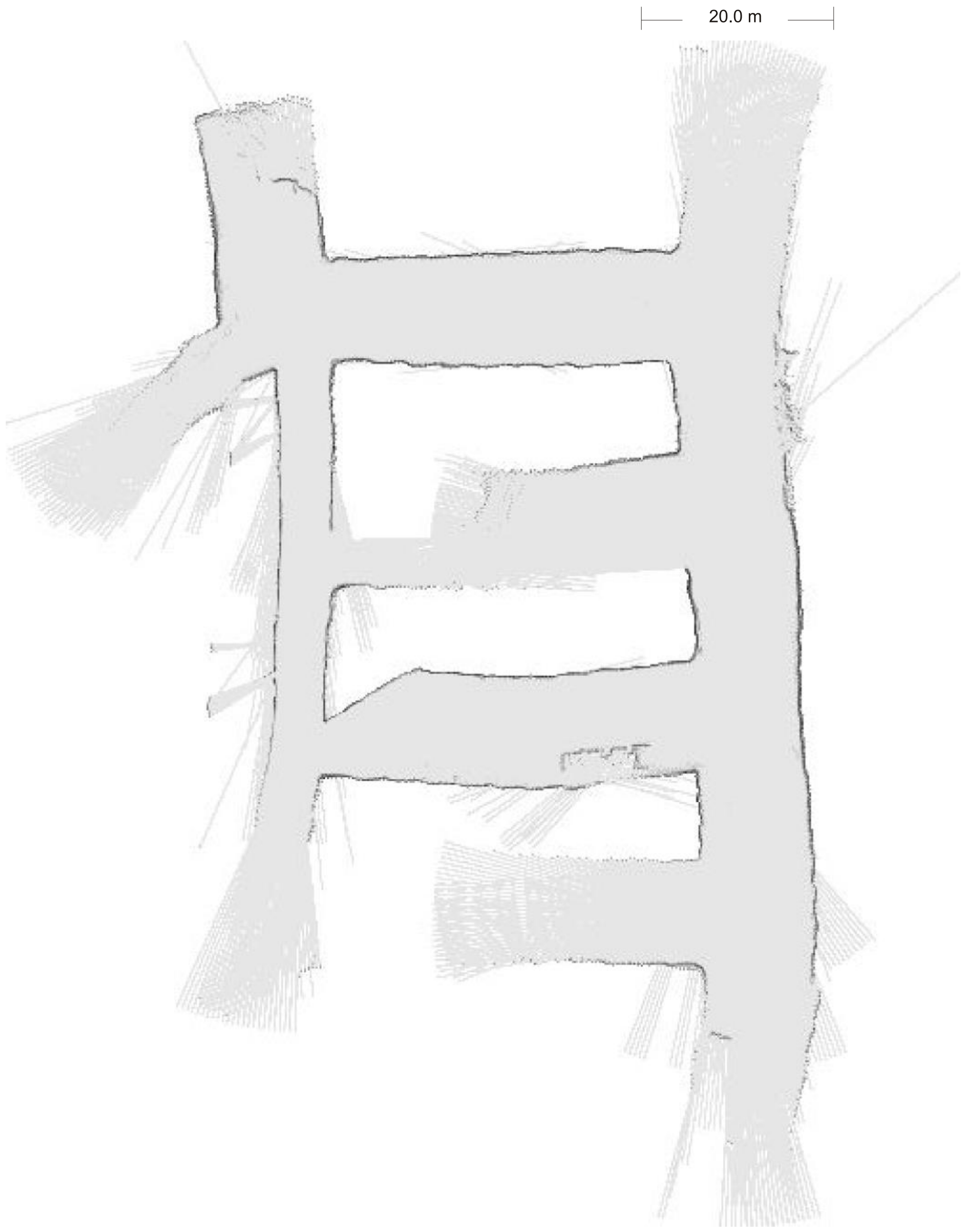

Figure 5.33: 2D grid map of “Mine” experiment, acquired with DP-SLAM using the proposed motion model.

5.4. 3D Mapping

The proposed mapping method using a single RLF uses Scan Matching and DP-SLAM to acquire 2D robot localization. Thus, as long as the parameter ranges shown in **Error! Reference source not found.** are satisfied, it will be possible to create as well 3D maps. However, almost all 3D data from available from literature, in special in [33] and [38], are out of these parameter ranges. Most of them are from unstructured environments, and those that are from indoor structured environments only picked up 3D data from sparse robot positions, not frequent enough to satisfactorily apply DP-SLAM without the use of odometer readings.

The previously simulated map is now used to evaluate the application of the proposed methods to 3D. The environment and LRF simulator presented in Section 4.3 is now applied to a 3D map.

As discussed in Section 3.3, trajectory given by the 2D DP-SLAM can be used to project the remaining three-dimensional data. Figure 5.34 shows a 3D map of the simulated environment exposed in previous section. It is represented in the form of a 3D point cloud map.

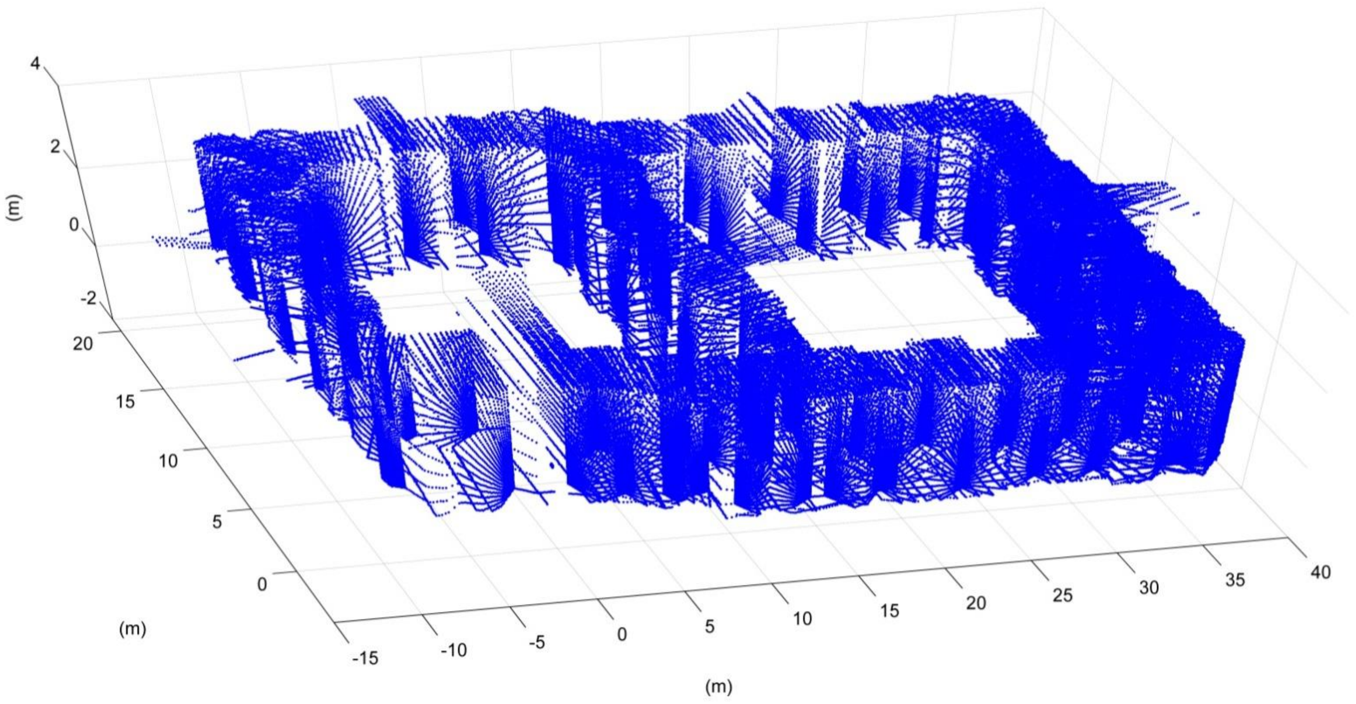

Figure 5.34: 3D point cloud map of the simulated environment.

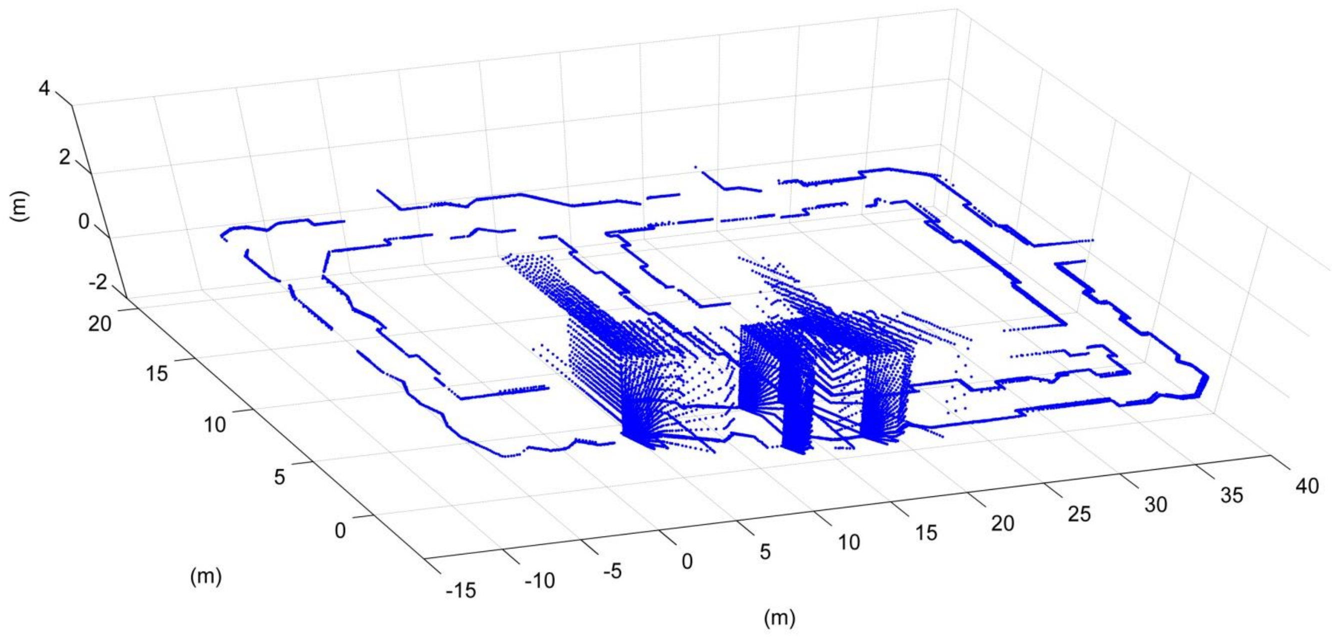

Figure 5.35: 3D point cloud of the simulated environment (only three 3D scans are shown)

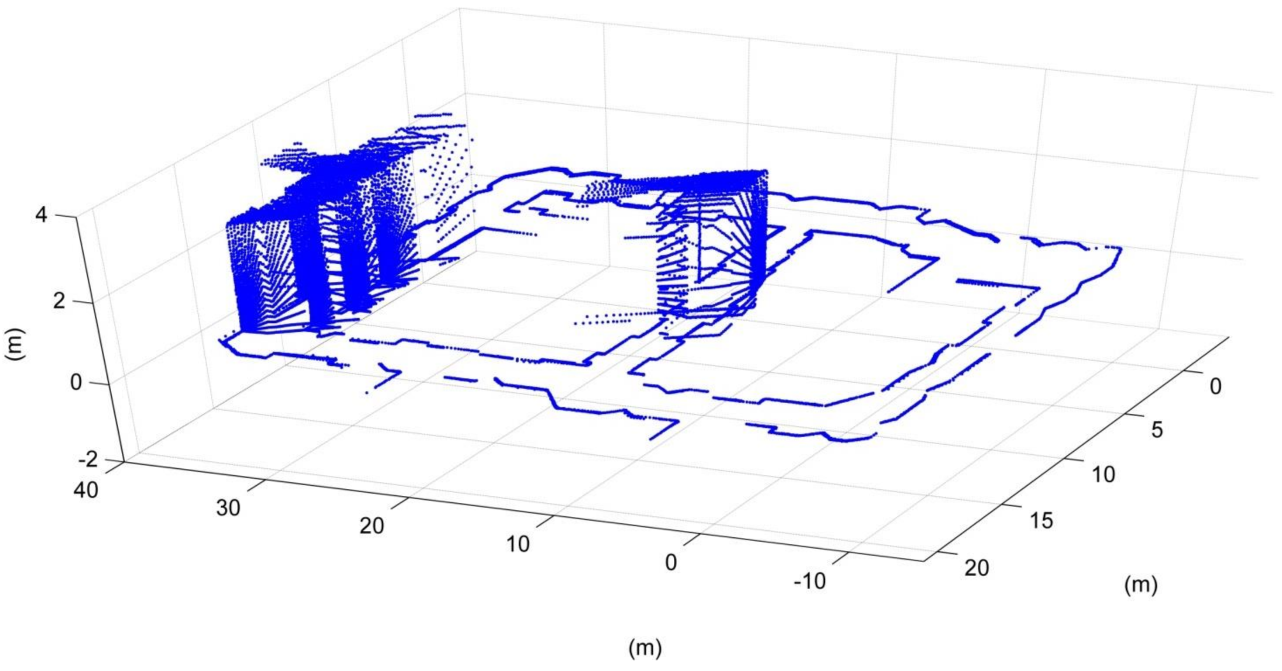

Figure 5.36: 3D point cloud of the simulated environment (only four 3D scans are shown).

The “Mine” experiment, shown in the previous section, is the only 3D real environment used in this work. However, it is an example of 3D data acquired from sparse robot positions; for this reason, its original dimensions were reduced by a factor of four and, after processing, returned to its original values.

Figure 5.37, Figure 5.38, Figure 5.39 and Figure 5.40 show the “Mine” experiment, but now in three dimensions, in the form of 3D point cloud map. This figures show only some 3D scans (not all) for visualization purposes.

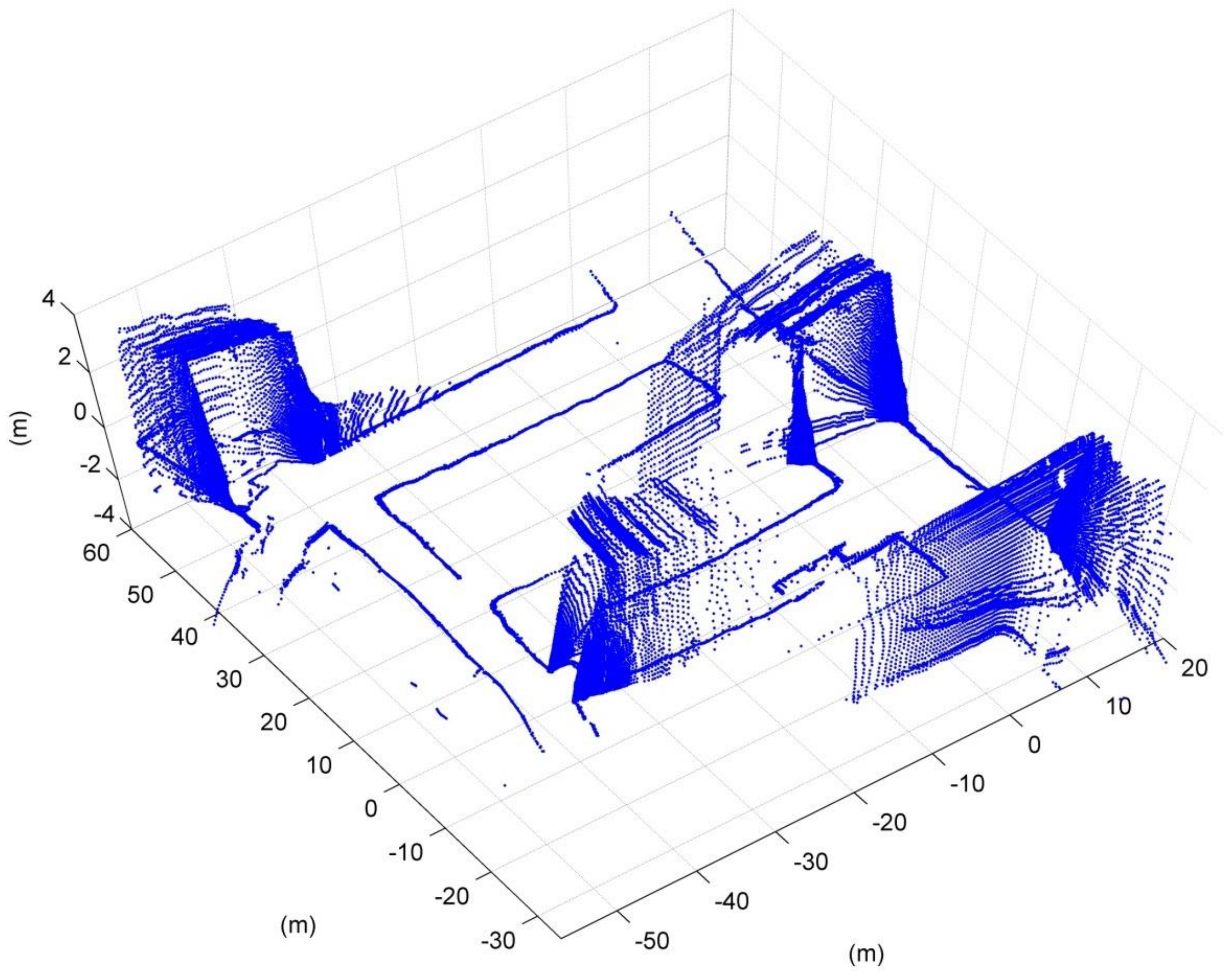

Figure 5.37: 3D point cloud of the “Mine” experiment.

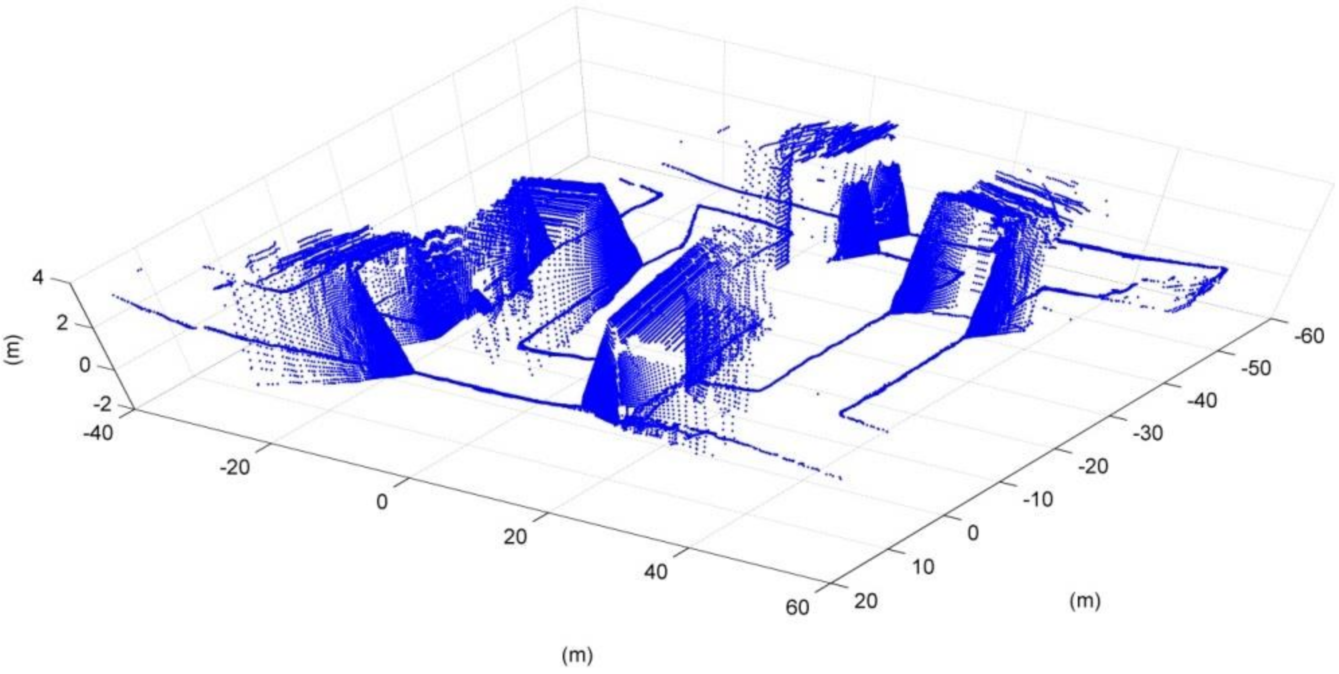

Figure 5.38: 3D point cloud of the “Mine” experiment.

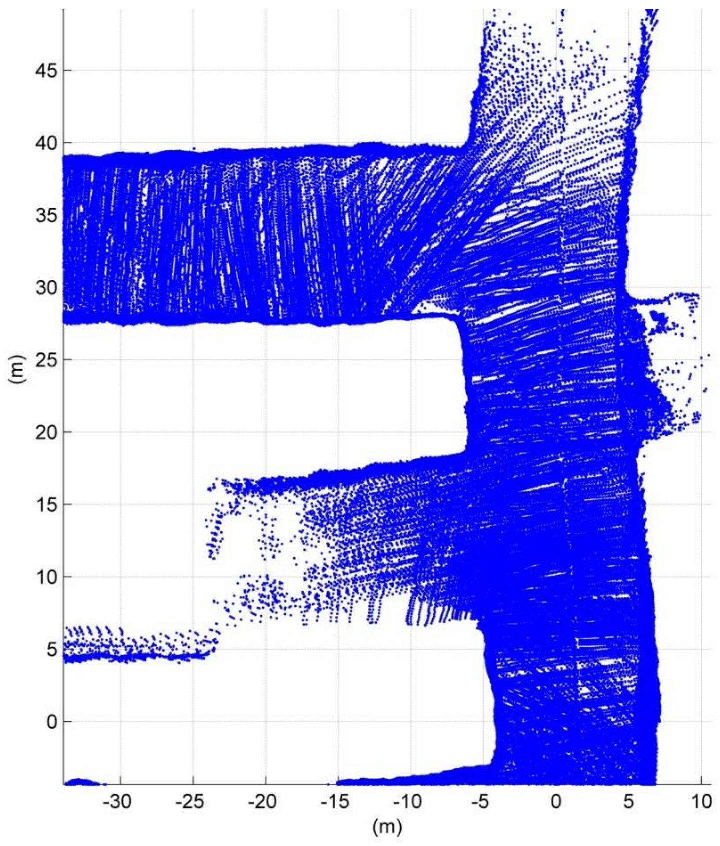

Figure 5.39: 3D point cloud of the “Mine” experiment (top view).

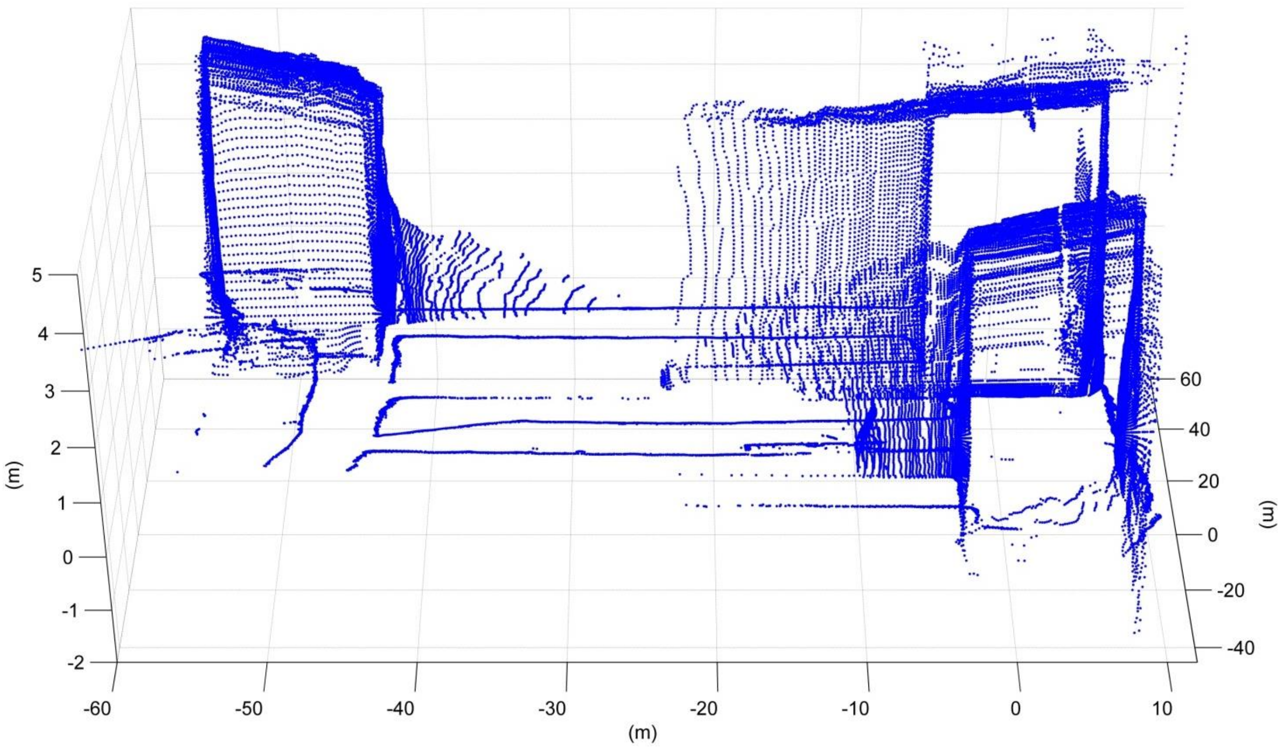

Figure 5.40: 3D point cloud of the “Mine” experiment.

6. Conclusions

This work explored the main SLAM solutions, given a detailed example for implementing the EKF-SLAM and FastSLAM; although the adopted solution, for the proposed application, was the DP-SLAM.

Thus, to perform SLAM without odometry information, the following algorithms were implemented:

- A simulator to acquire 3D data from structured environments; implemented on MatLab® platform.
- A scan matching algorithm, to get robot displacement without odometry information, based in genetic algorithm optimization for the Normal Distribution Transform; also implemented on MatLab® platform, using the Differential Evolution library acquired from reference [21].
- A modified DP-SLAM, which included a new motion model: the scan matching motion model; implemented on Visual C++ platform.

This method can deal as well with 3D environments, as long as the LRF is mounted on a rotating platform on the mobile robot, to allow both horizontal and vertical scans. As the robot moves, the LRF acquires 2D scans. Where and when 3D data is required, the robot stops and the platform rotates synchronized with the LRF to perform further 2D scans on different plane orientations. After traveling through a desired path, the acquired data is processed to obtain 2D or 3D maps.

In this way, the main contribution of this thesis is the application of DP-SLAM without the need for odometry information, just by using a single LRF. Furthermore, this comes with some considerations and advices, along with specific conclusions, detailed next.

6.1. DP-SLAM Conclusions

DP-SLAM is a powerful tool in 2D mapping so that, it doesn't need a separated loop detection algorithm.

Such a high performance comes with a high computational cost. Thus, DP-SLAM is an off-line mapping algorithm, due to the huge data it manages. The smallest experiment ("Mine") took about 1 hour to be evaluated and the longest ("Diiga") took about 5 hours, using a processor AMD Turion 64 with 2.1GHz. The time complexity of DP-SLAM is analyzed in detail in [6].

The Motion Model in DP-SLAM has a considerable influence in the mapping performance. Poor models will need a huge number of particles to obtain moderate results. Thus, the Scan Matching Motion Model proposed in this work could be improved to include holonomic robots, so that they can manage both Δx displacement errors as well as in Δy errors.

The "low map" size in LSLAM ("piece of data" in Figure 4.19) as proposed by [6] is a function of the number of iterations. Thus, [6] proposes between 75 to 150 iterations. But in the analysis in this thesis, these values didn't give good results. Basically, 150 iterations don't guarantee that the robot travels enough distance to be considered a low map. The robot could get hundreds of scans without leaving the same room. In all experiments made by DP-SLAM in this work, a low map is only created when robot travels about 3m in an approximately straight path. It was observed that, when a low map is created (the LSLAM algorithm finishes) within a fast robot rotation, the next low map (that uses a portion of the previous map) suffers major ambiguities and tends to produces poor particles.

In LSLAM, DP-SLAM uses the current map for particle weighing. The best particle is used to grow the map, adding the new observation. If the robot displacement is higher than the LRF's maximum range, then DP-SLAM does not have enough pieces of the map for particle weighing. Thus, it is recommended to have a LRF with maximum range large enough to avoid this undesired situation.

As a way of demonstrating the proposed method performance, the simulated map (Figure 5.8) is compared with the acquired map using DP-SLAM (Figure 5.24). Thus, in order to compare them, the contours (walls) of both maps are selected and then converted to bitmaps. In this case the pixel to pixel comparison gives 93.34% of similarity, this mean 6.66% of wrong pixels.

6.2. Scan Matching Conclusions

The time of convergence in DE optimization depends on population size and generation number. Population size of 100 with 50 generations takes approximately 18s using a processor AMD Turion 64 with 2.1GHz. This relatively long time, coupled with time consumed by DP-SLAM algorithm, make the proposed method an offline but robust solution.

Errors in Scan Matching, the first or any other, are outweighed by the motion model proposed in Section 5.2. Note also that the first scan or any other have the same level of reliability; thus, if the first scan, and consequently the first grid map, is not good, it can be improved by the subsequent iterations (subsequent scans), in the sense of a probabilistic fusion.

Misalignments found in scan matching (for Δy displacement) are due to the cell size defined in Section 2.3.3. I.e. small details in the environment are blurred in NDT representation, which leads to unclear limits in alignment. One solution would be to reduce the cell size, but this creates an NDT representation with sharp shape; this case, DE optimization would need a quite larger population to achieve convergence. However, with some considerations, the cell size could be dynamically defined, depending on the measured LRF values. Thus, if LRF returns small distances, for instance less than 3m, then the cell size would be reduced to 500 mm. For higher distances, 1m of cell size would be a good choice. This idea was not implemented in this thesis, but it suggests future works to determine the distance threshold for each cell size choice.

The LRF's maximum range, as in DP-SLAM, is a very important parameter in scan matching. Larger maxima mean more data (about the environment) in one scan, which helps to improve the alignment.

The scan matching proposed was implemented in Matlab®, while DP-SLAM was implemented in C++ (using the code from [32]). It is possible, of course, to use the same computer language for Scan Matching and DP-SLAM. To increase the algorithm speed, it is recommended to implement the scan matching in C++ as well. A powerful library for evolutionary computing, GCOM [38], can help in such task. This is a suggestion for future works.

There are solutions for 3D scan matching in non-planar terrain [39], [40] and [41]. Thus, they could be used as a basis to extend the proposed method to a 3D mapping in uneven terrain, using as well a single LRF without odometry information.

6.3. 3D Mapping Conclusions

The 3D maps presented in Section 5.4 use point cloud representation. Thus, the quality of these maps depends on LRF error, because they are simply plotted using the 2D trajectory given by DP-SLAM. However, DP-SLAM fuses probabilistic observations made for each cell, so, as the cell is more often observed as occupied, the darker it becomes. This idea could be applied in 3D representations as well. Thus, 3D observation may also be fused, similarly to what is done in 2D. Note that this does not mean using a 3D cell for localization or perception model: this means only using the 3D cells to print a 3D map output by fusing the available observations made at each 3D cell. This idea, however, was not implemented in this thesis but it is another suggestion for future works.

Another representation for 3D maps could be in the form of geometric planes. The Delaunay triangulation is a popular algorithm to create a simplified representation of the environment in the form of triangles acquired from a point cloud. There are commercial and open source software [42] specialized in processing this kind of data.

7. References

[1] THRUN, SEBASTIAN et al. *Probabilistic Robotics.* Cambridge, Massachusetts - London, England: The MIT Press, 2006.

[2] KLAFTER, RICHARD DAVID, THOMAS A. CHMIELEWSKI, and MICHAEL NEGIN. *Robotic Engineering: An Integrated Approach.* Prentice, Hall, 1989.

[3] FERREIRA, EDSON DE PAULA. *Robotica Básica.* Rio de Janeiro, 1991.

[4] HIEBER-TREUER, BRADLEY. "An Introduction to Robot SLAM (Simultaneous Localization And Mapping)." Edited by Bachelor of Arts in Computer Science - Middlebury College. Middlebury, Vermount, USA, 2007.

[5] THRUN, SEBASTIAN. "Robotic Mapping: A Survey." Pittsburgh, PA 15213: School of Computer Science - Carnegie Mellon University, February 2002.

[6] ELIAZAR, AUSTIN. "DP-SLAM." Department of Computer Science - Duke University, 2005.

[7] MORAVEC, H. P., and A. ELFES. "High resolution maps from wide angle sonar." St. Louis, Missouri: ICRA-85, 1985.

[8] BIBER, PETER. "The Normal Distributions Transform: A New Approach to Laser Scan." Sand 14, 72070 Tüingen, Germany: University of Tübingen, Germany, 2003.

[9] LU, FENG, and EVANGELOS MILIOS. "Robot Pose Estimation in Unknown Environments by Matching 2D Range Scans." North York, Canada M3J 1P3: Department of Computer Science, York University, 1994.

[10] ALSHAWA, M. "ICL: Iterative Closest Line a Novel Point Cloud Registration Algorithm Based on Linear Features." STRASBOURG, France: Photogrammetry and Geomatics Group MAP-PAGE UMR 694, 2007.

[11] AGHAMOHAMMADI, A. A., H. D. TAGHIRAD, A. H. TAMJIDI, and E. MIHANKHAH. "Feature-Based Laser Scan Matching For Accurate and High Speed Mobile Robot Localization." *Advanced Robotics and Automated Systems (ARAS).* Department of Electrical Engineering, K. N. Toosi University of Technology, 2007.

[12] LINGEMANN, KAI, HARTMUT SURMANN, ANDREAS NÜCHTER, and JOACHIM HERTZBERG. "Indoor and Outdoor Localization for Fast Mobile Robots." Sankt Augustin, Germany: Fraunhofer Institute for Autonomous Intelligent Systems (AIS), 2005.

[13] OLSON, EDWIN B. "Real-Time Correlative Scan Matching." Ann Arbor, MI, USA: Department of Electrical Engineering and Computer Science - University of Michigan, 2009.

[14] HOLLAND, John H. *Adaption in Natural and Artificial Systems.* Cambridge, Massachusetts: MIT Press, 1992.

[15] MAN, K. F., K. S. TANG, and S. KWONG. "Genetic Algorithms: Concepts and Applications." IEEE Transactions on Industrial Electronics, October 1996.

[16] DAVIS, LAWRENCE. "Handbook of Genetic Algorithms." New York: Davis, Lawrence, January 1991.

[17] FORREST, STEPHANIE. "Genetic Algorithms: Principles of Natural Selection Applied to Computation." Science Vol. 261, August 1993.

[18] NELSON, ANDREW L., GREGORY J BARLOW, and LEFTERIS DOITSIDIS. "Fitness functions in evolutionary robotics: A survey and analysis." ELSEVIER - Robotics and Autonomous Systems, September 2008.

[19] BABUA, B.V., and S.A. MUNAWARB. "Differential evolution strategies for optimal design of shell-and-tube heat exchangers." ELSEVIER - Chemical Engineering Science, April 2007.

[20] STORN, RAINER, and KENNETH PRICE. "Differential Evolution - A simple and efficient adaptive scheme for global optimization over continuous spaces." Berkeley, CA, USA: International Computer Science Institute, March 1995.

[21] STORN, RAINER, and KENNETH PRICE. *Differential Evolution (DE).* Availabel on: <http://www.ICSI.Berkeley.edu/~storn/code.html>. Accessed in: June 2010.

[22] WELCH, GREG, and GARY BISHOP. "An Introduction to the Kalman Filter." Chapel Hill, NC, USA: University of North Carolina at Chapel Hill, July 2006.

[23] MONTEMERLO, MICHAEL, SEBASTIAN THRUN, DAPHNE KOLLER, and BEN WEGBREIT. "FastSLAM: A Factored Solution to the Simultaneous Localization and Mapping Problem." Pittsburgh, Stanford, USA: Carnegie Mellon University - Stanford University, 2002.

[24] TAKEZAWA, S., D. C. HERATH, and G. DISSANAYAKE. "SLAM in Indoor Environments with Stereo Vision." Sendai, Japan: IEEE/RSJ International Conference on Intelligent Robots and Systems, 2004.

[25] DAVISON, ANDREW J., YOLANDA GONZÁLEZ CID, and NOBUYUKI KITA. "Real-Time 3D SLAM with Wide-Angle Vision." Lisboa, Portugal: 5th IFAC/EURON Symposium on Intelligent Autonomous Vehicles, 2004.

[26] THRUN, SEBASTIAN; THAYER, SCOTT; WHITTAKER, WILLIAM; BAKER, CHRISTOPHER; BURGARD, WOLFRAM; FERGUSON, DAVID; HÄHNEL, DIRK; MONTEMERLO, MICHAEL; MORRIS, AARON; WHITTAKER, WARREN;. "Autonomous Exploration and Mapping of Abandoned Mines." IEEE Robotics & Automation Magazine, 2004.

[27] WEINGARTEND, JAN, and ROLAND SIEGWART. "EKF-based 3D SLAM for Structured Environment Reconstruction." Edmonton Alberta, Canada: IEEE/RSJ International Conference on Intelligent Robots and Systems (IROS), August 2005.

[28] ZUREIKI, AYMAN, and MICHEL DEVY. "SLAM and Data Fusion from Visual Landmarks and 3D Planes." Seul, Korea: 17th Congress The International Federation of Automatic Control, July 2008.

[29] COLON, ERIC, HICHEM SAHLI, and YVAN BAUDOIN. "MoRoS3D, a multi mobile robot 3D simulator." Brussels, Belgium: Proceedings of the 9th International Conference on Climbing and Walking Robots, September 2006.

[30] BEDKOWSKI, J., M. KRETKIEWICZ, and A. MASLOWSKI. "3D laser range finder simulation based on rotated LMS SICK 200." Warsaw, Poland: Research Institute of Automation and control Intelligent Mobile System Division, 2008.

[31] LOHANI, BHARAT, and R. K. MISHRA. "Generating LIDAR Data in Laboratory: LIDAR Simulator." Espoo, Finland: ISPRS Workshop on Laser Scanning 2007 and SilvilLaser 2007, September 2007.

[32] ELIAZAR, AUSTIN, and RONALD PARR. *DP-SLAM.* Available on: <http://www.cs.duke.edu/~parr/dpslam/>. Accessed in: June 2010.

[33] Creative Commons. *Radish: The Robotics Data Set Repository - Standard Data Sets for the Robotics Community.* Available on: <http://radish.sourceforge.net>. Accessed in: May 2010.

[34] SICK-Sensor Intelligence. *Laser Measurement Systems.* Availabe on: <https://www.mysick.com/saqqara/pdf.aspx?id=im0012759>. Accessed in: July 2010.

[35] BURGUERA, ANTONI; GONZÁLEZ, YOLANDA; GABRIEL, OLIVER. "On the Use of Likelihood Fields to Perform Sonar Scan Matching Localization." Springer Science - Business Media, January 2009.

[36] GUTMANN, JENS-STEFFEN; SCHLEGEL, CHRISTIAN. "AMOS: Comparison of Scan Matching Approaches for Self-Localization in Indoor Environments." Ulm, Germany: Research Institute for Applied Knowledge Processing (FAW), August 2002.

[37] NÜCHTER, ANDREAS, and KAI LINGEMANN. *Robotic 3D Scan Repository.* Available on:< http://kos.informatik.uni-osnabrueck.de/3Dscans/>. Jacobs University Bremen - University of Osnabrück. Accessed in: November 2010.

[38] PUC-Rio. *Inteligencia Computacional Aplicada.* Available on: <http://www.ica.ele.puc-rio.br>. Rio de Janeiro, Accessed in: June 2010.

[39] MAGNUSSON, MARTIN, HENRIK ANDREASSON, ANDREAS NÜCHTER, and ACHIM J. LILIENTHAL. "Automatic Appaerance-Based Loop Detection from Three-Dimensional Laser Data Using the Normal Distribution Transform." Journal of Field Robotics - JFR, vol 26, August 2009.

[40] BORRMANN, DORIT, JAN ELSEBERG, KAI LINGEMANN, ANDREAS NÜCHTER, and JOACHIM HERTZBERG. "Globally Consistent 3D Mapping with Scan Matching." Osnabrück, Germany: ELSEVIER - Robotics and Autonomous Systems, July 2007.

[41] HÄHNEL, DIRK, and WOLFRAM BURGARD. "Probabilistic Matching for 3D Scan Registration." Freiburg, Germany: Department of Computer Science, University of Freiburg, 2002.

[42] SOURCE FORGE. *Mesh Lab.* Available on: <http://meshlab.sourceforge.net/>. Accessed in: January 2011.

[43] MURPHY, KEVIN P. "Bayesian Map Learning in Dynamic Environments." Berkely, CA, USA: Computer Science Division - University of California, 2000.